UNIVERSIDADE FEDERAL DE MINAS GERAIS
Instituto de Ciências Exatas
Programa de Pós-graduação em Física

Bárbara Elza Nogueira de Faria

HYPERSPECTRAL IMAGING AND TIME-RESOLVED SPECTROSCOPY OF PHOTOEXCITED PROCESSES IN BIOMOLECULES

Belo Horizonte
2020

Bárbara Elza Nogueira de Faria

HYPERSPECTRAL IMAGING AND TIME-RESOLVED SPECTROSCOPY OF PHOTOEXCITED PROCESSES IN BIOMOLECULES

Thesis Presented to the Postgraduation Program in Physics from the Instituto de Ciências Exatas of the Universidade Federal de Minas Gerais as a Partial Requirement for Obtaining the Title of Doctor of Science.

Supervisor: Ana Maria de Paula
Co-supervisor: Cristian Manzoni

Belo Horizonte
2020

Dados Internacionais de Catalogação na Publicação (CIP)

F224h Faria, Bárbara Elza Nogueira de.
Hyperspectral imaging and time-resolved spectroscopy of photoexcited processes in biomolecules / Bárbara Elza Nogueira de Faria. – 2020.
100 f. : il.

Orientadora: Ana Maria de Paula.
Coorientador: Cristian Manzoni.
Tese (doutorado) – Universidade Federal de Minas Gerais, Departamento de Física.
Bibliografia: f. 83-91.

1. Ótica. 2. Espectroscopia por transformada de Fourier. 3. Biomoléculas. I. Título. II. Paula, Ana Maria de. III. Manzoni, Cristian. IV. Universidade Federal de Minas Gerais, Departamento de Física.

CDU – 535 (043)

Ficha catalográfica elaborada por Romário Martins Ribeiro – CRB6 3595
Biblioteca Professor Manoel Lopes de Siqueira – Departamento de Física - UFMG

UNIVERSIDADE FEDERAL DE MINAS GERAIS
Instituto de Ciências Exatas
Programa de Pós-Graduação em Física

ATA DA SESSÃO DE ARGUIÇÃO DA 369ª TESE DO PROGRAMA DE PÓS-GRADUAÇÃO EM FÍSICA, DEFENDIDA POR BÁRBARA ELZA NOGUEIRA DE FARIA orientada pela professora Ana Maria de Paula e coorientada pelo professor Cristian Manzoni, para obtenção do grau de **DOUTORA EM CIÊNCIAS, área de concentração física**. Às 14:00 horas de vinte e nove de junho de dois mil e vinte reuniu-se, por videoconferência, a Comissão Examinadora, composta pelos professores **Ana Maria de Paula** (Orientadora - Departamento de Física/UFMG), **Luiz Alberto Cury** (Departamento de Física/UFMG), **Ubirajara Agero Batista** (Departamento de Física/UFMG), **Ricardo Rego Bordalo Correia** (Instituto de Física/UFRGS) e **Lino Misoguti** (Instituto de Física/USP - São Carlos) para dar cumprimento ao Artigo 37 do Regimento Geral da UFMG, submetendo a Mestre **BÁRBARA ELZA NOGUEIRA DE FARIA** à arguição de seu trabalho de Tese de Doutorado, que recebeu o título de **"Hyperspectral imaging and time-resolved spectroscopy of photoexcited processes in biomolecules".** A candidata fez uma exposição oral de seu trabalho durante aproximadamente 50 minutos. Após esta, os membros da comissão prosseguiram com a sua arguição, e apresentaram seus pareceres individuais sobre o trabalho, concluindo pela aprovação da candidata.

Belo Horizonte, 29 de Junho de 2020.

Profa. Ana Maria de Paula
Orientadora da estudante
Departamento de Física/UFMG

Prof. Luiz Aberto Cury
Departamento de Física/UFMG

Ubirajara Agero Batista
Departamento de Física/UFMG

Prof. Ricardo Rego Bordalo Correia
Instituto de Física/UFRGS

Prof. Lino Misoguti
Instituto de Física/USP-São Carlos

Candidata

Documento assinado eletronicamente por **Ubirajara Agero Batista**, **Membro de comissão**, em 29/06/2020, às 17:48, conforme horário oficial de Brasília, com fundamento no art. 6°, § 1°, do Decreto n° 8.539, de 8 de outubro de 2015.

Documento assinado eletronicamente por **Luiz Alberto Cury**, **Professor do Magistério Superior**, em 29/06/2020, às 18:20, conforme horário oficial de Brasília, com fundamento no art. 6°, § 1°, do Decreto n° 8.539, de 8 de outubro de 2015.

Documento assinado eletronicamente por **Ana Maria de Paula**, **Professora do Magistério Superior**, em 29/06/2020, às 18:26, conforme horário oficial de Brasília, com fundamento no art. 6°, § 1°, do Decreto n° 8.539, de 8 de outubro de 2015.

Documento assinado eletronicamente por **Lino Misoguti**, **Usuário Externo**, em 08/07/2020, às 10:28, conforme horário oficial de Brasília, com fundamento no art. 6°, § 1°, do Decreto n° 8.539, de 8 de outubro de 2015.

Documento assinado eletronicamente por **Ricardo Rego Bordalo Correia**, **Usuário Externo**, em 08/07/2020, às 11:08, conforme horário oficial de Brasília, com fundamento no art. 6°, § 1°, do Decreto n° 8.539, de 8 de outubro de 2015.

Documento assinado eletronicamente por **BÁRBARA ELZA NOGUEIRA DE FARIA**, **Usuário Externo**, em 08/07/2020, às 12:06, conforme horário oficial de Brasília, com fundamento no art. 6°, § 1°, do Decreto n° 8.539, de 8 de outubro de 2015.

A autenticidade deste documento pode ser conferida no site https://sei.ufmg.br/sei/controlador_externo.php?acao=documento_conferir&id_orgao_acesso_externo=0, informando o código verificador **0163008** e o código CRC **42B1C841**.

Referência: Processo n° 23072.216690/2020-21 SEI n° 0163008

Acknowledgements

Agradeço primeiro a Deus, por ser tão bom comigo e me abençoar sempre. Sem Ele eu nada seria e nada desse trabalho teria sido possível. Obrigada por estar sempre comigo.

Agradeço a Ana Maria, por ter aceitado me orientar, mesmo sabendo que eu nunca tinha entrado em um laboratório de óptica. Obrigada pela paciência e por me ajudar em todas as minhas limitações. Agradeço também pela amizade, pelas conversas, pelas cervejas, enfim, por ser mais que uma orientadora.

Agradeço os meus pais, Geraldo e Sirlene, por sempre acreditarem em mim e no meu trabalho. Obrigada por me apoiarem, nunca permitirem que eu desistisse do meu sonho de ser pesquisadora. Vocês são meu exemplo de pessoas boas e corretas, espero algum dia chegar lá.

Agradeço o Samuel, que é tudo para mim. Obrigada por gostar do meu trabalho, por me apoiar, me ajudar com o inglês que até hoje me atrapalho, por ler meus textos infinitas vezes, pelo companherismo, enfim você faz o impossível para sempre me ajudar. Obrigada por me mostrar um mundo mais alegre e divertido, que vai muito mais além de uma tese... Obrigada também por ter me ajudado no momento mais difícil da minha vida, sem você eu não teria conseguido superar.

Agradeço a minha irmã Lorena, que também sempre me apoia, e sempre está na torcida pelas minhas vitórias. Obrigada pelos seus conselhos e pelo seu exemplo de força e coragem.

Agradeço a nova família que tenho, a Mariluci, o Antônio, Débora, Carol, Willian, Felipe, Adrielle, as tias, a vó Clara, o vô Zezinho, os primos. Obrigada por serem tão presentes, por sempre me apoiarem e me mostrarem que aniversário precisa ser comemorado.

Agradeço o Cristian por me coorientar, e me ajudar em tudo que precisei durante o tempo que estive na Politecnico di Milano. Obrigada por me receber, me ensinar e me mostrar sua paixão pela óptica. Sou infinitamente grata a você.

Agradeço a Rocio, a Lucia, o Giulio, por terem me ajudado o tempo todo que estive na Polimi. Agradeço a Rocio e a Lucia por serem grandes amigas e por me ensinarem tudo que sei hoje de óptica, sem vocês esse trabalho não seria possível. Obrigada também por me mostrarem a Itália, a comida, enfim, tudo foi mais leve por causa de vocês. Espero que possamos nos reencontrar algum dia.

Agradeço o Franco e o Tetsuhiko por todos os conselhos e discussões sobre meu trabalho. Obrigada por me ajudarem e darem os puxões de orelha que precisei. Obrigada também pelos momentos de discontrações. Vocês são grandes amigos.

Agradeço os amigos que fiz na física, Ana Clara, Dani, Filó, Leo, Itapecerica, Hobbit, Luana, Gladystone, Egleidson, Gabi, Paresqui, Nestor, Nat, enfim são muitos e não tem como listar todos. Obrigada pelas conversas e diversões, pela amizade, sem vocês teria sido muito pesado. Obrigada Leo, em especial por me ajudar com meu trabalho também, por entender minha limitação com programação, e tirar o seu tempo pra me ensinar. Nem sei como te agradecer, sem você a programação seria um trabalho muito chato.

Agradeço os professores que tive na Física. Todos foram fundamentais na minha formação e agradeço imensamente pelo conhecimento dividido. Agradeço em especial o Mario e o Emmanuel pela dedicação excepcional que vocês tem com os alunos, pelas aulas encantadoras, e pelo exemplo que vocês deixam. Obrigada Mario pela sua amizade, pelos conselhos e pelas conversas da vida, do universo e tudo mais.

Agradeço as meninas da biblioteca, que tornam aquele espaço tão especial e aconchegante. Em especial agradeço a Shirley que sempre estará no meu coração, obrigada por me ajudar em tudo, pela amizade que vou levar para a vida toda. Obrigada Gislene pelo seu trababalho na biblioteca, obrigada por ser sempre atenciosa.

Agradeço as meninas da secretaria pelo trabalho dedicado e por estarem sempre disponíveis. Obrigada por tudo.

Agradeço a UFMG, CNPq, FAPEMIG, CAPES (em especial pela bolsa doutorado sanduíche), INCT Nanomateriais de Carbono e todos os demais órgãos de fomento que contribuíram para que este trabalho fosse possível.

Abstract

This work has two main focuses, the study of ultrafast phenomena on biomolecules and the development of optical setups for hyperspectral imaging. The project was developed in partnership with the university Politecnico di Milano, as part of a Ph.D. sandwich internship. We performed pump-probe measurements and also *ab initio* calculations to study the photophysical and photochemical processes of three aromatic amino acids: tryptophan, tyrosine, and phenylalanine. The results reveal ultrafast electron transfer from singlet to triplet states and photoproducts formation. We complemented the photoexcitation amino acid studies with linear absorption and photoluminescence measurements. In parallel, we developed two optical setups for hyperspectral imaging using a birefringent interferometer. Both setups allow us to obtain images that have not only the spatial but also the spectral information point by point in the image. The first one was designed for macro applications and the other for microscopic applications. The technique brings a novel way to acquire the hyperspectral images, based on an interferometric gadget called TWINS (Translating-Wedge-based Identical pulses eNcoding System). The TWINS is used to generate two replicas of the spectral information emitted by the sample, e. g. the reflectance or photoluminescence, one delayed in respect to the other. Then the interference pattern is generated by projecting the replicas to a common polarization and precisely controlling the delay between them that are detected by a camera. After computing the Fourier transform of the interferogram, we access the spectrum at each point of the image. With the hyperspectral camera, projected for macroscopic applications, we explored its potential in art and conservation, and with the hyperspectral microscope, we explored applications to study biological samples.

Keywords: Ultrafast Phenomena, Pump-probe, Tryptophan, Tyrosine, Phenylalanine, Singlet States, Triplet States, Photoproducts, Hyperspectral Imaging, Birefringence, TWINS, Interferogram, Fourier Transform, Hyperspectral Camera, Hyperspectral Microscope.

Resumo

Este trabalho tem como principais focos o estudo de fenômenos ultrarrápidos em biomoléculas e o desenvolvimento de montagens ópticas para imageamento hiperespectral. Parte do projeto foi desenvolvido em colaboração com a Universidade Politecnico di Milano, durante estágio Doutorado Sanduíche. Para o estudo dos fenômenos ultrarrápidos, utilizou-se principalmente de medidas do tipo excitação e prova (do inglês pump-probe) e de simulações computacionais por primeiros princípios para compreender os fenômenos fotoquímicos e fotofísicos de três aminoácidos aromáticos: triptofano, tirosina e fenilalanina. Os resultados obtidos demonstraram tempos ultra-rápidos de transferência de elétrons dos estados singletos para os tripletos e a formação de fotoprodutos. Complementamos os estudos de fotoexcitação dos aminoácidos com medidas de absorção linear e fotoluminescência. Em paralelo, desenvolvemos duas montagens ópticas para a obtenção de imagens hiperespectrais utilizando interferômetro baseado em birrefringência. Ambas são capazes de obter imagens do objeto de interesse que contém além da informação espacial, a informação espectral emitida pelo objeto contida em cada ponto da imagem. Uma montagem foi projetada para aplicações macro e a outra para aplicações microscópicas. A novidade da técnica está no modo de aquisição das imagens, que se baseia num dispositivo interferométrico birrefringente, o TWINS (do inglês: Translating-Wedge-based Identical pulses eNcoding System). O TWINS foi utilizado para gerar duas réplicas da informação espectral emitida pelo objeto (a refletância ou fotoluminescência, por exemplo), uma atrasada em relação a outra, bem como o padrão de interferência gerado pela combinação dessas devido a este atraso controlado, que é detectado por uma câmera. Após computarmos a transformada de Fourier do interferograma, obtemos acesso ao espectro ponto a ponto na imagem. Na câmera hiperespectral, projetada para aplicações macroscópicas, exploramos sua aplicação principalmente em arte e conservação. Já com o microscópio hiperespectral, exploramos principalmente sua aplicação em sistemas de tecidos biológicos.

Palavras-chave: Fenômenos Ultrarrápidos, Pump-probe, Triptofano, Tirosina, Fenilalanina, Estados Singletos, Estados Tripletos, Fotoprodutos, Imageamento Hiperespectral, Birrefringência, TWINS, Interferograma, Transformada de Fourier, Câmera Hiperespectral, Microscópio Hiperespectral.

List of Figures

Figure 1 – Schematic Figure for the Classical Treatment of Light-Matter Interaction. 19
Figure 2 – Graph Showing the Dependence of the Refractive Index with the Frequency of Light 21
Figure 3 – Schematic Diagram of Second-Harmonic Generation. 24
Figure 4 – Phase-Matching Using Birefringence in a Second-Harmonic Generation Process. 25
Figure 5 – Schematic Diagram of Third-Harmonic Generation. 26
Figure 6 – Schematic figure of a WLC Spectrum Generated in Sapphire Plates. . . 27
Figure 7 – Birefringence in a Calcite Crystal. 28
Figure 8 – Cross-Section of the Refractive Index Ellipsoid of a Positive Uniaxial Crystal. 29
Figure 9 – Schematic Setup of the TWINS device. 30
Figure 10 – Schematic Configuration for Pump-Probe Measurements. 34
Figure 11 – The Main Signals that can be Detected in a Pump-Probe Experiment. 35
Figure 12 – Pump-Probe Experimental Setup. 36
Figure 13 – Schematic Drawing of a Hyperspectral Datacube with Different Acquisition Modes. 38
Figure 14 – Schematic Setup of the Hyperspectral Camera. 39
Figure 15 – Optical Path of One Generic Ray that Impinges the Two Birefringent Plates at Angle α. 40
Figure 16 – Phase Difference Accumulated by the Two Polarization Components of a Ray that Passes Through a Birefringent Crystal. 41
Figure 17 – Visibility of the Interferogram as Function of the Phase Spread. 43
Figure 18 – Schematic Setup of the Hyperspectral Imaging Microscope. 45
Figure 19 – Schematic Configuration for a Uniform Excitation of the Samples in the Hyperspectral Microscope. 45
Figure 20 – General Structure of an Amino Acid. 46
Figure 21 – Aromatic Amino Acids Molecular Structure. 47
Figure 22 – Titration Curve of Glycine. 47
Figure 23 – Egg and Granuloma Structure of *Schistosoma Mansoni* in Histological Section of Mouse Liver. 49
Figure 24 – Linear Absorption Spectrum of the Aromatic Amino Acids. 50
Figure 25 – Photoluminescence Spectra of Tryptophan and Phenylalanine. 51
Figure 26 – Photoluminescence from steady-state fluorescence and the decay associated spectra (DAS) from time-resolved fluorescence of tyrosine in water at pH 5.5. 52

Figure 27 – Transient Absorption of Trp in phosphate buffer saline, pH 7.4, after excitation at 266 nm. 54
Figure 28 – Linear Absorption Spectra and Vertical Excitation from the Ground State for Tryptophan. 55
Figure 29 – Photoinduced Absorptions and Stimulated Emissions Calculations for Tryptophan in Water. 56
Figure 30 – Transient Absorption of Tryptophan After Excitation at 285 nm. . . . 57
Figure 31 – Schematic Drawing for Tryptophan Deactivation Processes in Neutral pH. 58
Figure 32 – Photoinduced Absorption Calculations for the Protonated Form of Tryptophan. 59
Figure 33 – Linear Absorption Spectrum for Tryptophan in Acid and Neutral Medium. 60
Figure 34 – Transient Absorption of Trp in Hydrochloric Acid Aqueous Solution, pH 1.0, After Excitation at 266 nm. 60
Figure 35 – Tryptophan Transient Absorption Spectrum at pH 7.4 in comparison to Tryptophan at pH 1.0. 61
Figure 36 – Absorption Spectrum of Tyrosine Obtained via TDDFT in Comparison with our Linear Absorption Spectrum Measured in different pHs. . . . 62
Figure 37 – Transient Absorption of Tyr in Phosphate Buffer Saline, pH 7.4, After Excitation at 266 nm. 63
Figure 38 – Time-resolved Absorption Spectra Extracted from the 2D map for 100 fs to 1.5 ns of Tyr in Phosphate Buffer Saline, pH 7.4. 64
Figure 39 – Transient Absorption of Tyr in HCl Aqueous Solution, pH 1.0, After Excitation at 266 nm. 65
Figure 40 – Transient Absorption of Phe in Phosphate Buffer Saline, pH 7.4, After Excitation at 266 nm. 67
Figure 41 – Transient Absorption of Phe in Hydrochloric Acid Aqueous Solution, pH 1.0, After Excitation at 266 nm. 68
Figure 42 – Optical Characterization of the Hyperspectral Camera. 71
Figure 43 – Hyperspectral imaging of the Egyptian cartonnage. 72
Figure 44 – Hyperspectral Microscope Image of a Smartphone Digital Display. . . . 73
Figure 45 – Hyperspectral Fluorescence Image of Rhodamine 6G Mixed with Green Beads Solutions Deposited in a Paper. 74
Figure 46 – Hyperspectral Microscope Fluorescence Images of Mechanically Exfoliated WS_2 flakes. 75
Figure 47 – Normalized Photoluminescence Spectra of Mechanically Exfoliated WS_2 Flakes. 76
Figure 48 – Autofluorescence Hyperspectral Imaging of a Mouse Liver from an Uninfected Sample. 77

Figure 49 – Representative Autofluorescence Hyperspectral Imaging of the Mouse Livers Infected with *S. Mansoni* 78
Figure 50 – Representative Autofluorescence Hyperspectral Imaging of the Mouse Livers Showing the Evolution of the Disease. 79
Figure 51 – Linear Absorption Spectrum of the Aromatic Amino Acids at pH 5.35. 92
Figure 52 – Transient absorption of Trp in a buffer solution, pH 5.35, after excitation at 266 nm. 93
Figure 53 – Transient absorption of Tyr in a buffer solution, pH 5.35, after excitation at 266 nm. 93
Figure 54 – Transient absorption of Phe in a buffer solution, pH 5.35, after excitation at 266 nm. 94
Figure 55 – Transient Absorption of Tryptophan in HCl Aqueous Solution with Parallel and Perpendicular Polarization. 96
Figure 56 – Transient Absorption of Tyrosine in HCl Aqueous Solution with Parallel and Perpendicular Polarization. 96
Figure 57 – Transient Absorption of Phenylalanine in HCl Aqueous Solution with Parallel and Perpendicular Polarization. 97

List of Abbreviations

$\Delta T/T(\tau)$ differential transmission signal

Phe phenylalanine neutral species

$Phe+$ phenylalanine pronotonated species

Trp neutral tryptophan

$Trp+$ protonated tryptophan

ESA excited state absorption

FT Fourier transform

FW fundamental wavelength

GSB ground state bleaching

GVD group velocity dispersion

HCl hydrochloric acid

HSI hyperspectral imaging

IC internal conversion

ISC intersystem crossing

LA linear absorption

OMA optical multichannel analyzer

OS oscillator strength

PA photoinduced absorption

PBS phosphate buffer saline

pI isoelectric pH or isoelectric point

PL photoluminescence

QM/MM quantum mechanics/molecular mechanics

SE stimulated emission

SFG sum-frequency generation

SHG second-harmonic generation

TDDFT time-depend density functional theory

THG third-harmonic generation

TWINS Translating-Wedge-based Identical pulses eNcoding System

UV ultraviolet

WLC white light continuum

WS_2 tungsten disulfide

Contents

1 INTRODUCTION 15

2 OPTICAL PROCESSES 17
2.1 Propagation of Electromagnetic Waves 17
2.2 Dispersion 18
2.3 Nonlinear Optical Processes 22
2.3.1 Second-Harmonic Generation 23
2.3.2 Third-Harmonic Generation 25
2.3.3 Supercontinuum Generation 26
2.4 Birefringence and the TWINS 28
2.5 Fourier Transform Spectroscopy 31

3 METHODS AND MATERIALS 34
3.1 Methods 34
3.1.1 Pump-probe Spectroscopy 34
3.1.1.1 Third-Harmonic Experimental Setup 36
3.1.2 Theoretical Calculations 37
3.1.3 Hyperspectral Imaging 38
3.1.3.1 Hyperspectral Camera 39
3.1.3.2 Hyperspectral Microscope 44
3.2 Materials 46
3.2.1 Amino Acids[1] 46
3.2.2 Mice Liver Tissues Infected with *Schistosoma Mansoni* 48

4 RESULTS - AMINO ACIDS 50
4.1 Stead-State Absorption 50
4.2 Photoluminescence 51
4.3 Tryptophan 52
4.3.1 State of Art 52
4.3.2 Transient Absorption Measurements 53
4.4 Tyrosine 62
4.4.1 State of Art 62
4.4.2 Transient Absorption Measurements 63
4.5 Phenylalanine 66
4.5.1 State of Art 66
4.5.2 Transient Absorption Measurements 66

5 RESULTS - HYPERSPECTRAL IMAGING 70
5.1 Hyperspectral Camera 70
5.1.1 Spectral and Reflectance Calibration 70
5.1.2 Artworks imaging 71
5.2 Hyperspectral Microscope 72
5.2.1 Spectral Calibration 72
5.2.2 Nanomaterials Imaging 75
5.2.3 Biological Tissue Imaging 76

6 CONCLUSION AND PERSPECTIVES 80

BIBLIOGRAPHY 82

APPENDIX 91

APPENDIX A – AROMATIC AMINO ACIDS 92
A.1 Stead-State Absorption 92
A.2 Transient Absorption Measurements 92
A.2.1 Transient Absorption Measurements with Parallel and Perpendicular Polarization 95

ANNEX 98

ANNEX A – THESIS-RELATED PUBLICATIONS 99

1 Introduction

Over the last decades, the advances in techniques and equipments have changed the way of studies in optics. In particular, the construction of the first ruby laser by Theodore H. Maiman in 1960 has revolutionized the field. And since then, lasers have become increasingly more powerful. Due to this progress, several other areas have also been developed and thus their applications. Through the work developed by Gérard Mourou and Donna Strickland (both winners of the Nobel Prize in Physics in 2018), today we can generate ultra-short and high-intensity optical pulses. Because of that ultrafast phenomena started to play an important role in the understanding of how light interacts with matter.

In this thesis, we will present optical studies about two different subjects, realized in partnership with Politecnico di Milano, that can be seen as independent of each other: the study of molecular systems using ultrafast pump-probe spectroscopy and the development of a hyperspectral imaging device and its applications. This partnership was really important for the progress of our work since time resolved spectroscopy in biomolecules requires an infrastructure with femtoseconds lasers, optical parametric amplifiers, and nonlinear optics to obtain supercontinuum generation, third harmonic processes, and many other optical-equipments that we had access to in Giulio Cerullo's group. We work specifically with three amino acids: tryptophan, phenylalanine and tyrosine. We present our studies based on transient absorption and photoluminescence measurements and theoretical modeling the systems for a better understanding of their ultrafast optical processes. The photophysics (excitation and deactivation processes, with and without light) and photochemistry (chemical reactions induced by light) of these molecules have been widely studied. [1] Their distinctive feature, absorption (and fluorescence) in the UV (VIS) range, among the other amino acids constituents of the proteins, are often used to study protein structure and function. [2] Due to the high influence of local interactions in these molecules, a complete understanding of their excited states and deactivation processes is lacking. The understanding of the photophysical and photochemical processes of these three amino acids it is a key to better comprehend the general factors that govern protein fluorescence, and with that, provide more information for the studies of protein functions, folding, and dynamics.

In addition, under the supervision of Cristian Manzoni, we had the opportunity to develop a new device with many applications, some of them in areas of great interest for ongoing projects in the Biophotonics Laboratory at Universidade Federal de Minas Gerais. Hyperspectral Imaging systems are powerful tools that are able to provide spectral and spatial information of a sample. This technique has been applied in different fields since it started in remote sensing [3] in the early 1970s, and nowadays it is found in

other subjects such as forensic [4], food processing [5], artwork [6], biomedicine [7], etc. We developed and assembled a hyperspectral camera and a hyperspectral microscope based on a birefringent interferometer. We present a robust and stable system, capable to extract and store information acquired in the form of a datacube, containing spatial and spectral data of the samples. The efficiency and reliability of the system were confirmed by measurements and comparison with well-established spectrometers. We then present its applications in arts, solid state and biological systems.

This thesis is organized as the following: in Chapter 2 we present a brief review about the optical processes that are involved in the experimental techniques used in this work; in Chapter 3 we describe the setups and the studied materials; in Chapter 4 and 5 we present the results for the amino acids and the hyperspectral imaging respectively, and in Chapter 6 we present the conclusions and perspectives. In Appendix A it is presented some complementary measurements for the amino acids and in Annex A it is included the papers related to this thesis that were published during the Ph.D.

2 Optical Processes

In this chapter is presented a brief theoretical review of the optical processes used in the experimental techniques described in this thesis.

2.1 Propagation of Electromagnetic Waves

The Maxwell's equations and the Lorentz force law together form the basis of electromagnetism. Inside a medium, in regions with absence of free charges or currents, the Maxwell's equations can be expressed in the differencial forms as:

$$\left.\begin{array}{ll} \nabla \cdot \mathbf{D} = 0, & \nabla \times \mathbf{E} = -\frac{\partial \mathbf{B}}{\partial t}, \\ \nabla \cdot \mathbf{B} = 0, & \nabla \times \mathbf{H} = \frac{\partial \mathbf{D}}{\partial t}. \end{array}\right\} \tag{2.1}$$

in which $\mathbf{E}$ is the electric field, $\mathbf{B}$ is the magnetic field, $\mathbf{D} = \epsilon_0\mathbf{E} + \mathbf{P}$ is the electric displacement, and $\mathbf{H} = \mathbf{B}/\mu_0 - \mathbf{M}$ ($\mathbf{H}$ is also called "magnetizing force" or "auxiliary field"). The electric polarization ($\mathbf{P}$) and the magnetization ($\mathbf{M}$) are the medium's response to the presence of the electric and the magnectic fields, respectively. Initially, we will assume that the material is linear, isotropic, and homogeneous. "Linearity" means that the response of the medium to an incident electric field varies proportionally with this electric field. "Isotropic" medium means that it does not change the response with the electric field orientation, while the properties of a "homogeneous" medium do not vary along the entire medium. [8]

We can take the curl of both sides of Faraday's and Ampere's laws to obtain partial second-order differential equations for $\mathbf{E}$ and $\mathbf{B}$:

$$\nabla \times \nabla \times \mathbf{E} = -\frac{\partial}{\partial t}\nabla \times \mathbf{B}$$

$$\nabla(\nabla . \mathbf{E}) - \nabla^2\mathbf{E} = -\mu\frac{\partial^2\mathbf{D}}{\partial t^2}. \tag{2.2}$$

With the assumption of a homogeneous medium, thus $\nabla . \mathbf{P} = 0$, which implies in $\nabla . \mathbf{E} = 0$, therefore we have:

$$\nabla^2\mathbf{E} = \mu\epsilon\frac{\partial^2\mathbf{E}}{\partial t^2}, \tag{2.3}$$

and with the same approach in the Ampere's law, we get:

$$\nabla^2\mathbf{B} = \mu\epsilon\frac{\partial^2\mathbf{B}}{\partial t^2}. \tag{2.4}$$

In this way each component of $\mathbf{E}$ and $\mathbf{B}$ obeys a wave equation that propagates within the linear and homogenous material with the phase velocity v:

$$v = \frac{1}{\sqrt{\mu\epsilon}} = \frac{c}{n}, \tag{2.5}$$

$$n = \sqrt{\frac{\mu\epsilon}{\mu_0\epsilon_0}} \cong \sqrt{\frac{\epsilon}{\epsilon_0}}, \tag{2.6}$$

in which n is the refractive index of the material. We have assumed that the dielectric constant, ϵ_r, is a constant characteristic of each material and consequently the n of the material is also so. This is a good approximation for substances such as gases with a simple chemical structure which do not disperse light substantially. On the other hand, there is a strong deviation from the formula, $n = \sqrt{\epsilon_r}$, for many solid bodies (glasses), and for some liquids. For these materials it is necessary to introduce the notion of frequency-dependent dielectric constant, $\epsilon_r(\omega)$, which will imply in the dependence on the refractive index with the frequency, $n(\omega)$(this will be shown and discussed in section 2.2). [9]

We have started the discussion analyzing the propagation of light in a linear medium where the induced polarization is proportional to the applied electric field. In the following section 2.3 we will see that it does not apply to cases when a very intense electric field is applied, since the polarization density starts to act as a source of radiation itself, generating new fields with different phases and frequencies from those of the driving field.

2.2 Dispersion

From Maxwell's equation we obtained a general wave equation for the electric field $\mathbf{E}$, equation 2.3. To describe the propagation of light in a nonmagnectic ($\mu \approx \mu_0, c = 1/\sqrt{\mu_0\epsilon_0}$) and electrically neutral media, we can express the same equation in a way to point out the macroscopic polarization $\mathbf{P}$ of the medium:

$$\nabla^2\mathbf{E} + \mu_0\epsilon_0\frac{\partial^2\mathbf{E}}{\partial t^2} = -\mu_0\frac{\partial^2\mathbf{P}}{\partial t^2}. \tag{2.7}$$

In the case of a nonconducting media, the polarization term ($-\mu_0\partial^2\mathbf{P}/\partial t^2$) is the source term. It is responsible for many optical effects, including dispersion, absorption, double refraction, and others. In optics, dispersion means that the phase velocity of the wave will depend on its frequency in such a way that the refractive index of the medium will not be constant anymore and will be also dependent on the frequency. Indeed, while a monochromatic wave of frequency ω travels at the phase velocity v_p:

$$v_p = \frac{\omega}{k(\omega)} = \frac{c}{n(\omega)}, \tag{2.8}$$

it is the superposition of many waves with different phase velocities that leads to a wave packet (pulse) propagating with the group veocity v_g: [10]

$$v_g = \frac{\partial\omega}{\partial k}. \tag{2.9}$$

To go further, we need a model that describes the response of electrons in the isotropic material due to the interaction with the applied electric field. As all classic models

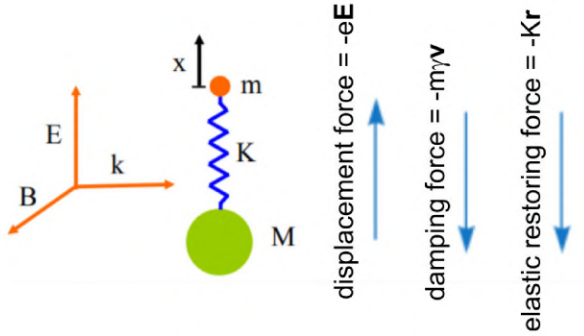


Figure 1 – Schematic figure for the classical treatment of light-matter interaction. In this model the atoms are described as linear oscillators formed by a heavy positive core and an outer electron, which are undergoing a forced oscillation under the influence of an incident electromagnetic wave. This figure was adapted from the reference [11].

it is only a good approximation of reality, nevertheless it describes qualitatively well this optical phenomenon [12]. It assumes that all molecules in the medium are identical, each one having active electrons subject to an elastic restoring force that keeps them bound to their respective molecule. Besides that we will assume that there is a frictional damping force that dissipates energy, as illustrated in Fig.1. In this way, each electron (charge $-e$), in the material is displaced from its equilibrium position by a distance $\mathbf{r}$, resulting in a macroscopic polarization $\mathbf{P}$ of the medium that is given by:

$$\mathbf{P} = -Ne\mathbf{r}, \tag{2.10}$$

in which N is the number of electrons per unit volume. The bound electrons in this classical damped harmonic oscillator model will be submitted to an external force impressed by the oscillating electric field $\mathbf{E}$, resulting in the motion equations:

$$\begin{aligned} m\frac{d^2\mathbf{r}}{dt^2} + m\gamma\frac{d\mathbf{r}}{dt} + K\mathbf{r} &= -e\mathbf{E}, \\ \frac{d^2\mathbf{r}}{dt^2} + \gamma\frac{d\mathbf{r}}{dt} + \omega_0^2\mathbf{r} &= -\frac{e}{m}\mathbf{E}, \end{aligned} \tag{2.11}$$

in which ω_0 is the effective resonance frequency of the bound electrons, $\omega_0 = \sqrt{K/m}$. Now supposing that the applied electric field varies harmonically with time as the factor $e^{-i\omega t}$, we obtain that:

$$\mathbf{r} = -\frac{e}{m(\omega_0^2 - \omega^2 - i\gamma\omega)}\mathbf{E}. \tag{2.12}$$

Consequently, the polarization $\mathbf{P}$, is given by:

$$\mathbf{P} = \frac{Ne^2}{m(\omega_0^2 - \omega^2 - i\gamma\omega)}\mathbf{E}. \tag{2.13}$$

To show how the polarization affects the propagation of light, we return to the wave equation 2.7 with the expression for $\mathbf{P}$ obtained in eq.2.13:

$$\nabla^2\mathbf{E} = \frac{1}{c^2}\left[1 + \frac{Ne^2}{m\epsilon_0}\frac{1}{(\omega_0^2 - \omega^2 - i\gamma\omega)}\right]\frac{\partial^2\mathbf{E}}{\partial t^2}. \tag{2.14}$$

It admits solutions of the type $\mathbf{E} = \mathbf{E_0} e^{i(\mathscr{K}\cdot\mathbf{r}-\omega t)}$ (called homogenous plane harmonic waves), with:

$$\mathscr{K}^2 = \frac{\omega^2}{c^2}\left[1 + \frac{Ne^2}{m\epsilon_0}\frac{1}{(\omega_0^2 - \omega^2 - i\gamma\omega)}\right]. \tag{2.15}$$

This shows that the wavenumber $\mathscr{K}$ is a complex number which can be expressed in terms of its real and imaginary parts as:

$$\mathscr{K} = k + i\alpha, \tag{2.16}$$

and also the refractive index ($\mathscr{N}$):

$$\mathscr{N} = n + i\kappa, \tag{2.17}$$

with

$$\mathscr{K} = \frac{\omega}{c}\mathscr{N}. \tag{2.18}$$

The fact that $\mathscr{K}$ is a complex number leads to the attenuation of the wave into the material, as the electric field has the following form:

$$\mathbf{E} = \mathbf{E_0} e^{i(\mathscr{K}\cdot\mathbf{r}-\omega t)} = \mathbf{E_0} e^{-\alpha z} e^{i(kz-\omega t)}, \tag{2.19}$$

exhibiting an exponential decay of the wave amplitude with distance into the material by the factor $e^{-\alpha z}$. Since the energy of the wave is proportional to E^2, then the energy varies with distance as $e^{-2\alpha z}$. The term α is called absorption coefficient. The phase factor $e^{i(kz-\omega t)}$ indicates that the harmonic wave travels with phase velocity v_p, as described in eq.2.8.

From the equations 2.15 and 2.18 we have:

$$\mathscr{N}^2 = (n + i\kappa)^2 = 1 + \frac{Ne^2}{m\epsilon_0}\left(\frac{1}{\omega_0^2 - \omega^2 - i\gamma\omega}\right), \tag{2.20}$$

from which the optical parameters n and κ can be found:

$$n^2 - \kappa^2 = 1 + \frac{Ne^2}{m\epsilon_0}\left[\frac{\omega_0^2 - \omega^2}{(\omega_0^2 - \omega^2)^2 + \gamma^2\omega^2}\right],$$

$$2n\kappa = \frac{Ne^2}{m\epsilon_0}\left[\frac{\gamma\omega}{(\omega_0^2 - \omega^2)^2 + \gamma^2\omega^2}\right]. \tag{2.21}$$

The Fig.2 shows the dependence of the real part of the refractive index (n) with the frequency (ω). Far from ω_0, γ is very small what implies cancellation of the imaginary parts of $\mathscr{K}$ and $\mathscr{N}$. This behavior is showed in the graph by the region called normal dispersion. In this region the refractive index increases with frequency (decreases with wavelength). This means that for wavelengths towards the infrared region the refractive index (n) is smaller, hence the phase velocity is greater. If a light pulse is propagated

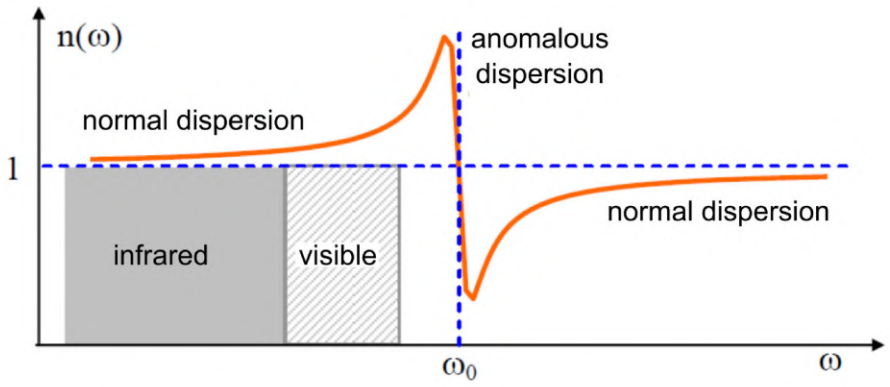


Figure 2 – Graph showing the dependence of the refractive index with the frequency of light near a single resonance line. This grapf was adapted from the reference [11].

through a material when dispersion is present, not only the group velocity will be different to the phase velocity, but it can also vary itself with wavelength. This is known as group velocity dispersion (GVD) and causes a short pulse of light to be broadened where the shorter wavelength components travel slower than the longer wavelength components (for positive group velocity dispersion), also known as chirped pulses. Near to the resonance frequency, $\omega \sim \omega_0$, the denominator in the equation 2.20 is dominated by the term $i\gamma\omega$. The imaginary part of $\mathscr{N}$ dominates leading to the absorption. The dispersion becomes anomalous in the sense that the refractive index decreases with increasing frequency.

In this model we assumed that all electrons were indentically bound, and the system had only one resonance frequency ω_0. To extend the model in order to take into account the fact that there are electrons with different harmonic interactions it is necessary to generalize the expression obtained assuming that there are kinds of electrons (indicated by j) associated with certain resonance frequencies (ω_j) and damping constants (γ_j):

$$\mathscr{N}^2 = 1 + \frac{Ne^2}{m\epsilon_0} \sum_j \left(\frac{f_j}{\omega_{0j}^2 - \omega^2 - i\gamma_j\omega} \right). \tag{2.22}$$

In practice, it is usually used the empirical relation, known as Sellmeier's formula, between the refractive index and the wavelength to describe the dispersion in many transparent materials. In its original and the most general form, the Sellmeier equation is: [12] [11]

$$n^2(\lambda) = 1 + \frac{B_1\lambda^2}{\lambda^2 - C_1} + \frac{B_2\lambda^2}{\lambda^2 - C_2} + \frac{B_3\lambda^2}{\lambda^2 - C_3} + \cdots = 1 + \sum_i \frac{B_i\lambda^2}{\lambda^2 - C_i}. \tag{2.23}$$

Each term of the sum represents an absorption resonance of strength B_i at wavelength $\sqrt{C_i}$, λ is the vacuum wavelength (in micrometers), and B_i and C_i are the Sellmeier's coefficients obtained experimentally. The Sellmeier's coefficients for many common optical materials can be found in the online database [13].

2.3 Nonlinear Optical Processes

The development of lasers with increasingly high power, tunable over a wide frequency range, and with very short pulses enabled the emergence of areas such as nonlinear optics. Nonlinear optical phenomena occur when the response of a given material to the applied electric field depends in a nonlinear way on the strength of electric field. In order to describe the optical nonlinearity, let us first consider the linear response of an isotropic medium to an electric field:

$$\mathbf{D} = \epsilon \mathbf{E}, \tag{2.24}$$

in which $\mathbf{D}$ is the electric displacement vector, $\mathbf{E}$ is the electric field vector, and ϵ is the medium absolute permittivity constant. The response of the medium can also be described by the polarization vector, $\mathbf{P}$:

$$\mathbf{P} = \epsilon_0 \chi \mathbf{E}, \tag{2.25}$$

in which χ is the medium susceptibility, and can be expressed in terms of the absolute permittivity: $\epsilon \equiv \epsilon_0(1+\chi)$, or $\chi = \epsilon_r - 1$.

However, most of the crystals can be easier polarized in some directions than in others, exhibiting their anisotropic characteristic. In this way, the equation 2.24 has to be replaced by a general linear relation where the absolute permittivity constant turns into a tensor:

$$\mathbf{D} = \overleftrightarrow{\epsilon}\mathbf{E}, \tag{2.26}$$

in which

$$\overleftrightarrow{\epsilon} = \begin{vmatrix} \epsilon_{xx} & \epsilon_{xy} & \epsilon_{xz} \\ \epsilon_{yx} & \epsilon_{yy} & \epsilon_{yz} \\ \epsilon_{zx} & \epsilon_{zy} & \epsilon_{zz} \end{vmatrix}.$$

In addition, when intense lights interact with the medium the optical response has to be described by generalizing the equation 2.25 and expressing the induced polarization as a power series in the field strength as:

$$\mathbf{P} = \epsilon_0(\overleftrightarrow{\chi}\mathbf{E} + \overleftrightarrow{\chi}^{(2)}\mathbf{E}\mathbf{E} + \overleftrightarrow{\chi}^{(3)}\mathbf{E}\mathbf{E}\mathbf{E} + ...), \tag{2.27}$$

in which $\overleftrightarrow{\chi}$ is the linear susceptibility tensor, $\overleftrightarrow{\chi}^{(2)}$ is the second-order susceptibility tensor, and so on. These higher-order terms are responsible for the generation of the optical harmonics. In particular, we are interested in the second- and third-order nonlinear optical interactions that are associated with second-harmonic generation, sum-frequency generation, third-harmonic generation and white light continuum generation processes.

In the following subsections we will describe briefly the main nonlinear optical processes that are present in the optical setups we used in this work.

2.3.1 Second-Harmonic Generation

The second-order nonlinearity (and also all even order polarizabilities) is present only in non-centrosymmetric mediums, i.e., in materials that do not have inversion symmetry. Thus, if the medium has inversion symmetry, all the elements of the second-order susceptibility tensor must be zero. [12] In a more general way the material structure reveals how is the form of the optical susceptibility tensor.

The second-order nonlinear susceptibility written in cartesian coordinates,

$$P_i^{(2)} = \sum_{j,k} \epsilon_0 \chi_{ijk}^{(2)} E_j E_k, \tag{2.28}$$

has 27 independent coefficients. But taking into account the permutation symmetry, where the order of terms E_j and E_k in the equation 2.28 is not important, the number of coefficients reduces down to 18. This two dimensional 3×6 tensor is commonly known as the Kleinman d-tensor(d_{eff}) [14]

$$\begin{bmatrix} P_x \\ P_y \\ P_z \end{bmatrix} = 2\epsilon_0 \begin{bmatrix} d_{11} & d_{12} & d_{13} & d_{14} & d_{15} & d_{16} \\ d_{21} & d_{22} & d_{23} & d_{24} & d_{25} & d_{26} \\ d_{31} & d_{32} & d_{33} & d_{34} & d_{35} & d_{36} \end{bmatrix} \begin{bmatrix} E_x^2 \\ E_y^2 \\ E_z^2 \\ 2E_yE_z \\ 2E_xE_z \\ 2E_xE_y \end{bmatrix}$$

There will be other symmetries for crystalline materials and the remaining 18 coefficients are not completely independent of each other.

To discuss the second-harmonic generation (SHG) process we need to consider the nonlinearity up to the second-order term. We are supposing that the incident light is a harmonic wave and for now we will neglect the vector character and the spatial dependence, thus the applied electric field and the response of the crystal are expressed as:

$$E(t) = \frac{1}{2} A e^{-i\omega t} + \frac{1}{2} A^* e^{i\omega t}, \tag{2.29}$$

$$P(t) = [\frac{1}{2}\epsilon_0 \chi A e^{-i\omega t} + c.c.] + [\frac{1}{4}\epsilon_0 \chi^{(2)} A A^*] + [\frac{1}{4}\epsilon_0 \chi^{(2)} A^2 e^{-2i\omega t} + c.c.], \tag{2.30}$$

in which *c.c.* is the complex conjugate. The equation 2.30 shows that the interaction with the electric field may generate nonlinear processes such as optical rectification (zero frequency component) and second-harmonic generation (oscillating contribution at 2ω). [14] In principle all transparent crystals can present a nonlinear response for an intense applied light, but in practice the process will only be efficiently generated due to favorable phase-matching condition. Because the crystal is a dispersive medium, and dispersion means that the refractive index ($n(\omega)$) is a monotonic function of frequency (ω), the SH wave (2ω) will propagate slower than the fundamental wave (ω). This will cause a negative interference between the waves at 2ω and will quench the nonlinear SHG. [15]

As can be seen, in isotropic crystals it is impossible to obtain efficiency in SHG. However, in anysotropic crystals it is possible to achieve phase-matching condition, $n(2\omega) = n(\omega)$, depending on the directions of propagation and polarizations of the ω and 2ω signals. From a corpuscular point of view, it can be seen as a momentum conservation during collisions of photons that for a general nonlinear second-order process would be $\hbar\mathbf{k_3} = \hbar\mathbf{k_2} + \hbar\mathbf{k_1}$ and specifically for SHG, $\hbar\mathbf{k}_{2\omega} = \hbar\mathbf{k}_\omega + \hbar\mathbf{k}_\omega$:

$$\mathbf{k}_{2\omega} = 2\mathbf{k}_\omega,$$
$$\Delta k = \frac{2\omega}{c} n(2\omega) - 2\frac{\omega}{c} n(\omega) = 0, \tag{2.31}$$

and finally:

$$n(2\omega) = n(\omega). \tag{2.32}$$

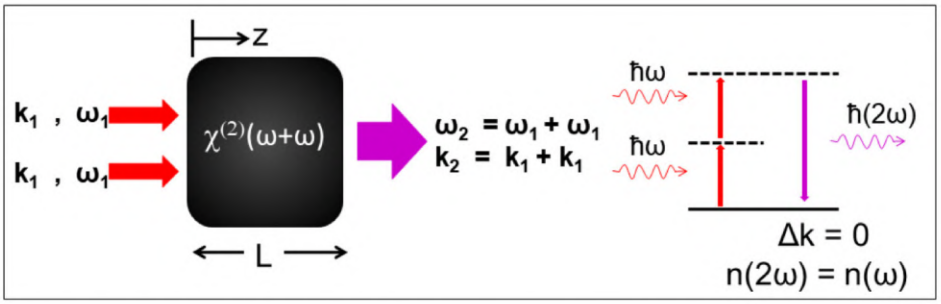


Figure 3 – Schematic diagram of SHG and the energy level diagram. The SHG can be treated as a two-photon reaction. Figure adapted from the reference [14].

In uniaxial crystals for example, there are two different refractive indexes, extraordinary (n_e) and ordinary (n_o) which depend on the light polarization and propagation direction. In fact, the extraordinary refractive index depends on the the angle (θ) between the optical axis of the crystal and the propagation direction of the beam ($\mathbf{k}$) as illustrated in the ellipsoid of indexes in Fig.4. [11] It is possible to achieve the phase-matching condition by tuning the angle θ: $n_e(2\omega, \theta) = n_o(\omega)$. [15] There are two types of phase-matching, Type I and Type II, that are defined by the polarization of the electric fields involved in the process. Then, the crystal can be orientated in such a way that the SH is polarized in the direction that gives it the lowest refractive index. Since in positive uniaxial crystals $n_e > n_o$, then the SH will be polarized in the ordinary index (o) direction and in negative uniaxial crystals ($n_e < n_o$) will be in the extraordinary index (e) direction, as shown in Table 1.

SHG is widely used to extend the choices of wavelengths generated by lasers, and in this way, are the basis of materials research. It is even more efficient for pulsed lasers, which has brought great advances in nonlinear imaging, for example in applications of cancer diagnostics in biological tissues. In our setup it was used to obtain the second-harmonic of the Titanium sapphire laser.

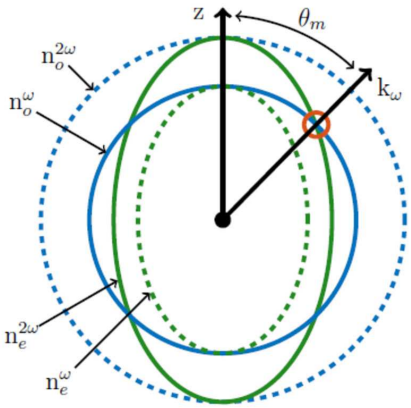


Figure 4 – Phase-matching using birefringence in a second-harmonic generation process. The refractive index ellipsoid of a negative uniaxial crystal shows that tuning the propagation angle θ (between the direction of the beam propagation and the optical axis of the crystal) is possible to achieve the condition: $n_e(2\omega, \theta) = n_o(\omega)$. Figure extracted from the reference [16].

Table 1 – Phase-matching condition for different electric fields polarization in a negative uniaxial crystal (on the left) and in a positive uniaxial crystal (on the right). The ordinary polarization is represented with an (o) and the extraordinary polarization with an (e).

	ω	ω	2ω
Type I	o	o	e
Type II	o	e	e

	ω	ω	2ω
Type I	e	e	o
Type II	o	e	o

2.3.2 Third-Harmonic Generation

The third-harmonic frequency can be obtained by a three photon reaction ($\omega + \omega + \omega = 3\omega$) in a $\chi^{(3)}$ crystal but, this process has much lower probability than a two-photon reaction. Then, to obtain the third-harmonic (TH) frequency of the Ti:sapphire laser we did it in a two steps procedure. First we generated the second-harmonic, $\omega + \omega = 2\omega$, after that the SH and the fundamental were combined by sum frequency generation in a $\chi^{(2)}(2\omega + \omega)$ crystal to produce the TH. This process is represented in Fig.5. Similarly to the SHG the phase-matching condition ($\Delta k = 0$) cannot be satisfied in isotropic crystals (since $n(\omega_3) > n(\omega_1), n(\omega_2)$). However, in uniaxial crystals for example, chosing the propagation direction and the polarization of the beams $(\omega_1, \omega_2, \omega_3)$ properly, we can achieve the phase-matching condition: [14]

$$\Delta k = k_3 - k_1 - k_2 = 0, \tag{2.33}$$

and from energy conservation, we have that:

$$\omega_3 = \omega_1 + \omega_2, \tag{2.34}$$

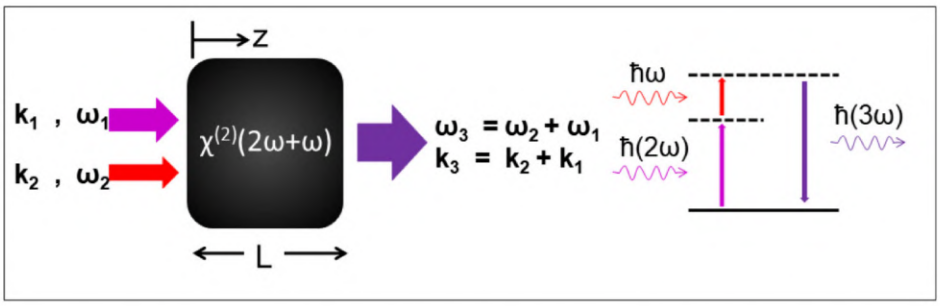


Figure 5 – Schematic diagram of third-harmonic generation (THG) and the energy level diagram. The THG is obtained by a sum-frequency generation in another crystal after the second-harmonic generation has generated in a first nonlinear crystal since they did not share the same phase-matching condition. Figure adapted from the reference [14].

which shows us that:

$$\frac{\omega_1}{c}[n(\omega_3) - n(\omega_1)] + \frac{\omega_2}{c}[n(\omega_3) - n(\omega_2)] = 0$$
$$n(3\omega) = \frac{n(\omega)}{3} + \frac{2n(2\omega)}{3} \tag{2.35}$$

In Type I synchronism condition for negative uniaxial crystals, the SH and the fundamental may have the same polarization, for example ordinary polarization, then the sum wave, at 3ω, must have perpendicular polarization with respect to the primary waves, extraordinary polarization.

In this way, we obtained UV pulses and could excite the three aromatic amino acids and obtain their photoinduced and deactivation processes in the UV range. The transient absorption measurements of tryptophan, tyrosine and phenylalanine are shown in Chapter 4.

2.3.3 Supercontinuum Generation

White light continuum (WLC) generation, or supercontinuum generation, is a third-order nonlinear process ($\chi^{(3)}$) that has been observed in a variety of transparent media [17]. The general result is a spectral broadening of the pulse. For a pulse with spectrum center initially in the near infrared, it expands covering from the infrared to the visible range, as shown in the top of Fig.6. In Fig.6, we also show a typical WLC spectrum generated by focusing 800 nm (central wavelength), 120 fs pulses in a 1 mm and 2 mm thick sapphire plate. Besides an intense residual peak at the driving pulse wavelength, two broad continua are generated to the blue and red regions of the spectrum.

WLC generation results from an ultrashort intense pulse subjected to many nonlinear processes and is far from being well understood. [17] It is a nonlinear optical process that involves temporal, such as self-phase modulation, dispersion, self-steepening,

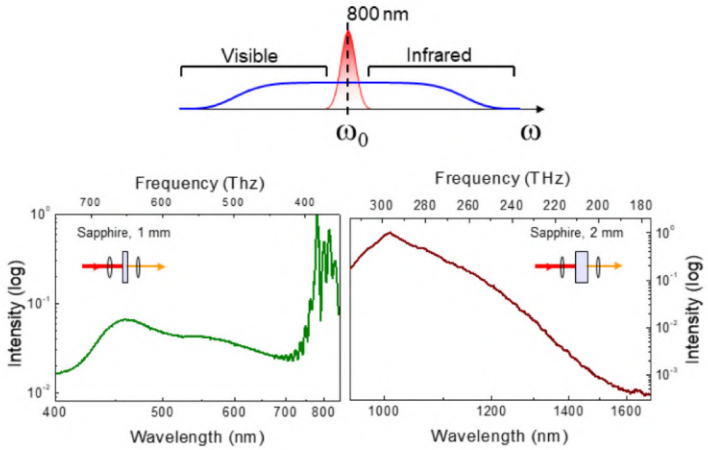


Figure 6 – Schematic figure of a WLC spectrum generated by a 800 nm pulse (top) and the obtained spectra in 1 mm and 2 mm sapphire plates (bottom). The figure was adapted from the reference [18].

and spatial, such as self-focusing, difraction, and other aspects. [18] The description of all these processes is out of the scope of this thesis and a better understanding of the mechanisms behind the WLC generation can be found in the literature [19] [20]. Briefly, it is triggered by self-phase modulation of the pulse and arises from the nonlinearity of the refractive index of the material (Kerr medium - $\chi^{(3)}$ dominant). In such materials the refractive index depends on the intensity of the light:

$$n(t) = n_0 + n_2 I(z,t). \tag{2.36}$$

When a laser pulse propagates over a distance L in this material it accumulates a nonlinear phase (φ):

$$\varphi(t) = \omega_0 t - \frac{\omega_0}{c} n(t) L. \tag{2.37}$$

This phase shift due to the variation of the refractive index ($n(t)$) results in a frequency shift of the pulse. The instantaneous frequency ($\omega(t)$) is given by:

$$\omega(t) = \frac{d\varphi(t)}{dt} = \omega_0 \left(1 - \frac{n_2 L}{c} \frac{dI}{dt}\right). \tag{2.38}$$

From the last equation we can see that the self-phase modulation leads to a broadening in the spectrum of the pulse. The front of the pulse (positive slope $dI/dt > 0$) generates redder frequencies (lower frequencies) and the back (negative slope $dI/dt < 0$) generates bluer frequencies (higher frequencies) than the central wavelength of the pulse.

In this thesis WLC generation in 3 mm CaF_2 crystal was used as probe pulses in the transient absorption experiments.

2.4 Birefringence and the TWINS

In this section we will describe the birefringence process and its use in the device developed by the researchers at the Politecnico di Milano, called Translating-Wedge-based Identical pulses eNcoding System (TWINS).

Birefringence is an optical property of a crystal that shows the dependency of the refractive index with the polarization and propagation direction of light. The most explored example is the calcite crystal as illustrated in Fig.7. When unpolarized light is refracted by

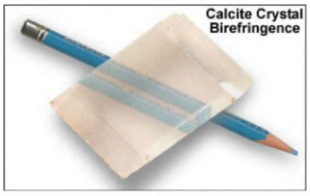


Figure 7 – In a naturally birefringent crystal such as calcite it is possible to see the double refraction from an object showing the split of the light into two separate rays travelling at different speeds. Figure extracted from the reference [21].

a birefringent crystal, the refraction angle becomes dependent on the polarization direction of the light. For a non-normal incidence in the surface, the unpolarized light can be split into two linearly polarized light beams. Because of that the object that is illuminated with the unpolarized light is viewed through the birefringent crystal as a twin image slightly displaced.

This ordinary optical property depends on the cristalline geometry of the material and can be separated into uniaxial and biaxial crystals. The last ones present three refractive indices $(n_\alpha, n_\beta, n_\gamma)$ corresponding to three principal axes of the crystal and two optical axes which light may propagate along independent of polarization. We will focus our attention to the uniaxial birefringent crystals, since the TWINS device that will be presented hereafter is based on them. These crystals have two refractive indexes for different light polarization, the ordinary index n_o and the extraordinary index n_e and one optical axis. For positive uniaxial crystals $n_o < n_e$ and for the opposite relation they are called negative uniaxial crystals.

In Fig.8 we show a geometric way that allows finding the refractive index for a light propagating in any $\hat{\mathbf{k}}$ direction (unity length vector in the wave vector $\mathbf{k}$ direction). [22] The refractive index "seen" by the beam propagating in the crystal depends on its propagation direction and polarization. Thus, a beam propagating in the $\hat{\mathbf{k}}$ direction exhibits two normal polarizations states, one perpendicular to the optical axis, the ordinary polarization, and one in the (Y,Z) plane, the extraordinary polarization. The ordinary polarization propagates with refractive index n_o and the extraordinary polarization propagates with refractive index $n_e(\theta)$ that varies from n_o $(\theta = 0)$ to n_e $(\theta = 90°)$ as a function of the

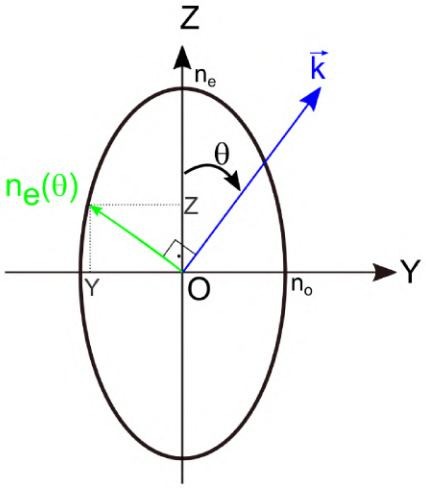


Figure 8 – Cross-section of the refractive index ellipsoid of a positive uniaxial crystal. In this notation $n_o \equiv n_x = n_y$ is called ordinary refractive index; $n_e \equiv n_z$ is called extraordinary refractive index; the Z axis is the optic axis of the crystal. The $n_e(\theta)$ is the refractive index seen by extraordinary polarized component of a planar wave propagating in the crystal in the $\hat{\mathbf{k}}$ direction. Figure adapted from the reference [22].

propagation angle θ:

$$\frac{1}{[n_e(\theta)]^2} = \frac{\cos^2(\theta)}{n_o^2} + \frac{\sin^2(\theta)}{n_e^2}. \tag{2.39}$$

One example of negative uniaxial crystal that has been applied for the manufacture of polarizer, time delay compensator plate, and other birefringent device is the α-BBO (α-BaB_2O_4). It has large birefringence over a broad transparent range from 190 nm to 3500 nm. [23] At Politecnico di Milano these crystals play an important role in two-dimensional spectroscopy where the researchers developed the novel device called TWINS, based on α-BBO birefringent crystals. [24] [25] [26] They also showed another application for the TWINS device, as an interferometer, where it is used to replace Michelson interferometers in Fourier transform spectroscopy covering from infrared upto the visible range. [27] [28]

The concept of using the birefringent crystals to obtain an interferometer is our main interest in this device. As illustrated in Fig.9, it consists of two birefringent blocks (one with adjustable thickness made by one translating wedge), both made of α-BBO with optical axes rotated by 90° with respect to each other and perpendicular to the propagation direction of the beam. In addition there are two polarizers placed one in the front and the other at the end of the blocks sequence, set with the polarization axis at 45° to the blocks ordinary and extraordinary axes. When a pulse polarized at 45° with respect to the ordinary and extraordinary axes of the first fixed thickness plate propagates through the system, it splits into two perpendicular polarized pulses with same intensity. This means that the first block introduces a fixed delay between the replicas of the pulse in which one component propagates along the fast axis (n_e) and the other along the slow

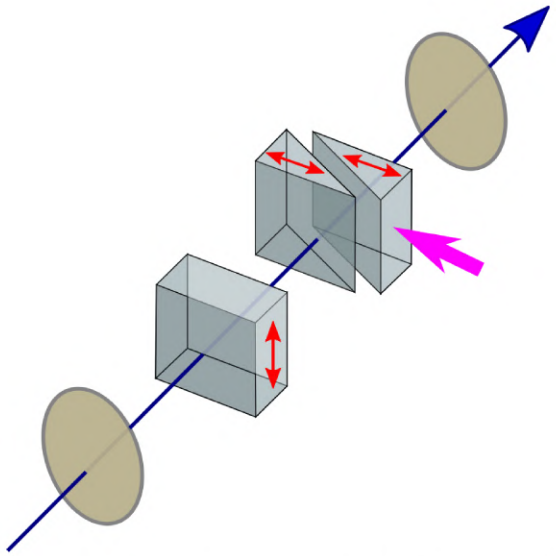


Figure 9 – Schematic setup of the TWINS device.

axis (n_o) of the material. The second plate is a pair of wedges in which one of them moves (inserting material in and out in the optical path) to change the final thickness of the block in order to controll with precision the delay between the replicas. When translating one of the wedges by Δl the time delay between the two replicas is given by:

$$\Delta\tau_{TWINS} = \left(\frac{1}{v_{ge}} - \frac{1}{v_{go}}\right)\Delta l \tan(\alpha), \tag{2.40}$$

in which α is the apex angle of the wedges, v_{ge} and v_{go} are the group velocity of the extraordinary and ordinary polarization, respectively. After the wedge sequence, the last polarizer projects the two delayed and orthogonal replicas to a common linear polarization giving rise to a interferogram.

It should be noted that due to chromatic dispersion, the group refractive index of the ordinary (n_{go}) and extraordinary (n_{ge}) polarization are wavelength dependent, thus for each position in translating the wedge the delays experienced by the different spectral components are different. The group velocity mismatch (GVM $= 1/v_{ge} - 1/v_{go}$) and also the birefringence (Δn) of α-BBO according to the wavelength is showed in Table 2. Because of this nonlinear dependence on wavelength, to apply the TWINS setup as a Fourier transform (FT) spectrometer it is necessary a calibration of the wavelength axis. This can be easily done by measuring and interpolating known wavelengths spectrum of color filters through the setup.

The spectral resolution is inversely proportional to time delay introduced between the replicas which show us that the maximum spectral resolution is obtained with the maximum translation of the wedge (only limited by the available lateral size of the wedge, L). Higher resolution could be achieved by using either a material with lager birefringence

Table 2 – α-BBO refractive indices n_o and n_e, birefringence Δn, and group velocity mismatch (GVM). The data was obtained from the reference [25]

$\lambda(nm)$	n_o	n_e	Δn	GVM (fs/mm)
1100	1.6573	1.5374	0.1199	402.5
900	1.6623	1.5410	0.1203	411.0
700	1.6674	1.5460	0.1215	427.1
500	1.6807	1.5557	0.1250	468.2
300	1.7342	1.5928	0.1414	672.6

or by changing the design of the wedges (bigger size and larger apex angle).

$$\Delta\nu \cong \frac{1}{\Delta\tau_{max}}. \tag{2.41}$$

It has been successfully implemented as a FT spectrometer [29], [27], [28] due to its simplicity, compactness, stability, and delay precision. The stability comes from the fact that both replicas follow the same optical path which means that their relative delay is locked with high stability and no mechanical fluctuations affects the system. And the small apex angle of the wedges and the small group velocity mismatch introduced by them allow high delay accuracy. We used all these advantages of the TWINS in another application to obtain hyperespectral images in macro and microscope setups. The details of these implementations will be shown in the sections 3.1.3.1 and 3.1.3.2.

2.5 Fourier Transform Spectroscopy

The spectrum from an object provides very rich information about their identity, structure and its physical environment. Fourier transform (FT) spectroscopy is a powerful technique to measure spectra that unlike frequency domain spectrometers that use dispersive elements, it is based on interferometry. [30] Even though there are several types of FT spectrometers including those based on Michelson interferometers [31], Mach-Zehnder interferometers [32], Fabry-Perot interferometers [33], and birefringent interferometers [34], they share the same principle: there is an apparatus that is responsible for splitting an incent light into two components to obtain interference fringe pattern. The interferogram is nothing more than the correlation function of the electric field, and to obtain the spectrum from it we only have to calculate the FT. To understand that we need to analyze the interference pattern that is obtained by the detector. By measuring the overall incident energy($I(\tau)$) as a function of optical path difference of the interferometer, we obtain the delay dependent signal:

$$I(\tau) \propto \langle(\mathbf{E_1} + \mathbf{E_2})(\mathbf{E_1^*} + \mathbf{E_2^*})\rangle$$
$$I(\tau) \propto \langle|\mathbf{E_1}|^2\rangle + \langle|\mathbf{E_2}|^2\rangle + 2Re\langle\mathbf{E_1}\mathbf{E_2^*}\rangle,$$

where the symbols $\langle\rangle$ means time average, and $I_1 \propto \langle|\mathbf{E_1}|^2\rangle$, and $I_2 \propto \langle|\mathbf{E_2}|^2\rangle$. We are supposing that $\mathbf{E_1}$ and $\mathbf{E_2}$ are parallels (if not, the interference term needs to be multiplied by $cos(\phi)$, which ϕ is the angle between them). The first and second terms are the sum of the individual intensities of each incident light components, and the last one is the modulation, caused by the interference of the components. Since each component travels different distances, and they let the source at the same time ($t = 0$), thus they will be detected in a superposition of $E_1 = E(t)$ with $E_2 = E(t-\tau)$. By subtracting the DC offset (the mean amplitude of the interferogram), we are left with the oscillating AC term that provide information about the spectrum of $E(t)$: [27]

$$I_{AC}(\tau) = 2Re\langle E(t)E^*(t-\tau)\rangle. \tag{2.42}$$

By computing the Fourier transform (FT), we obtain that:

$$\mathscr{F}\{E(t)\} \equiv \tilde{E}(\omega),$$

$$\mathscr{F}\{E(t-\tau)\} = \tilde{E}(\omega)e^{-i\omega\tau},$$

$$\mathscr{F}^*\{E(t-\tau)\} = \tilde{E}^*(\omega)e^{+i\omega\tau},$$

and from Parseval's theorem, we have that:

$$\int_{t=-\infty}^{t=+\infty} f_1(t)f_2^*(t)dt = \frac{1}{2\pi}\int_{t=-\infty}^{t=+\infty} \tilde{F_1}(\omega)\tilde{F_2}^*(\omega)d\omega \tag{2.43}$$

In this way, we can see that the FT of the interferogram directly provides the spectrum of the incoming light: [29]

$$I_{AC}(\tau) = \int_{\mathbb{R}} E(t)E^*(t-\tau)dt = \frac{1}{2\pi}\int_{\mathbb{R}} \tilde{E}(\omega)\tilde{E}^*(\omega)e^{i\omega\tau}d\omega$$

$$I_{AC}(\tau) = \int_{\mathbb{R}} |\tilde{E}(\omega)|^2 e^{i\omega\tau}d\omega = \mathscr{F}^{-1}\{|\tilde{E}(\omega)|^2\} \tag{2.44}$$

$$\boxed{\mathrm{I_{AC}}(\tau) \underset{\mathscr{F}^{-1}}{\overset{\mathscr{F}}{\rightleftharpoons}} |\tilde{E}(\omega)|^2} \tag{2.45}$$

The visibility of the interferogram is defined as:

$$\eta = \frac{I_{max} - I_{min}}{I_{max} + I_{min}}. \tag{2.46}$$

The complex correlation function $\Gamma_{12}(\tau)$, which the $Re\Gamma_{12}(\tau)$ is the interference term in eq.2.42, is defined as: [11]

$$\Gamma_{12}(\tau) \equiv \langle E_1(t)E_2^*(t+\tau)\rangle, \tag{2.47}$$

before proceeding, it is useful to normalize the expression, to enable coherence to be specified independently of the moduli of the amplitudes:

$$\gamma_{12}(\tau) = \frac{\langle E_1(t)E_2^*(t-\tau)\rangle}{\sqrt{\langle E_1(t)E_1^*(t)\rangle\langle E_2(t)E_2^*(t)\rangle}} = \frac{\langle E_1(t)E_2^*(t-\tau)\rangle}{\sqrt{\Gamma_{11}(0)\Gamma_{22}(0)}} \tag{2.48}$$

We can write the oscillating AC term, showed in eq.2.42, in terms of the complex degree of partial coherence function $\gamma_{12}(\tau)$:

$$I_{AC}(\tau) = 2Re\langle E_1(t)E_2^*(t+\tau)\rangle,$$

$$I_{AC}(\tau) = 2\sqrt{I_1 I_2}Re\gamma_{12}(\tau), \tag{2.49}$$

which $\Gamma_{11}(0) = \langle E_1(t)E_1^*(t)\rangle \propto I_1$ and $\Gamma_{22}(0) = \langle E_2(t)E_2^*(t)\rangle \propto I_2$. The function $\gamma_{12}(\tau)$ is periodic function of τ. We can detect the interference fringe pattern in the detector if $|\gamma_{12}(\tau)|$ is non-zero: [12]

$$\begin{aligned} |\gamma_{12}(\tau)| &= 1 \quad && \text{Complete Coherence} \\ 0 < |\gamma_{12}(\tau)| &< 1 && \text{Partial Coherence} \\ |\gamma_{12}(\tau)| &= 0 && \text{Complete Incoherence} \end{aligned}$$

The irradiance is then varying between two limits, I_{max} and I_{min}:

$$I_{max} = I_1 + I_2 + 2\sqrt{I_1 I_2}|\gamma_{12}|, \tag{2.50}$$

$$I_{min} = I_1 + I_2 - 2\sqrt{I_1 I_2}|\gamma_{12}|, \tag{2.51}$$

thus, it follows that the visibility is:

$$\eta = \frac{2\sqrt{I_1 I_2}|\gamma_{12}|}{I_1 + I_2}. \tag{2.52}$$

In particular, if $I_1 = I_2$, then:

$$\eta = |\gamma_{12}|, \tag{2.53}$$

that is, the fringe visibility shows us the degree of the light coherence. [12]

3 Methods and Materials

3.1 Methods

3.1.1 Pump-probe Spectroscopy

Ultrafast transient absorption spectroscopy is a powerfull tool to study dynamical processes in molecules. In a typical pump-probe experiment, the system is photoexcited by an intense pump pulse, after that a second pulse, called probe, is placed to interact with the sample and its transmission changes are detected. We control the time delay (τ) between pump and probe, and for each delay τ the differential transmission($\Delta T/T(\lambda_{probe}, \tau)$) is measured [35], as indicated in Fig.10

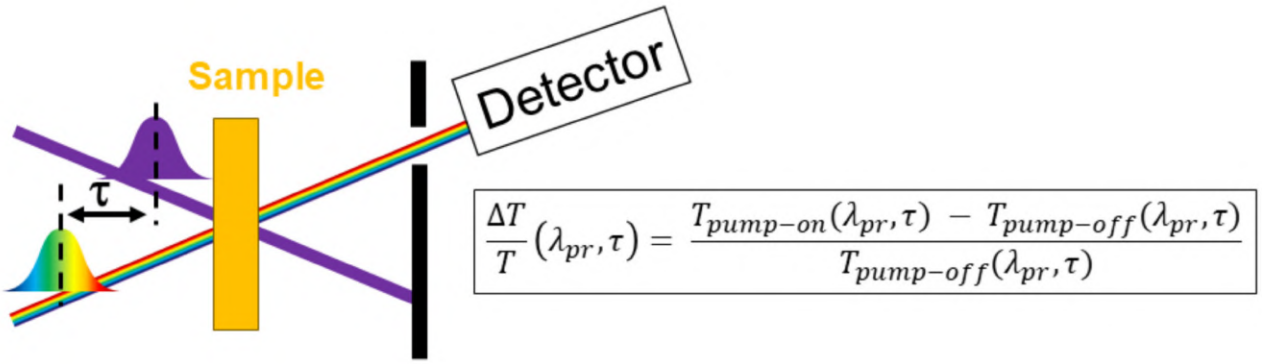


Figure 10 – Schematic configuration for pump-probe measurements; the transmission changes in the probe pulse due to the excitation with a pump pulse are detected for different time delays between the pump and probe pulses.

After measuring $\Delta T/T$, we calculated the transient absorption spectra. Since the transmittance (T) of the system is defined by the ratio of transmitted radiant energy (I) and the incident radiant energy (I_0), and the absorption (A) (or absorbance) is defined as:

$$\begin{aligned} A &= -\log_{10}(T) \\ &= -\log_{10}\left(\frac{I}{I_0}\right), \end{aligned} \tag{3.1}$$

so the transient absorption is obtained by the following calculations:

$$\frac{\Delta T}{T}(\lambda_{probe}, \tau) = \frac{T_{pump-on} - T_{pump-off}}{T_{pump-off}}$$

$$\frac{\Delta T}{T}(\lambda_{probe}, \tau) + 1 = \frac{T_{pump-on}}{T_{pump-off}}$$

$$\Delta A = -\log_{10}\left(\frac{T_{pump-on}}{T_{pump-off}}\right) = -\log_{10}\left(\frac{\Delta T}{T} + 1\right) \tag{3.2}$$

Three different transient absorption signals (ΔA) can be detected according to the probe wavelength: ground state bleaching (GSB), stimulated emission (SE), and photoinduced absorption (PA), as seen in Fig.11. If the pump pulses are resonant with an eletronic transition of the sample ($\hbar\omega_{pump} = E_1 - E_0$) when the probe pulses arrive on the sample after the pump, the number of absorbing molecules in the ground state is smaller than when the probe pulses arrive before. Hence for probe wavelengths shorter or equal to this excitation the differential absorption is negative ($\Delta A < 0$), giving rise to the photobleaching signal. For probe wavelengths greater than this excitation transition($\lambda_{probe} > \lambda_{pump}$) and after the interaction with the pump pulses, the probe photons can stimulate the system to emit back to the ground state which will increase the transmission of the probe ($\Delta A < 0$) giving rise to the stimulated emission signal. Finally, the excited state that was populated by the pump pulse can absorb to some other higher excited states which will decrease the transmission of the probe ($\Delta A > 0$) giving rise to the photoinduced absorption signal. [35] [36] The last signal can occur at any probe wavelength, it only depends on the electronic structure of the system; in particular we will see that the PA signals of tryptophan, tyrosine and phenylalanine spectrally overlap the SE signals and surpassed them. Because of that the PA is the dominant signal in the amino acids transient absorption spectra.

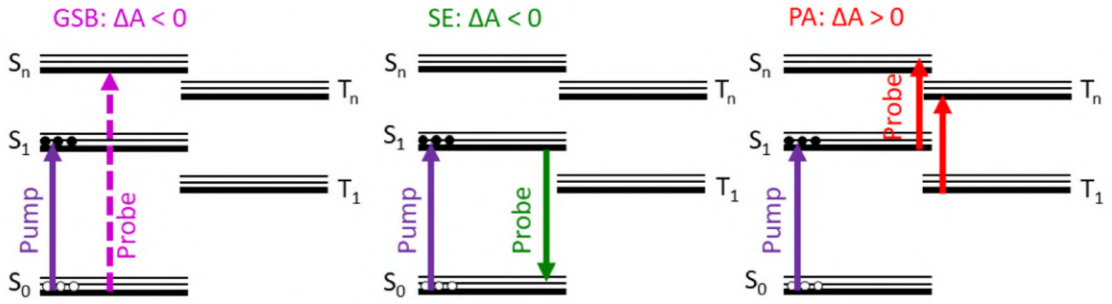


Figure 11 – The main signals that can be detected in a pump-probe experiment: ground state bleaching, stimulated emission, and photoinduced absorption.

In the next section 3.1.1.1, we present the setup configuration we used to study the photoinduced processes in the aromatic amino acids by pump-probe spectroscopy.

3.1.1.1 Third-Harmonic Experimental Setup

We used a pump-probe system with a third-harmonic setup for the generation of the UV pump pulses at 266 nm, as we can see in Fig.12. The system starts with an

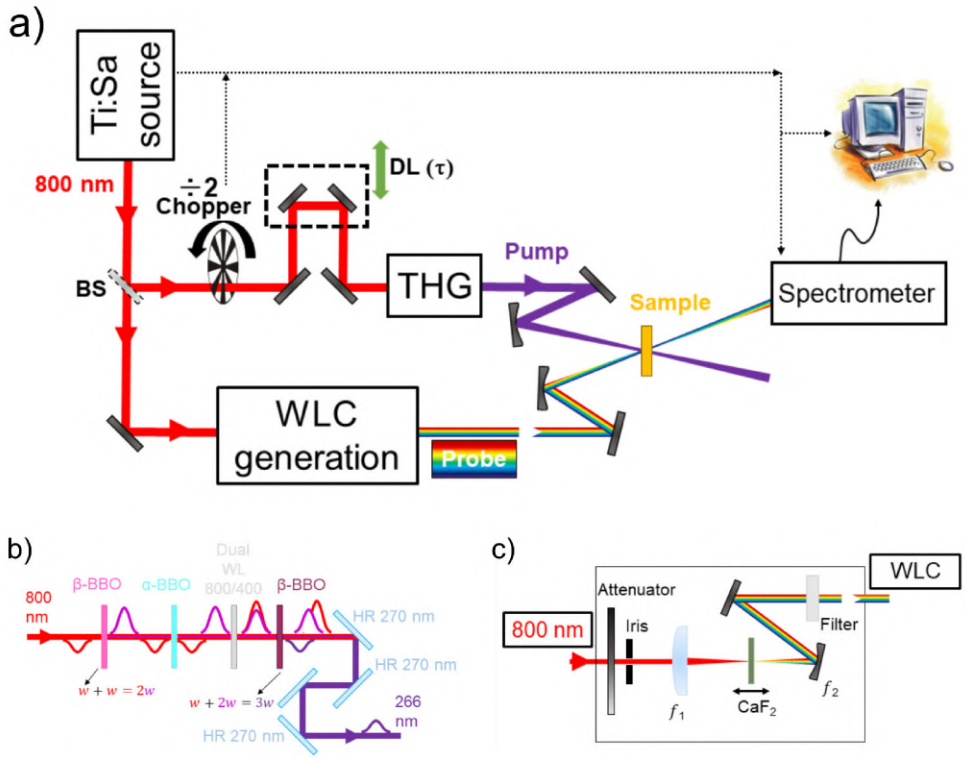


Figure 12 – Scheme of the noncollinear pump-probe setup: (a)the generation of few-optical-cycle UV pump pulses and visible probe pulses, based on: (b)THG of the Ti:sapphire laser (800 nm) and (c)WLC generation driven by the FW of Ti:sapphire laser (800 nm) in a CaF_2 crystal.

amplified Ti:sapphire laser (Libra, Coherent, Santa Clara, CA, USA) which has vertically polarized pulses with 100 fs width, 1 kHz repetition rate at 800 nm wavelength. The beam is divided in two by the beamsplitter(BS), one beam is used to generate the third-harmonic pulses from the fundamental wavelength (FW) and the other is responsible for generating broadband probe pulses obtained by white light continuum (WLC) generation in a CaF_2 crystal. The third-harmonic generation (THG) produces 266 nm pulses as illustrated in Fig.12b). The first crystal is a β-BBO, type I, with 500 μm thick, cut at $\theta = 22.5°$ which produces vertically polarized pulses at 400 nm (the FW has horizontal polarization in the entrance of the TH setup); this is the second-harmonic generation (SHG) process. Then we use an α-BBO crystal to compensate the time delay between the FW pulses and the SH pulses due to the group velocity mismatch (GVM) in the crystal. This is used to improve the overlap of the pulses for the subsequent THG process. Then we use a dual wavelength waveplate to rotate the FW polarization by 90° and overlap it with the SH pulse. Finally, we have a β-BBO, type I, cut at $\theta = 29.2°$ which is responsible for

generating the third-harmonic pulses. We also used 4 dielectric mirrors with high reflection for TH wavelength, thus blocking the FW and SH pulses.

The WLC can be obtained from the FW or from the SH of Ti:sapphire, depending on the spectral window that needs to be covered. A 2 mm thick sapphire crystal is used to cover the $400-710$ nm range and a 3 mm thick CaF_2 crystal is used to cover the $330-650$ nm range using the FW of the laser, the last crystal is also used to cover the UV range, $270-370$ nm, driven by the SH of the laser. We control the stability of the process using an iris and a variable attenuator which are used to vary the numerical aperture and the power of the beam, and a precise translation stage which is used to control the position of the nonlinear crystal in the focus. [37] For our measurements, we used a CaF_2 crystal and the 800 nm laser source which was focused by a lens of 75 mm focal length, and the WLC was recollimated by a spherical mirror of 50 mm focal length.

The pump and the probe pulses were focused noncollinearly onto the sample at approximately 5° by a CaF_2 lens of 300 mm focal length for the pump pulses and by a spherical mirror of 250 mm focal length for the probe pulses. The pump spot size at the focus position was around 120 μm and its intensity was 0.88 mJ/cm^2; the probe spot size was around 56 μm. We measured the differential transmission ($\Delta T/T$) for each time delay (τ) between pump-probe by dispersing the probe spectrum on an optical multichannel analyzer (OMA), modulating the pump beam and subtracting pump-on and pump-off probe spectra. The system enabled the acquisition of full 2D pump-probe maps with 120 fs temporal resolution and sensitivity down to 10^{-4}.

3.1.2 Theoretical Calculations

The calculations were performed by the Theoretical and Computational Photochemistry group from the University of Bologna coordinated by Prof. Marco Garavelli. They performed quantum mechanics/molecular mechanics (QM/MM) calculations using the COBRAMM software to characterize and analyze our time-resolved amino acids measurements. They implemented a new version of the simulation software COBRAMM where is possible to setup and analyze pure QM and QM/MM calculations for the ground and excited states [38]. To explain the photoinduced absorption and stimulated emission signals of tryptophan in neutral pH, they performed calculations using this new implemented COBRAMM program, interfacing the MOLCAS QM code with the AMBER force field, taking into account the solvent. Møller-Plesset second-order perturbation theory (MP2) level was used to optimize the ground state geometry minimum. The excited states geometry optimizations were computed at the MS-CASPT2 level using an active space including all the valence π-orbitals. Photoinduced absorption energies and oscillator strengths were calculated at MS-CASPT2 level, state averaged on 30 singlet or triplet states. The absorption spectrum simulation (linear absorption (LA)) was calculated at CASPT2 level. The LA spectrum

showed in Fig.28 is the combination of the single LA spectrum calculated on six possible conformers of tryptophan. The weight of the single spectrum on the total one is proportional to its respective population on the ground state (GS), evaluated by long GS molecular dynamics in water.

3.1.3 Hyperspectral Imaging

Hyperspectral Imaging (HSI) combines spectroscopy and imaging in a single system. In this way the images obtained with this technique carry spatial and spectral information at each point of the image.

In recent years, more sophisticated and versatile hyperspectral systems have been developed to obtain high quality images in a limited amount of time to cover the most diverse applications. [39] There are different types of HSI systems, but they all get the same final datacube structure - a three dimensional image with two spatial and one spectral dataset, as we can see in Fig.13. The HSI systems are mainly composed by a light source,

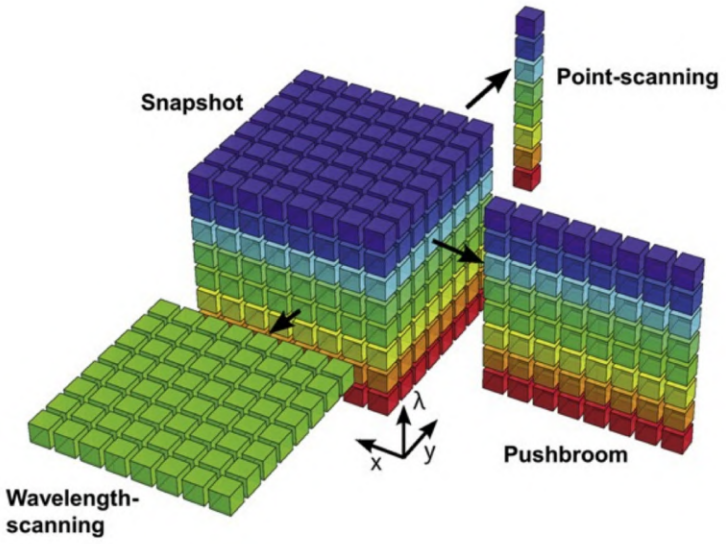


Figure 13 – Schematic drawing of a hyperspectral datacube with different acquisition modes. The axes x and y are the spatial coordinates and the axis λ has the spectral information. The figure was extracted from the reference [39].

a spectral device, and a detector. Because there are so many ways to obtain the hypercube, there are many types of hyperspectral systems. The device we developed at Politecnico di Milano which is capable to generate hyperspectral images, is a Fourier transform imaging spectrometer. In the applied method there are no filters or dipersive elements, and the spectrum is measured by using the interference of light. Our system is equipped with the TWINS, the birefringent interferometer that we presented in the section 2.4, which demonstrated exceptional stability and reliability to generates the interferogram. It creates two replicas of the input light radiation, $E(t)$ and $E(t-\tau)$, where τ is their relative delay.

A single detector record the interference of these replicas as a function of τ, giving rise to an interferogram. Therefore the interferogram is Fourier transformed in order to determine the spectrum at each position of the image.

We present two setup configurations that allow macroscopic and microscopic imaging. A camera for macroscopic imaging [40], and a microscope device [41], that will be described in the following sections.

3.1.3.1 Hyperspectral Camera

The hyperspectral camera was the first configuration of the hyperspectral imaging that we implemented [40]. A general scheme of our device is shown in Fig.14. It consists of a TWINS interferometer (see the details in section2.4) followed by a monochrome imaging system. The TWINS is composed of two birefringent blocks A and B, and two polarizers

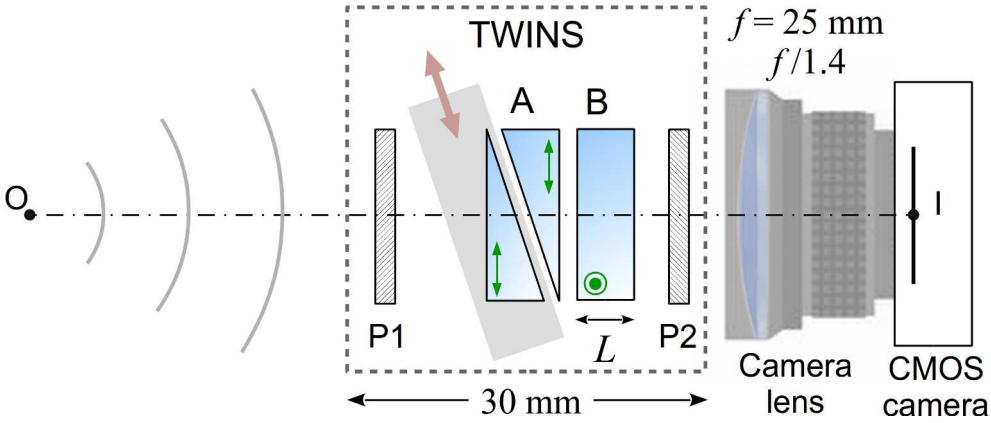


Figure 14 – Schematic setup of the hyperspectral camera: P1, P2 are wire-grid polarizers; A block: α-BBO wedges, with optical axis along x direction (green double arrow); B block: α-BBO plate, with optical axis along y direction (green circle). The brown double arrow indicates the wedge translation direction. O: object and I: image. This image was extracted from the ref. [40].

P1 and P2. The device as already said, acts as a common path interferometer based on birefringence. The camera lens has focal length $f = 25$ mm and maximum aperture $f/1.4$. The image detector is a monochrome CMOS silicon detector with size 6.78 mm×5.43 mm, 1280 × 1024 pixels, with 10 bits depth and spectral sensitivity from 400 nm to 1100 nm. The angular field of view of the combined camera lens and detector is 15.4° (19° along the sensor diagonal).

The TWINS device is responsible to generate two replicas of the optical field coming from the object. The design allows varying the thickness of the block A generate a total phase delay going from negative to positive that depends on the refractive index difference of the crystal (α-BBO) and on the thickness of block A. Then, the polarizer P2 projects the two orthogonal polarizations to a common polarization state, making them interfere. We obtained our hypercube by taking a sequence of images as a function of the block A

wedge position that was controlled by a motorized translation stage ($L-402.10SD$, Physik Instrumente) with maximum travel range of 13 mm. In this way the phase delay between the two replicas is scanned from negative to positive values and the interferograms that form in each pixel of the sensor are recorded by the camera. Finally, we calculated the Fourier transform of the dataset to produce the spectrally resolved images, the hypercube.

Because the spectral resolution is inversely proportional to the travel range of the wedge, only limited by the lateral size of the available wedge (10 mm), thus the maximum spectral resolution achievable for our device at 635 nm is 3 THz ($\approx$ 4 nm), scanning the wedges position for $\pm$5 mm. The time required to acquire the images depends on the intensity of the light from the sample. For instance, as will be shown in the results, in the test with laser sources the acquiring time was around one minute, but with the fluorescence sample it took about five minutes.

An interferometer is suitable for imaging when it is able to maintain coherence (i.e. similar path delay) between the rays of light that form the interferogram at a given image point. In order to estimate the fringe visibility for our hyperspectral camera, we will consider monochromatic waves with angular frequency ω, for a generic ray propagation direction through the system. In Fig.15a) we are representing the two blocks A and B of the TWINS interferometer with crossed optical axes, and with the air spacing between them neglected for simplicity. When a ray impinges the system with an angle α with respect to the normal direction we obtain two polarized replicas, the vertically (red) and horizontally (blue), of the input ray that accumulates a relative phase shift φ. Assuming

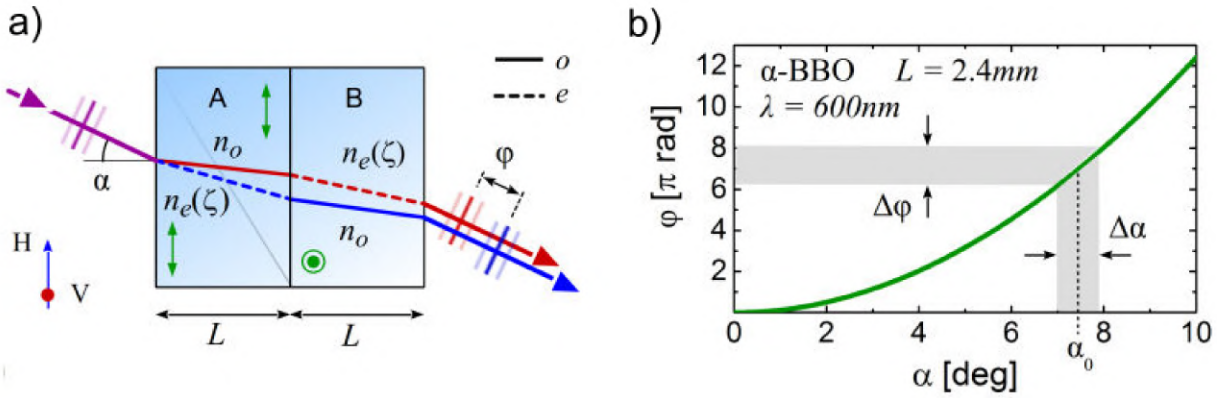


Figure 15 – a) Top view of the optical paths and refractive indexes of the vertically-polarized (V, red) and horizontally-polarized (H, blue) components of a ray traveling in the TWINS system; dashed lines: extraordinary (e) rays; solid lines: ordinary (o) rays. b) Relative phase accumulated by the crosspolarized components as a function of α. This figure was extracted from the ref. [40].

that the ray can be described as a plane harmonic wave of the form $e^{i(kr-\omega t)}$, then this

relative phase shift (φ) will be:

$$\varphi = [(k_{e2}d_{e2} + k_{o3}d_{o3}) - (k_{o2}d_{o2} + k_{e3}d_{e3})] + k_0\delta, \tag{3.3}$$

$$\varphi = [(\frac{2\pi n_{e2}(\zeta)}{\lambda_0}d_{e2} + \frac{2\pi n_{o3}}{\lambda_0}d_{o3}) - (\frac{2\pi n_{o2}}{\lambda_0}d_{o2} + \frac{2\pi n_{e3}(\zeta)}{\lambda_0}d_{e3})] + \frac{2\pi}{\lambda_0}\delta,, \tag{3.4}$$

in which $(k_{e2}d_{e2}+k_{o3}d_{o3})$ is the phase accumulated by the blue ray, the term $(k_{o2}d_{o2}+k_{e3}d_{e3})$ is the phase accumulated by the red ray, both showed in the Fig.15a), and $k_0\delta$ is the phase difference accumulated between the polarized components outside of the plates. Notice that the refractive index $n_e(\zeta)$ depends on the angle between the optical axes and the propagating direction of the ray, and will assume values from n_e to n_o, as we showed before in sec.2.4, equation2.39. The Fig.16 illustrates the phase the rays accumulate outside the α-BBO plate. The δ can be expressed as:

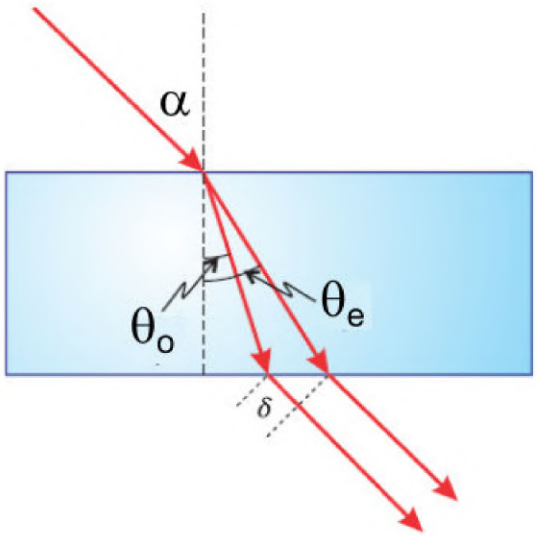


Figure 16 – Phase difference accumulated by the two polarization components of a ray that passes through a birefringent crystal. This figure was adapted from the ref. [42].

$$\delta = L[tan(\theta_{e2}) - tan(\theta_{e3})]sin(\alpha). \tag{3.5}$$

These angles will be clear in the following equations.

The dashed lines in the crystal, showed in Fig.15, represent the extraordinary rays (e-rays) and the solid lines represent the ordinary rays (o-rays). Due to birefringence the ordinary beams experience the same ordinary index n_o in blocks A and B but the extraordinary beams experience $n_{e2}(\zeta)$ in block A and $n_{e3}(\zeta)$ in block B. Following both rays in the crystal we can see two paths, $(d_{e2} + d_{o3})$ followed by the blue ray and $(d_{o2} + d_{e3})$

followed by the red ray:

$$
\begin{aligned}
n_{air}sin(\alpha) &= n_{o2}sin(\theta_{o2}) && \text{o-ray on the first interface}\\
sin(\theta_{o2}) &= \frac{sin(\alpha)}{n_o}\\
\theta_{o2} &= sin^{-1}\left[\frac{sin(\alpha)}{n_o}\right]\\
n_{air}sin(\alpha) &= n_{e2}(\zeta)sin(\theta_{e2}) && \text{e-ray on the first interface}\\
sin(\theta_{e2}) &= \frac{sin(\alpha)}{n_e(\frac{\pi}{2}-\theta_{e2})}\\
\theta_{e2} &= sin^{-1}\left[\frac{sin(\alpha)}{n_e(\frac{\pi}{2}-\theta_{e2}))}\right]\\
n_{o2}sin(\theta_{o2}) &= n_{e3}(\zeta)sin(\theta_{e3}) && \text{o-ray on the second interface}\\
sin(\alpha) &= n_e(\pi/2)sin(\theta_{e3})\\
\theta_{e3} &= sin^{-1}\left[\frac{sin(\alpha)}{n_e(\pi/2)}\right]\\
n_{e2}(\zeta)sin(\theta_{e2}) &= n_{o3}sin(\theta_{o3}) && \text{e-ray on the second interface}\\
sin(\alpha) &= n_o sin(\theta_{o3})\\
\theta_{o3} &= sin^{-1}\left[\frac{sin(\alpha)}{n_o}\right]
\end{aligned}
$$

$$
\begin{aligned}
(d_{e2}+d_{o3}) &= \frac{L}{cos(\theta_{e2})}+\frac{L}{cos(\theta_{o3})}\\
(d_{o2}+d_{e3}) &= \frac{L}{cos(\theta_{o2})}+\frac{L}{cos(\theta_{e3})}\\
(d_{e2}+d_{o3})-(d_{o2}+d_{e3}) &= L\left(\frac{1}{cos(\theta_{e2})}-\frac{1}{cos(\theta_{e3})}\right)
\end{aligned}
$$

$$
(d_{e2}+d_{o3})-(d_{o2}+d_{e3}) = L\left(\frac{n_e(\frac{\pi}{2}-\theta_{e2})}{\sqrt{n_e^2(\frac{\pi}{2}-\theta_{e2})-sin^2(\alpha)}}-\frac{n_e(\pi/2)}{\sqrt{n_e^2(\pi/2)-sin^2(\alpha)}}\right). \quad (3.6)
$$

Thus, the phase difference accumulated by the two components inside the crystal can be expressed as:

$$
\varphi_{crystal} = \frac{2\pi L}{\lambda_0}\left(\frac{n_e^2(\frac{\pi}{2}-\theta_{e2})}{\sqrt{n_e^2(\frac{\pi}{2}-\theta_{e2})-sin^2(\alpha)}}-\frac{n_e^2(\pi/2)}{\sqrt{n_e^2(\pi/2)-sin^2(\alpha)}}\right), \quad (3.7)
$$

in which

$$
n_e(\zeta) = \frac{n_o n_e}{\sqrt{n_o^2 sin^2(\zeta)+n_e^2 cos^2(\zeta)}}. \quad (3.8)
$$

This implies that:

$$
n_e(\pi/2) = n_e, \quad (3.9)
$$

$$n_e(\frac{\pi}{2} - \theta_{e2}) = \sqrt{\frac{n_o^2 n_e^2 + (n_o^2 - n_e^2)sin^2(\alpha)}{n_o^2}} \tag{3.10}$$

Finally, the total phase accumalated can be expressed as:

$$\varphi = \frac{2\pi L}{\lambda_0}\left(\frac{n_e^2(\frac{\pi}{2} - \theta_{e2})}{\sqrt{n_e^2(\frac{\pi}{2} - \theta_{e2}) - sin^2(\alpha)}} - \frac{n_e^2}{\sqrt{n_e^2 - sin^2(\alpha)}}\right) + \frac{2\pi L}{\lambda_0}[tan(\theta_{e2}) - tan(\theta_{e3})]sin(\alpha) \tag{3.11}$$

The graph in Fig.15b) plots φ as a function of α, for the time delay (τ) between the replicas set to zero, i.e. when the plates have the same thickness $L = 2.4$ mm, for a wave at $\lambda_0 = 600$ nm through the $\alpha-$BBO blocks.

We can see that α strongly affects φ, and we now will discuss how this may influence the visibility. From each point of the scene emerges bundle of rays that pass through the interferometer and the imaging optics, and finally impinge the pixel I at the image plane. In Fig.17a) we illustrated the peripheral rays of the bundle that travels from O to I. They impinge on the birefringent interferometer at angles α_1 and α_2, and consequently all the rays of the bundle have incident angles ranging from α_1 to α_2. The average angle

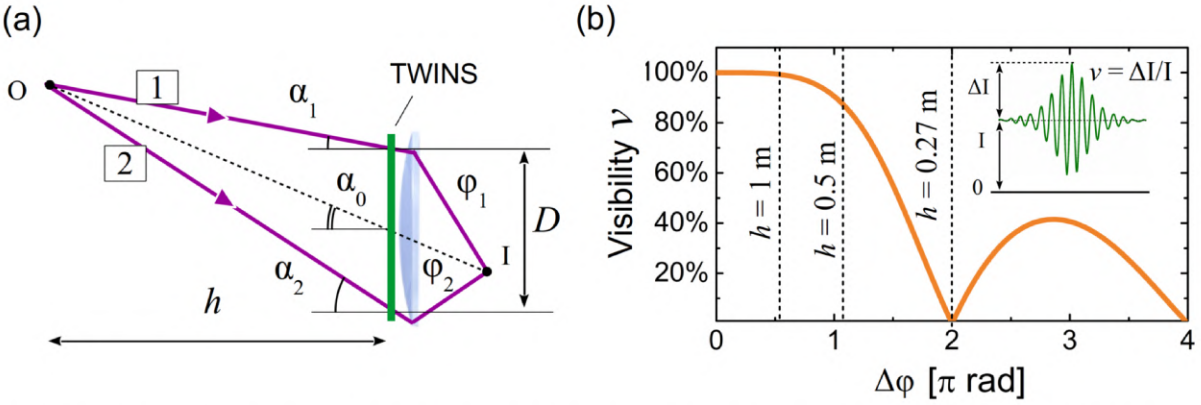


Figure 17 – a)Diagram of two marginal rays (1 and 2) propagating from the source point O to the image point I; φ_1, φ_2: relative phase between the vertically and horizontally polarized components of the field replicas. b)Visibility of the interferogram of a CW wave, as a function of the phase spread $\Delta\varphi$. Vertical lines correspond to various distances h of an object at the edge of the field of view of our camera. Inset: definition of η. This figure was extracted from the ref. [40].

is $\alpha_0 = (\alpha_1 + \alpha_2)/2$, and to the first order the angular spread $\Delta\alpha = |\alpha_1 - \alpha_2|$ can be expressed as:

$$\Delta\alpha \approx tan^{-1}\left[\frac{D/h}{1/tan^2(\alpha_0)}\right] < tan^{-1}(D/h), \tag{3.12}$$

and this implies that the corresponding phase shift φ ranges from $\varphi_1 = \varphi(\alpha_1)$ to $\varphi_2 = \varphi(\alpha_2)$.

To design a camera with large visibility for all pixels in the detector, we need to focus on the most unfavorable condition, the rays from the point O with the largest

phase range $\Delta\varphi$. As showed in Fig.17a), they are at the edge of the field of view. The birefringent interferometer generates for each of the rays, two phase delayed replicas ($E_j(\varphi_j)$) at frequency ω. The overlap of all rays at the image point I in the neighbourhood of phase delayed equal to zero ($\psi_\tau = 0$ means birefringent blocks A and B with same thickness), after the projection on a common polarization with a polarizer at 45°gives the field:

$$E_T(\psi_\tau) = \int_{\varphi_1}^{\varphi_2} E_j d\varphi = E_0 \int_{\varphi_1}^{\varphi_2} [cos(\omega t) + cos(\omega t - \psi_\tau - \varphi)] d\varphi. \tag{3.13}$$

The measured intensity(the interferogram) is proportional to $I \propto \langle |E_T(\psi_\tau)|^2 \rangle$. Assuming that all rays have the same amplitude E_0 and their phase linearly ranges varies from φ_1 to φ_2 thus, the overlap of all rays at the image point I coming from O gives origin an interferogram which visibility depends on the phase spread $\Delta\varphi = \varphi_2 - \varphi_1$. We derive from eq.3.13 that the visibility depends uniquely on the phase spread and its behavior is plotted in Fig.17b). [43] Note that if all rays had the same phase shift φ_i, the visibility would be equal to 1.

In the case of our camera, for an object placed at the edge of the field of view ($\alpha_0 = 7.7°$) and at a distance $h = 0.5$ m, the fringe visibility is about 0.85. We can conclude that with this large visibility our TWINS hyperspectral camera is able to provide high contrast interferogram at all pixels of the image, suitable for FT hyperspectral application.

3.1.3.2 Hyperspectral Microscope

The development of the hyperspectral imaging microscope started at Politecnico di Milano [41] and after that we also implemented the setup at the Biophotonics Laboratory in the Physics Department of the Federal University of Minas Gerais (UFMG). The description of the setup, and also the results that will be presented in section 5.2, are the ones that we obtained in the Biophotonics Laboratory.

The hyperspectral imaging microscope setup that we implemented is shown in Fig.18. The microscope is composed by an infinite-corrected objective, located before the birefringent interferometer (TWINS), a tube lens and a monochrome CCD camera with a lens. We choose this configuration because as showed in Fig.18b) all the rays coming from the same point of the object enter in the TWINS device parallelly, this means that theoretically they all propagate at the same angle ($\Delta\alpha = 0$). In other words, all the rays from the same object point experience a common phase shift φ ($\Delta\varphi = 0$), hence the visibility of the interferogram is maximum.

The other possibility is to place the TWINS device between the tube lens and the detector. The comparison between these configurations and their specific advantages, were discussed in the ref. [41].

One application of the hyperspectral microscopy is for fluorescence measurements in

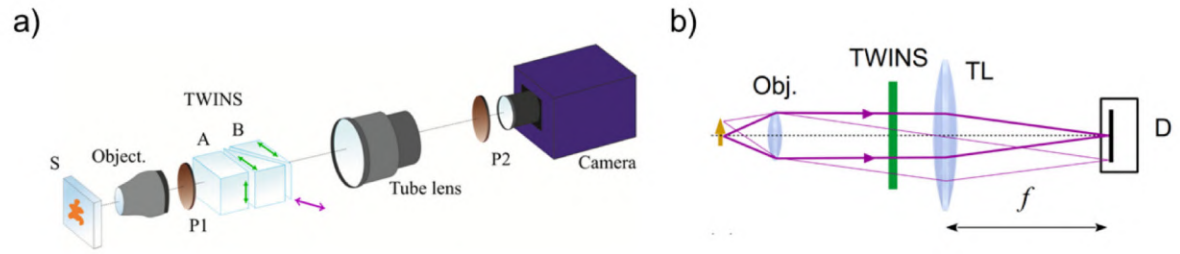


Figure 18 – Schematic setup of the hyperspectral imaging microscope; a)P1 and P2: wire grid polarizers at angle of +/- 45° with respect to the optical axes of A and B; A (plate) and B (wedges): α-BBO birefringent blocks; Obj: 40X objective with NA = 0.6; Tube lens: Nikon zoom lens with adjustable focal length; Camera: monochrome CCD with 12 bits and sensitivity in the $290 - 1000$ nm range with a Nikon camera lens. b)Optical configuration of the hyperspectral microscope. The optical configuration showed in b) was extrated from the ref. [41].

biological tissues. For this, we tested different ways to detect the fluorescence spectra. The best way is to measure in back-reflection by using a dichroic mirror since in transmission is not possible to remove completely the laser excitation. In Fig.19 we show the schematic setup we used to measure the fluorescence and the autofluorescence of the samples presented in section 5.2. This configuration enabled a uniform excitation throughout the measured region of the samples.

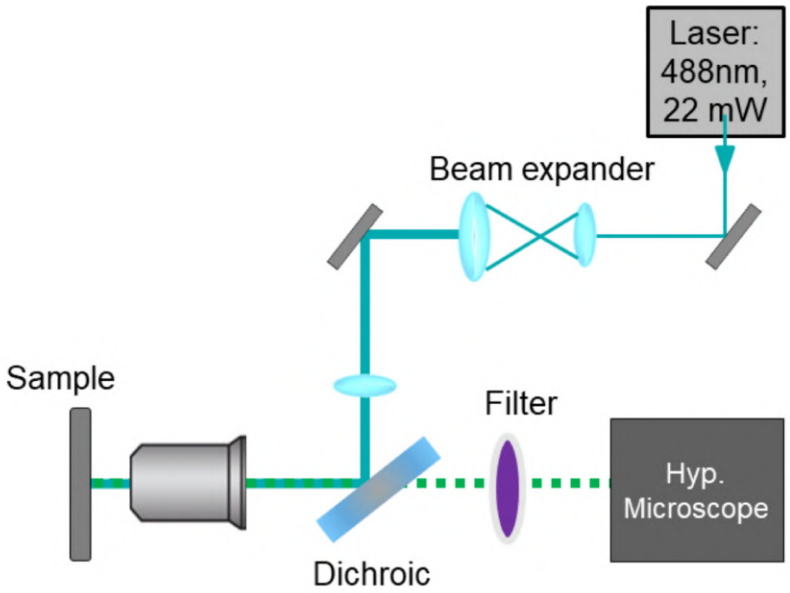


Figure 19 – Schematic configuration for a uniform excitation of the samples in the hyperspectral microscope: we excited the samples at 488 nm, and used a dichroic mirror at 505 nm and an edge filter at 488 nm to remove the excitation laser from the emisson of the sample. The beam expander is responsible to increase the spot size of the laser. The lens just before the dichroic mirror is placed in a distance from the infinite-corrected objetive in a way that all rays coming out of the objective are parallel.

3.2 Materials

In this section we present the materials studied with the time resolved pump and probe spectroscopy and the last material is the one we studied in the hyperspectral microscope. Most of the samples used for the hyperspectral imaging will be presented together with the results for each setup configuration.

3.2.1 Amino Acids[1]

Proteins are complex structures formed by a sequence of amino acids with their synthesis controlled by genetic mechanisms, which involves DNA replication and RNA transcription. All of them are built from a set of twenty amino acids, covalently bond in their characteristic linear sequences. Although they have the same subunits the cells can produce proteins with surprisingly different properties and activities. Each protein has a specific multidimensional configuration, which is stated by the amino acids sequence, and by the degree of inclination between the chemical bonds. The final 3D configuration of a protein will define its biological function and because it is a very complex structure, many studies have been carried out on its subunits - the amino acids. We focus our studies in three of them: tryptophan, tyrosine, and phenylalanine.

The α-amino acids which are present in peptides and proteins have a standard structure: a carboxyl group, an amino group and the "R" group bonded to the same carbon atom(the α carbon):

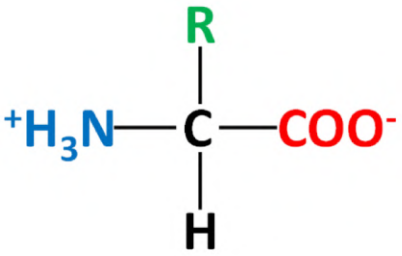
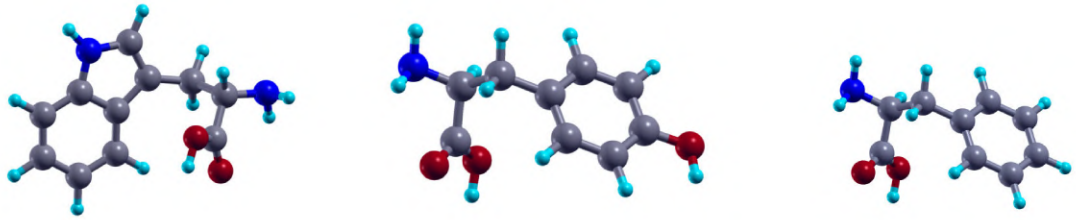


Figure 20 – The general structure of an α-amino acid with a carboxyl group, amino group, and R group bonded to α carbon (zwitterion form)

.

The R group is different in each amino acid and presents different chemical properties, for example, the ones present in our study have R aromatic groups as illustrated in Fig.21. One of the most explored properties of the aromatic amino acids is their strong absorption of light in the ultraviolet (UV) range. Tryptophan, tyrosine, and phenylalanine absorb light at characteristic wavelengths and because of that it is possible to detect and

[1] The section 3.2.1 was adapted from the references [44] and [45]



(a) Tryptophan (b) Tyrosine (c) Phenylalanine

Figure 21 – Aromatic amino acids molecular structure which the carbon atoms are shown in gray, the oxigen atoms in red, the nitrogen atoms in blue, and the hidrogen atoms in cyan.

identify these molecules inside a peptide or a protein, and thereby infer some information about the structure of that compound.

The α-amino acids have another distinctive feature, they are amphoteric, meaning that they can act either as an acid (proton donor) or a base (proton acceptor). In this way their structure in aqueous solution is pH dependent. In physiological conditions the zwitterion (dipolar ion) form predominates, and is formed from protonation of the amino group by the carboxylic acid. This characteristic pH in which the dipolar form is present predominantly is called isoelectric pH (pI). The titration curve for them presents two zones of stability (chemical equilibrium) where they act as a buffer in solution. The graph in Fig.22 shows this behavior for glycine. For tryptophan, tyrosine, and phenylalanine pI,

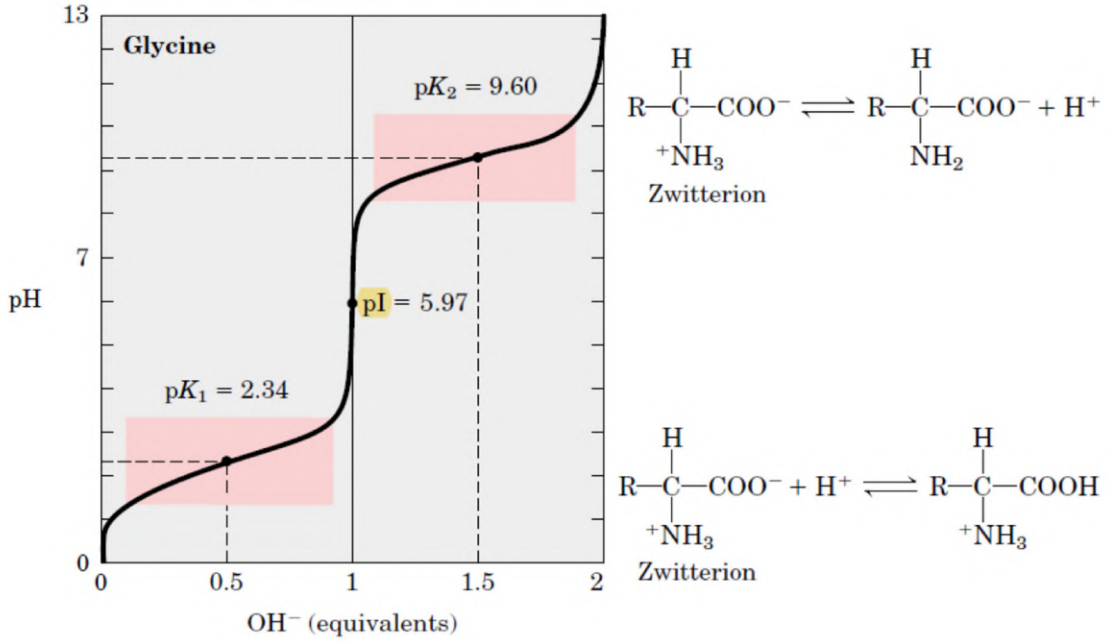


Figure 22 – Titration curve of 0.1 M glycine at 25°C; the shaded boxes indicate the regions in which glycine best acts as a buffer. Adapted from [44]

pK_1, and pK_2 values are shown in the table3 below. Tyrosine presents one more zone of buffering than the other amino acids , pK_r, with three stages corresponding to the three

possible ionization steps. The last one is the titration of the ionizable R group.

Table 3 – Acid-Base Properties of Aromatic Amino Acids

Amino Acid	pK_1	pK_2	pK_r	pI
Tryptophan	2.38	9.39	-	5.89
Tyrosine	2.20	9.11	10.07	5.66
Phenylalanine	1.83	9.13	-	5.48

The photophysics (excitation and deactivation processes, with and without light) and photochemistry (chemical reactions induced by light) of these three molecules are subject of this thesis. To address this problem we focused on experiments of transient absorption, photoluminescence, and *ab-initio* calculations that are showed in Chapter4.

3.2.2 Mice Liver Tissues Infected with *Schistosoma Mansoni*

The liver is composed mainly of epithelial cells called hepatocytes which when submitted to excitation in the UV-Visible range give rise to an autofluorescence emission. This autofluorescence emission in biological samples is related to the emission of endogenous fluorophores such as collagen and elastin, NAD(P)H, the aromatic amino acids, flavins, vitamin A, porphyrins and their derivatives, etc. [46] Anna Cleta Croce and *et al.* recorded autofluorescence spectra on hepatocytes and through the analysis of the curves, it was evaluated the relative contribution of each fluorophore involved in the overall emission. [47] It was shown that excitating the liver tissue homogenates from livers of male Wistar rats ($250 - 300$g; Harlan-Nossan, Correzzana, Italy), at 470 nm it is observed a main band centered at about 520 nm, corresponding to the emission of flavins, and two minor bands at about 625 and 670 nm, that may be related to the presence of porphyrins and Heme metabolism-related compounds. They also showed that excitating the samples at other wavelengths provides information about other fluorophores.

We expect that alterations in the liver functional conditions modify the physico-chemical state of the endogenous fluorophores, thus affecting the tissue autofluorescence properties. Therefore, autofluorescence analysis could be used in studies of liver tissues infected with *Schistosoma mansoni*. This project was carried out in collaboration with the Biophysics Department of Universidade Federal de Pernambuco (UFPE). The samples were prepared by the Dr. Gabriela Ayres Fragoso Nascimento and the discution of the results were done in collaboration with the Prof. Adriana Fontes. [48] The idea of the project was to study mice liver granulomatous lesion caused by infection of *Schistosoma mansoni* by using hyperspectral autofluorescence imaging.

We analyzed liver tissues of female mice that were individually infected by *Schistosoma mansoni* over different days of infection to study the evolution of the disease. Past 30 days of infection, a group of ten mice was euthanized by an overdose of anesthetic and their

livers, spleens and kidneys were removed with surgical scissors. The second and third group, also with 10 animals, were euthanized past 60 and 120 days of infection, under the same conditions of the first group. Ten other mice were used as control samples. The experimental protocols were in accordance with the requirements of the Animal Experiments Ethics Committee of the Federal University of Pernambuco, Brazil (n°23076.017619/2015-60). Finally the livers, spleens, and kidneys were washed several times with PBS (phosphate buffered saline) and preserved in 10% formalin in PBS for histopathological study. The selected fragments underwent dehydration steps (diving in ethanol) and diaphanization (diving in xylene), followed by a dip in molten paraffin at 60°C. Two paraffin sections of samples were sequentially cut with thickness of 8 μm each, and transferred to glass slides. [49]

Previous studies showed that granulomas induced by the parasite eggs are the primary lesions in mice livers infected with *Schistosoma mansoni*. [50] At later stages of infection, this initial lesion around the egg is subsequently encompassed by proliferating connective tissue. [51] The resulting fibrous capsule spreads centripetally, producing three-dimensional collagen fibers around the egg. Two patterns of fiber arrangement were observed: collagen type III containing reticular fibers and collagen type I containing collagen fibers. [52] In Fig.23b) we illustraded the granuloma structure of *Schistosoma mansoni* in histological section of mouse liver stained with hematoxylin and eosin, and analyzed by optical microscopy. The images showed in Fig.23 were obtained from the website of the Laboratory for the Study of Protein Structure and Function from the Universidade Federal de Juiz de Fora.

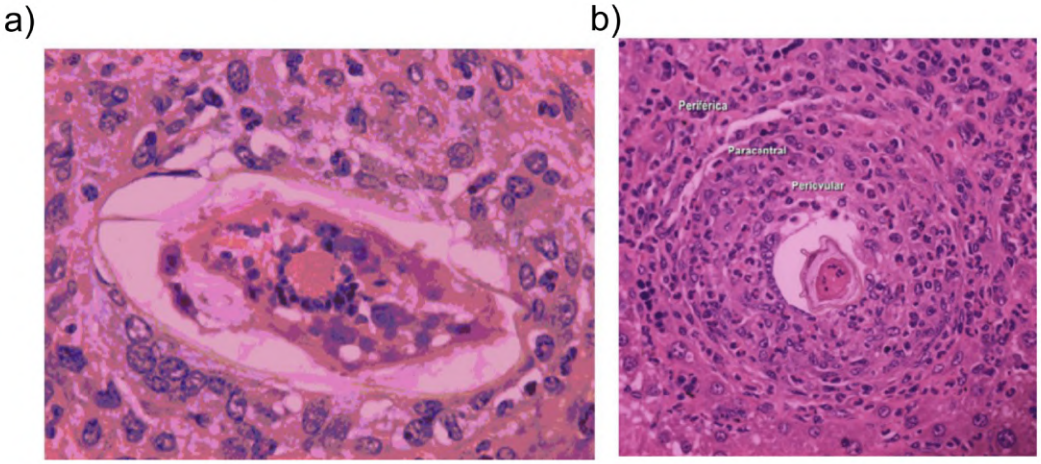


Figure 23 – Egg a) and granuloma structure b) of *Schistosoma mansoni* in histological section of Swiss mouse liver stained with hematoxylin and eosin and analyzed by optical microscopy. The figures were extrated from the ref. [53].

In this way, to characterize the evolution of the disease we excitated the liver tissue samples (without stain) at different stages of the infection, at 488 nm and obtained the hyperspectral autofluorescence images. The results can be seen in section 5.2.

4 Results - Amino Acids

4.1 Stead-State Absorption

We measured the steady-state absorption spectra of tryptophan, tyrosine, and phenylalanine in a 1 mm cuvette at room temperature using a V-570 spectrophotometer. We prepared the solutions in three different pH conditions, for the neutral we used a phosphate buffer saline (PBS) solution at pH 7.4, for the acid we used hydrochloric acid (HCl) aqueous solution at pH 1.0, an the third one was a buffer solution at pH 5.35 (generally used for cells). However, for the pH 5.35 solution the results show almost no difference when compared to the neutral condition, thus they are presented in Appendix A.1. We choose the solution concentrations in order to obtain an absorption of around 1 at the peak position in the absorbance spectrum, just to avoid the formation of aggregates. However, for tyrosine and phenylalanine we increased a little bit the concentration of

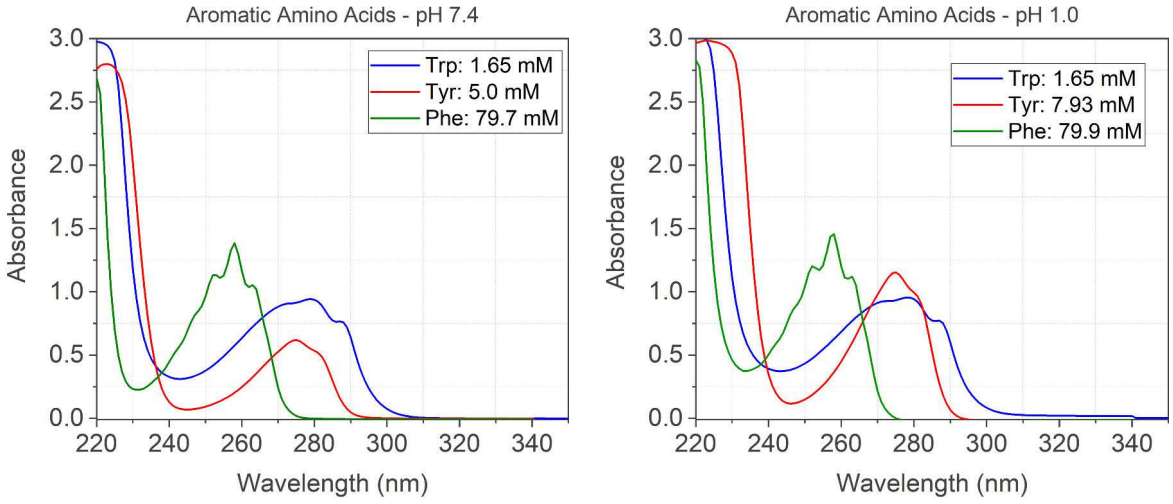


Figure 24 – Linear absorption spectra of tryptophan, tyrosine, and phenylalanine dissolved a) in phosphate buffer saline (pH 7.4) and b) in hydrochloric acid aqueous solution (pH 1.0)

the samples because the signal in the pump-probe measurements was really too noisy with absorption around 1 in the LA spectrum. As can be seen in the Fig.24 this was only possible for tyrosine in the acid medium since it showed low solubility in the saline buffer. These are the same samples that were used in the transient absorption measurements. We checked the LA spectrum before and after those measurements to make sure there was no sample degradation.

4.2 Photoluminescence

We measured the steady-state fluorescence spectra of tryptophan and phenylalanine in a 1 cm cuvette at room temperature using a Varian Cary 100 spectrophotometer, and the photoluminescence changing the excitation wavelength using a Varian Cary Eclipse spectrophotometer. These measurements were performed in the Chemistry Department at UFMG. We prepared the solutions in water since we did not have the phosphate buffer saline, and because we also believe that these are very similar experimental conditions. The results are shown in Fig.25.

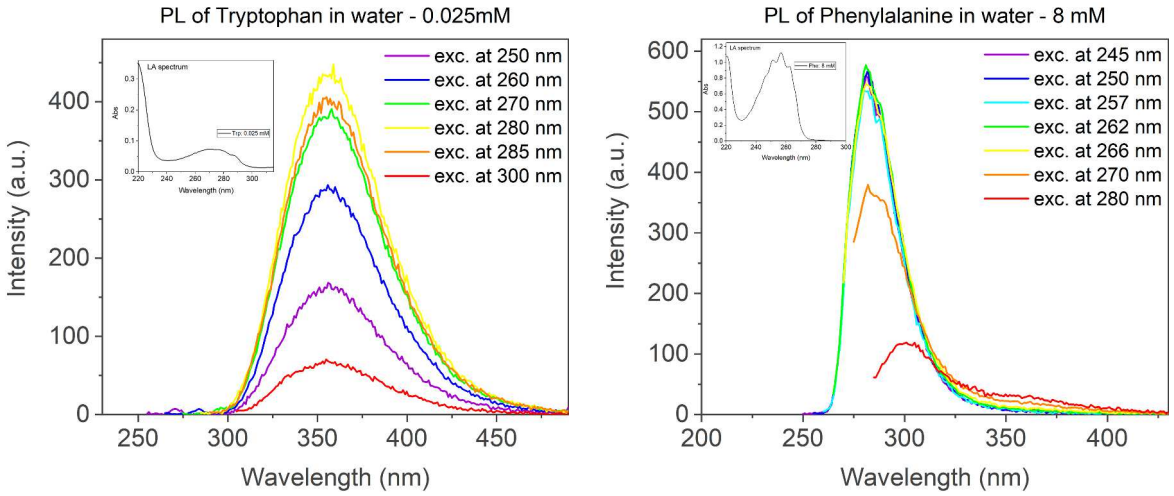


Figure 25 – Photoluminescence spectra of tryptophan and phenylalanine dissolved in water changing the excitation wavelength.

Although we did not measure the photoluminescence of tyrosine, in the literature we found steady-state fluorescence measurements and also time-resolved fluorescence of tyrosine in water. [54] [55] In Fig.26 we can see the fluorescence total spectra of tyrosine in water at pH 5.5 together with the decay associated spectra (DAS) that results from the time resolved fluorescence measurements. The emission spectra were recorded using a spectrofluorimeter (Perkin-Elmer, model LS-50B), and more details about the time resolved fluorescence measurements are described in ref. [54].

As shown in Figs.25 and 26, the steady-state fluorescence emission spectra of tryptophan, tyrosine, and phenylalanine in water show a single band with a maximum near 355, 303, and 284 nm respectively.

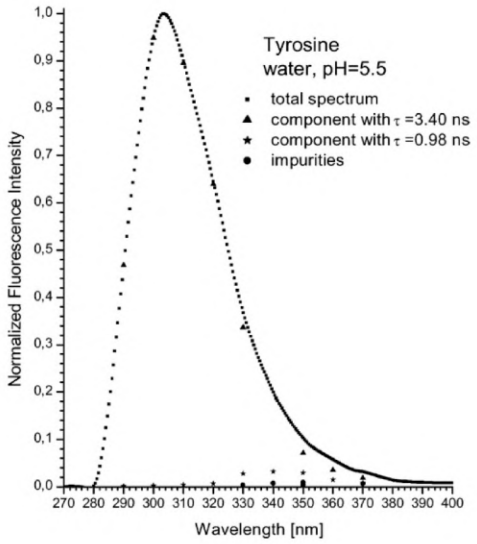


Figure 26 – Photoluminescence spectra from steady-state fluorescence and the decay associated spectra (DAS) from time resolved fluorescence of tyrosine in water at pH 5.5. For the steady-state fluorescence the excitation were done at 275 nm, and for time-resolved fluorescence at 277 nm. This figure was extracted from the paper [54].

4.3 Tryptophan

4.3.1 State of Art

Computational studies of the photophysics for the zwitterion tryptophan (expected to exist in aqueous solution from pH $4-8$) in $(H_2O)_2$ clusters showed the results of the lower vertical excitation energies and their respectively oscillator strengths and dipole moments. [56] Andrzej L. Sobolewski *et al.* in this paper assigned the first excited state as $L_b(\pi\pi^*)$, the second as $L_a(\pi\pi^*)$, and also pointed out a third one, $\pi\sigma^*$, that seems to be involved in the photoexcitation processes. It was shown that the π orbitals located on the indole ring are involved in the L_b and L_a states. The results also provided the possible deactivation mechanisms which can be either a low-lying conical intersection of the $S_1(n\pi^*)$ and S_0 potential-energy surfaces or a detachment of the neutral NH_3. Other scenarios were presented showing that the photochemistry of the zwitterion tryptophan is not yet understood.

For the protonated form ($Trp+$), that is the predominant species at low pH, *ab initio* studies on the excited state deactivation processes were reported following UV excitation. [57] [58] In comparison to neutral tryptophan (Trp), in the protonated form the complexity is even higher because of the existence of different tautomers. Probable protonation sites are: (1) the amine group, (2) the indole hydrogen, and (3) the indole carbon. Gilles Grégoire *et al.* [57] calculated the lowest energetic possible tautomers and discussed the ones that are expected to be experimentally accessible. These calculations were performed for isolated compounds for comparison with gas phase experiments.

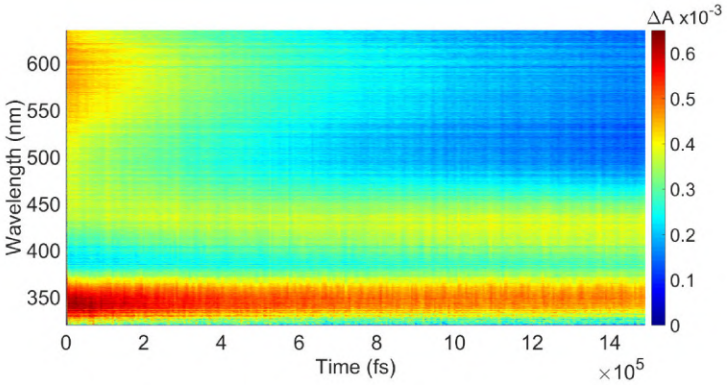
Although a quantitative comparison with our data is not possible, the results showed that the energetic position of the L_b state is insensitive to protonation and to the proton position. In contrast the L_a state shifts upwards (blue shift) upon protonation. [58] The femtosecond pump-probe experiment exhibited an ultrafast decay with two time constants of 400 fs and 15 ps. The short one was assigned to the dynamics on the $\pi\sigma^*$ state surface along the free NH stretchcoordinate, and the long one to the dynamics on the $\pi\pi^*$ state that decays through proton transfer to the indole ring. [57]

Most of the ultrafast ultraviolet spectroscopy experimental works in aromatic amino acids were performed in gas phase condition which is not the focus of this work. It is possible to find the main results in the review by Satchin Soorkia *et al.* [1]. In the Jérémie Léonard papers [59], [60], they present ultrafast excited state dynamics of tryptophan in water using a pump-probe setup. Excitation was at 266 nm with the probe pulse covering the VIS range ($300 - 700$ nm). They observed only positive signals which means that excited state absorption (ESA) signals dominated, even in the region from 310 to 370 nm, in which it is expected to detect stimulated emission (SE) signal. They observed 3 ESA: the first one is around 330 nm that shifts towards 350 nm on the nanosecond time scale, the second one around $500 - 600$ nm that decreases on the picosecond time scale, and a third one initially centered at 450 nm that seems to shift to 425 nm also in the nanosecond time scale. We obtained transient absorption results with similar features using the third harmonic experimental setup.

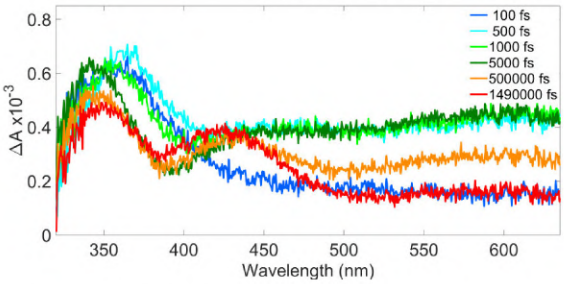
4.3.2 Transient Absorption Measurements

In this section we present the results for excited state dynamics of tryptophan in solutions with different pHs by femtosecond transient absorption experiments. We excited the samples with 266 nm pump pulses and measured their transient absorption with a $330 - 700$ nm white light supercontinuum probe, set at magic angle ($54.7°$) [15] [61] [62] with respect to the pump; the time resolution is 120 fs (the details of the setup are described in section 3.1.1.1). The samples were circulated in a 1 mm thick quartz cuvette using a peristaltic pump. In Fig.27 we show the transient absorption results for the neutral pH: the 2D pump-probe map, the time-resolved absorption spectra at some selected delay times and the wavelength-resolved absorption signal at some selected wavelengths. All signals are positive indicating that the photoinduced absorptions (PA) dominate the stimulated emission (SE) signals. The results were compared with theoretical calculations to obtain the deactivation processes.

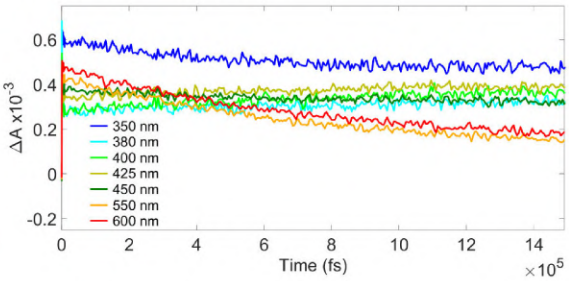
The first values obtained from the calculations were the vertical excitation energies and their oscillator strengths that are involved with the linear absorption, as we can see in Fig.28. To know which one is responsible for the excitation from the ground state and also to reproduce the linear absorption (LA) spectrum of Trp, simulations of the absorption



(a) 2D pump-probe map of transient absorption



(b) Time-resolved absorption spectra extracted from the 2D map for 100 fs to 1.5 ns.



(c) Wavelength-resolved absorption signal extracted from the 2D map for the 350 – 600 nm probe range.

Figure 27 – Transient Absorption of Trp in phosphate buffer saline, pH 7.4, after excitation at 266 nm.

spectrum were performed for six possible tryptophan conformers. The graph in Fig28 a) is the final LA spectra based on these 6 conformers. The weight for the population of each state is proportional to the intensity of the single spectrum on the total one. From this simulation and also from the Gaussian fit in the LA spectrum, we can conclude that after excitation from 290 nm until 260 nm we are mainly populating the L_a state, as illustrated in Fig.28 c). The Gaussian fit of the LA spectrum shows that the broad Gaussian obtained at 232 nm (5.34 eV) works as a background (for any higher energy transitions) and the other at 281 nm (4.41 eV) can be just a L_b vibronic band, as presented in the reference [63]. In the simulations we obtained L_a centered at 268 nm (4.63 eV), close to the experimental value - 273 nm, and L_b at 277 nm (4.47 eV) which seems to differ slightly from the experiment - 289 nm. We believe these calculations are made at a better level compared to the ones in the literature and because L_a and L_b are so close, different calculations methods could switch them giving rise to a different scenario.

Some calculations were performed to explain the PA peaks in the pump-probe map. In Fig.29 we can see the spectra from the initial time delays between pump and probe - the spectra related with the initial dynamics -, and also the simulations of the PA peaks that can explain from each state those absorptions came from. We propose this scenario: initially, pumping the molecule at 266 nm we are populating the L_a state, then

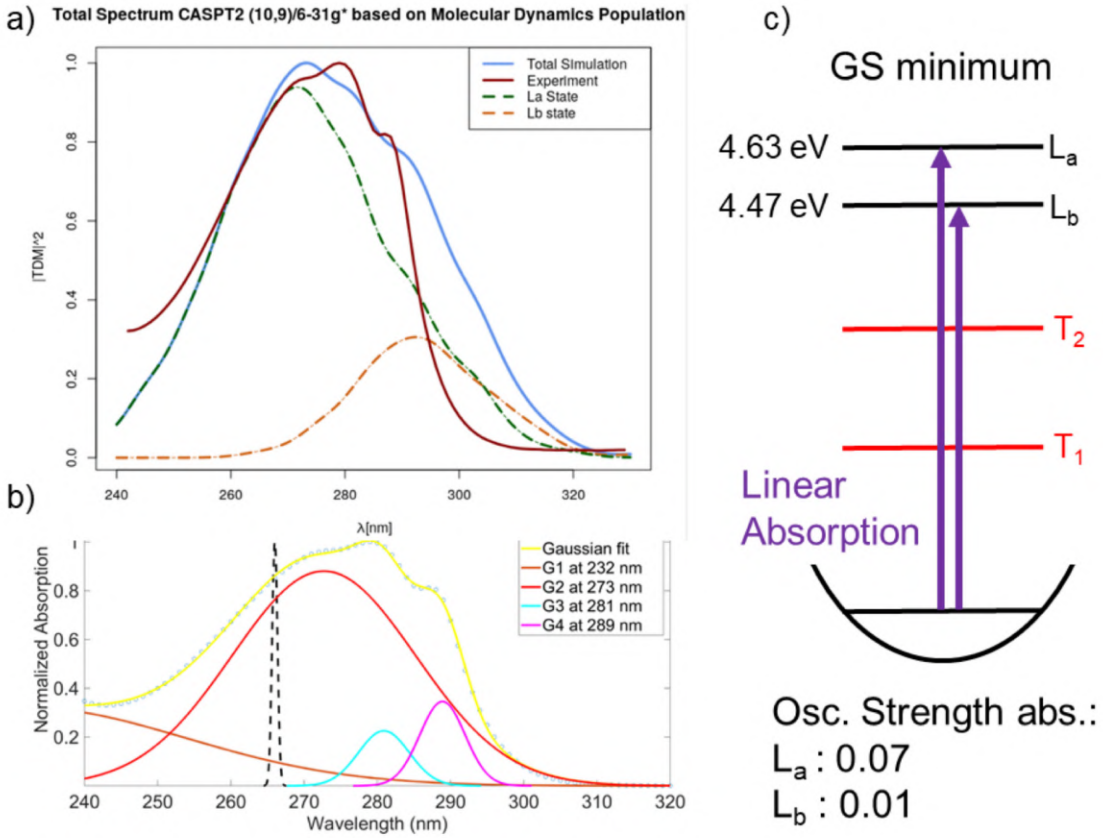


Figure 28 – First vertical excitations for tryptophan: a) total linear absorption spectrum obtained by the overlap of LA spectrum of six conformer of tryptophan; b) experimental LA spectrum of tryptophan in buffer saline with a Gaussian fit with 4 components; c) schematic drawing of the first excited states of tryptophan obtained from the calculations of the LA spectrum.

because the first PA signal appears at 360 nm and in the simulation there is a PA signal from the minimum of L_b in this wavelength, before there should have been an ultrafast internal conversion (IC) from L_a to L_b. This IC happens faster than our time resolution as we could not detect any signal coming from L_a or L_b in the Franck-Condon region. In fact, new measurements were done in a setup with better resolution (around 20 fs), and even in this condition the first signal detected was a PA coming from the minimum of L_b as we can see in Fig.30. This setup consists of a visible non-collinear optical parametric amplifier followed by second harmonic generation and prism pair compressing system (for more details see the reference [37]) which allowed us to excite the tryptophan at 285 nm. These measurements were performed by the researcher Piotr Jan Kabacinski as part of his doctorate at Politecnico di Milano. The results showed in the graph lead us to conclude that the first IC predicted by the calculations happens before the 50 fs time delay. From the minimum of L_b was also predicted a stimulated emission (SE) at 302 nm (oscillator strength, OS, of 0.02), but this signal is outside of our measurement region. We believe that this stimulated emission at 302 nm seems to be detected in the new measurements where the resolution is better and also the probe spectrum extends

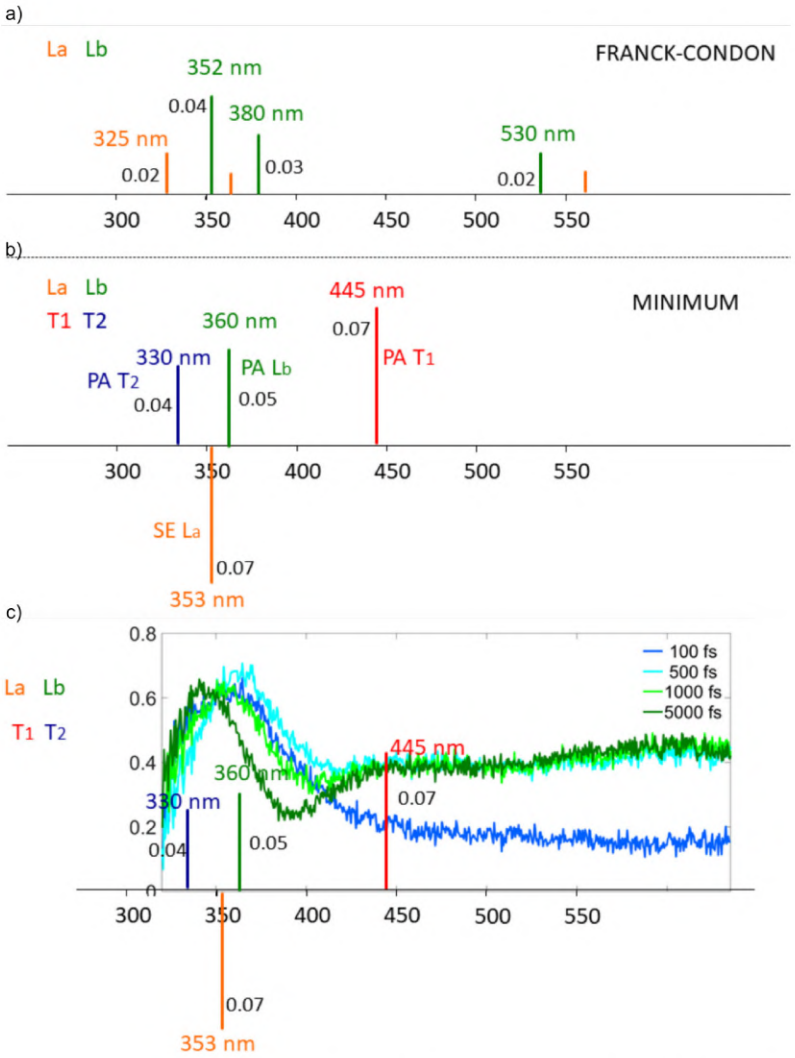


Figure 29 – Photoinduced absorptions (PA) and stimulated emissions (SE) calculations for tryptophan in water: a)PA from the L_a and L_b in the Franck-Condon region; b)PA and SE of the singlets, L_a and L_b, and the triplets, T_1 and T_2, in their own minimum; c)transient absorption spectra of tryptophan in buffer saline for the first time delays with the predicted PA and SE signals.

to 310 nm. The evidence of the SE comes from the coherent oscillations centered at 330 nm as showed in Fig.30. Two-dimensional Fourier analysis of the probe spectrum with the calculations showed that these oscillations at 330 nm are excited vibrational mode of L_b state. In time resolved fluorescence measurements the emission from the L_b state was detected at 32000 cm^{-1} (312.5 nm), but was not the main signal since their resolution was about 180 fs and they were mainly exciting the L_a state. [64] From the minimum of L_b, the calculations predicted another internal conversion from L_b to L_a, this is supported by the decreasing of the signal at 360 nm and also a SE signal that is from the minimum of L_a at 353 nm (OS of 0.07). This signal at 353 nm was observed in our steady state photoluminescence (in Fig.25, section 4.2) and in time resolved fluorescence too [65] [64], but in the pump-probe it is certainly less intense than the PA at 360 nm, that is why we only see the decrease of the PA signal. The second IC, L_b to L_a, happens around 500

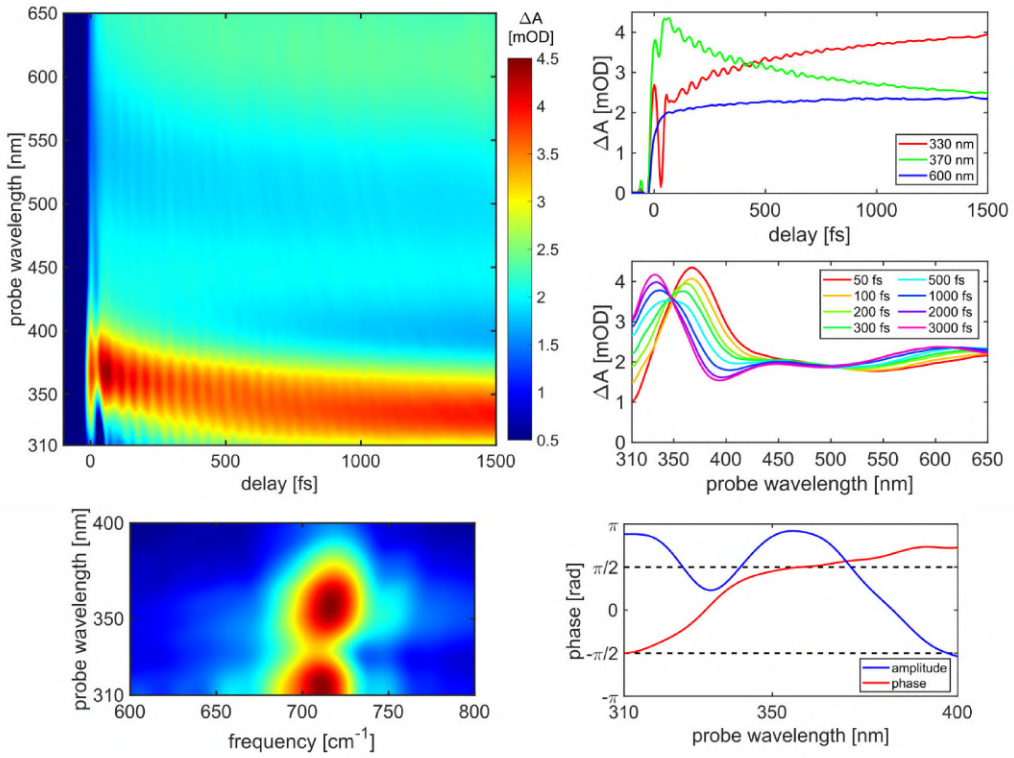


Figure 30 – Transient absorption of tryptophan after excitation at 285 nm: in the top of the figure we have 2D differencial absorption map and in at the bottom 2D Fourier transform of the probe spectrum with amplitude and phase of the mode at 720 cm^{-1}.

fs. Then we observed a blue shift of the spectrum, from 360 to 340 nm, the PA signal at 340 matches with a calculated PA that comes from the T_2 state at 330 nm (OS of 0.04). The PA of T_2 is well established in the pump-probe map around 5 ps and remains there until 100 ps, so the intersystem crossing (ISC), from L_a to T_2 seems to happen in less than 5 ps. Then from T_2 there are more than one possibility for the deactivation process at longer delays, as illustrated in Fig.31. The first possibility could be an internal conversion from T_2 to T_1 where in T_1 was predicted a PA at 445 nm. The last PA detected in the pump-probe map is not centered at this wavelength but because the signal is very broad (centered at 425 nm), this may explain our last signal. The second one is related to a photoproduct, the protonated tryptophan ($Trp+$). Other calculations were performed to obtain the PA signals from different tautomers and the structure that presented good agreement with our measurements is the one that exhibits protonation in the carbon four, see the details in Fig.32. Besides that, Isao Saito *et al.* [66] showed that $Trp+$ tautomer in carbon four is formed in tryptophan neutral solutions after excitation with light. These photoproduct formation was pointed out as a mechanism of nonradiative decay of singlet excited tryptophan in aqueous solutions. For this species it is expected an absoption at 423 nm (from S_0, ground state, with OS of 0.09), another one at 350 nm (from S_0 with OS of 0.15), and a PA at 344 nm (from T_{p1} with OS of 0.16). In this way from T_2 we can also propose the formation of the $Trp+$ which would explain the increase of the signal

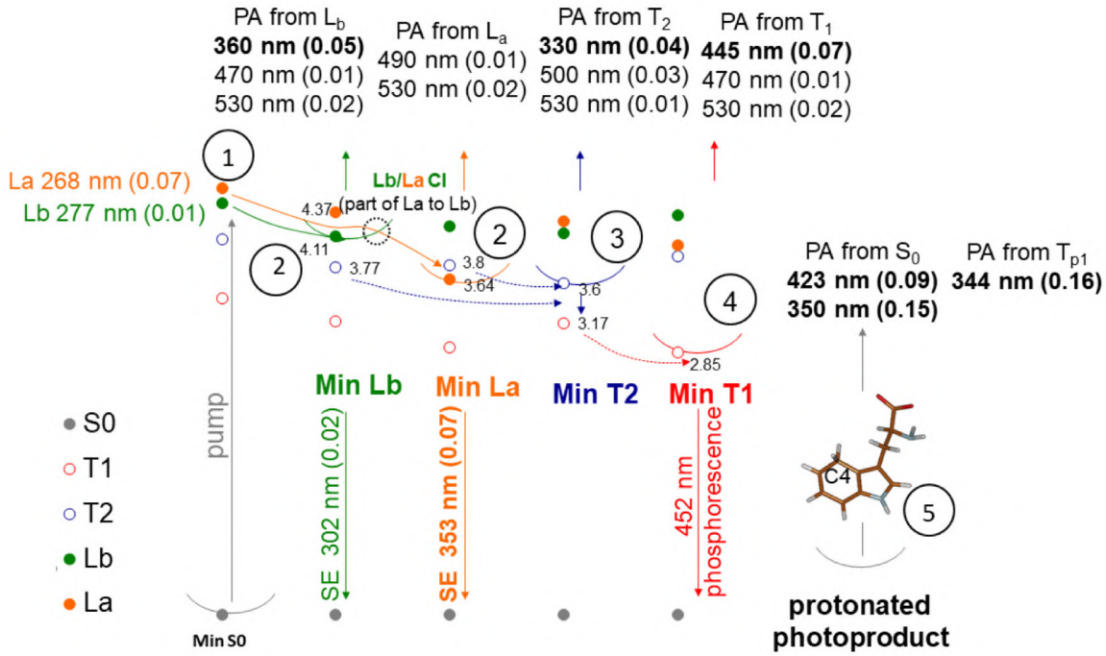


Figure 31 – Schematic drawing for tryptophan deactivation processes in neutral pH after excitation at 266 nm. This is a complex scenario that shows two different possibilities for long delays: the first one shows a IC from T_2 to T_1 state and then to the ground state with a phosphorescence signal at 452 nm; the second one shows a photoproduct formation from T_2 state. The strongest signals predicted in the calculations are shown in bold.

at 425 nm, the remain of the signal at 350 nm, or maybe instead of the 350 nm peak we are detecting the remaining signal at 344 nm. The photoinduced absorption values calculated for this photoproduct are preliminary results that is why we do not have a complete electronic description from it.

We also studied the tryptophan in acid medium and hence we dissolved the molecule in hydrochloric acid at pH 1.0. In Fig.33 we compare the linear absorption spectrum in the two different conditions. As indicated they are quite similar, the small difference appear close to the vertical excitation for L_a state and to higher energies transition. When we compare the Gaussian fits, only the component responsible for higher energy transitions is different.

In the Fig.34 we can see the transient absorption map for tryptophan in pH 1.0. Surprisingly, in the transient absorption measurements we also observed subtle changes in acid medium in comparison with the neutral. The first difference appeared from 550 to 640 nm in the spectral range in which a photoinduced absorption centered at 600 nm was detected. We believe that the PA centered at 600 nm is due to solvated electrons that exhibit long-lived transient absorption signal in the visible region. [67] [68] In the acid solution this signal was much stronger than in the neutral solution, as expected, showing

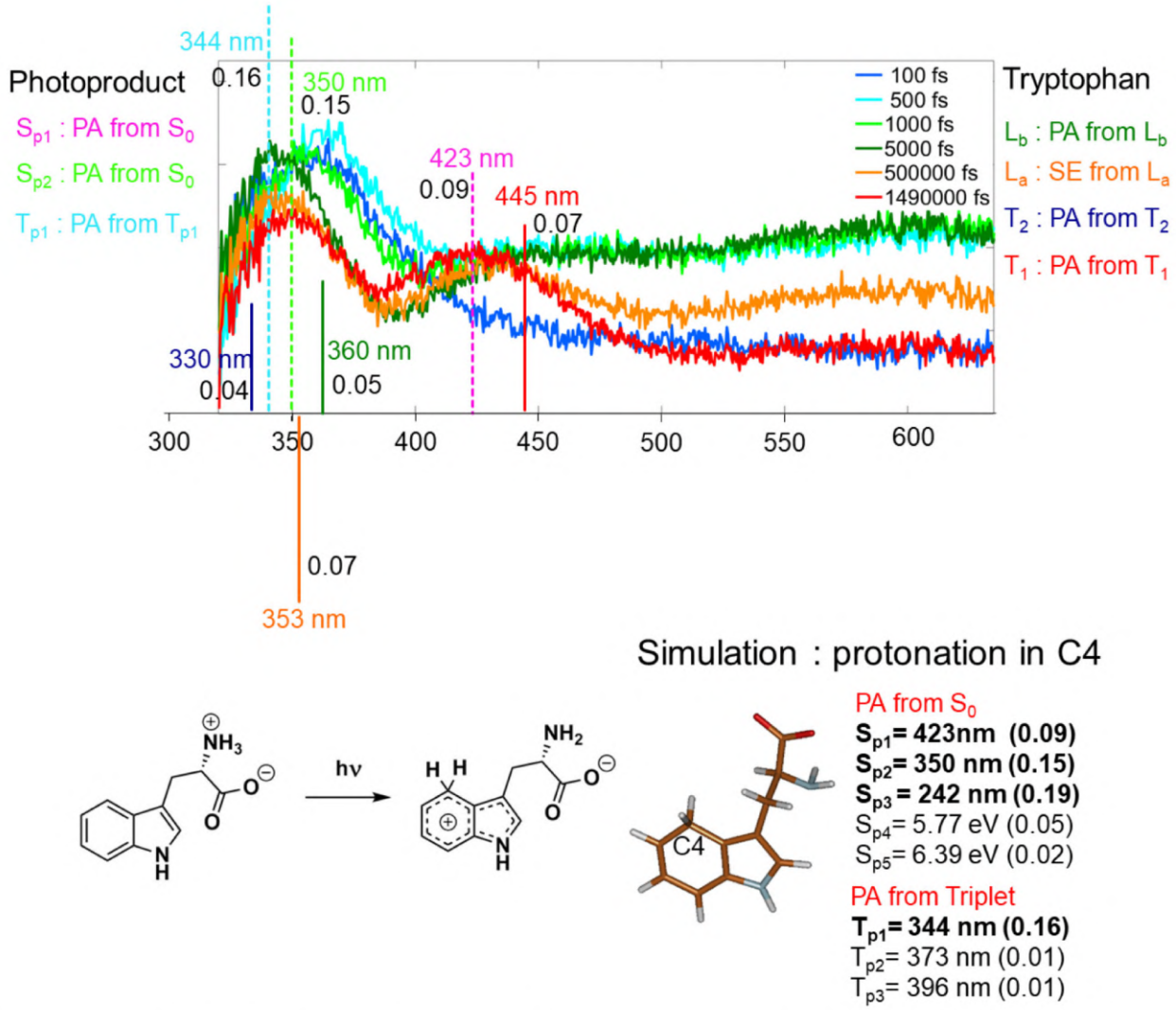


Figure 32 – In the bottom right of the figure we present the PA calculations for the tautomer $Trp+$ in carbon four that showed greater agreement with the signals detected in transient absorption spectra, showed in the top. One mechanism of nonradiative decay of tryptophan in neutral solutions is the formation of this photoproduct as showed in the bottom left of the figure.

the excess of $H+$ ions in the medium. The other differences were related to tryptophan behavior in acid medium: in the first 5 ps we observed the blue shift from a PA centered at 370 nm to a PA centered at 350 nm and here the PA centered at 450 nm started to form in 1 ps. Then at 500 ps the PA signal at 450 nm does not disappear, its intensity remained fixed until the maximum time delay of the measurement, but the center position of the signal shifts to 425 nm, and the PA at 350 nm becomes broad, decreasing the contribution at 350 nm and increasing the signal at 370 nm. Finally, at 1.5 ns the PA at 425 nm increases even more and the PA at 370 nm does not seem to decay in this time scale.

The clear picture of what is happening with tryptophan in acids medium only will be possible under scrutiny of theoretical calculations over protonated tryptophan species.

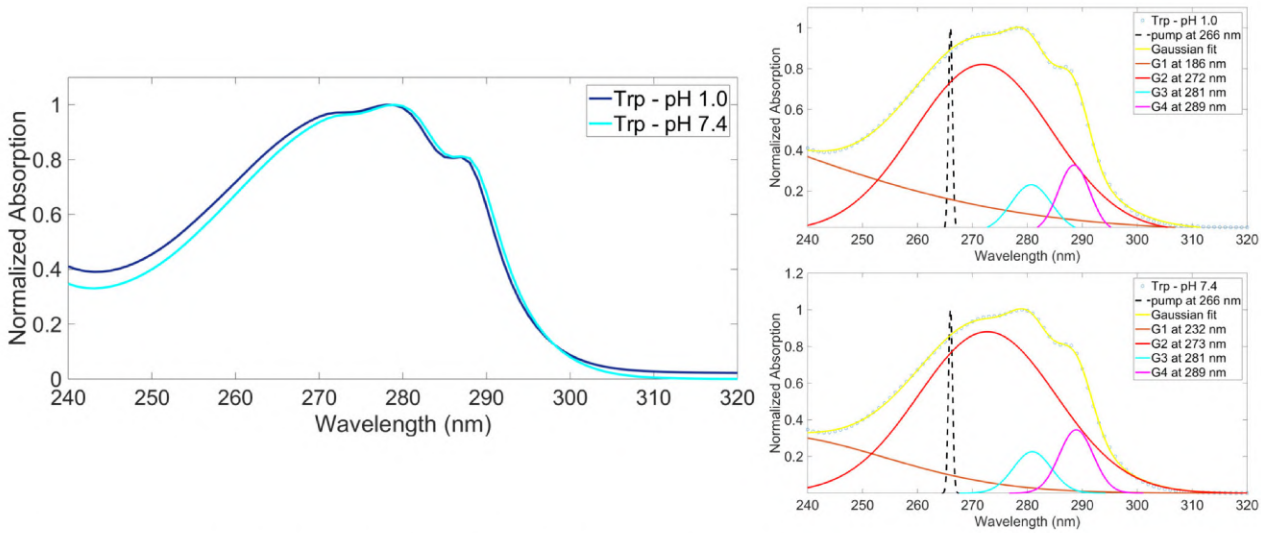
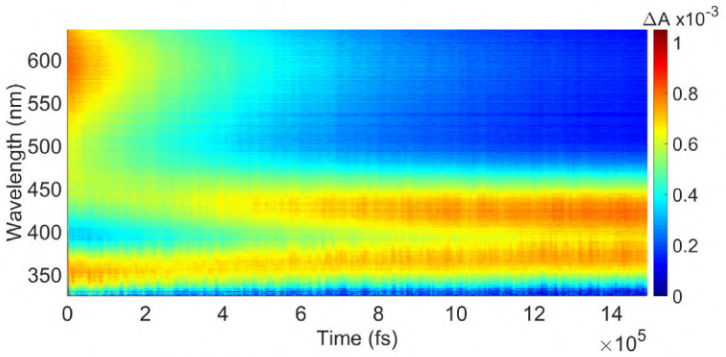
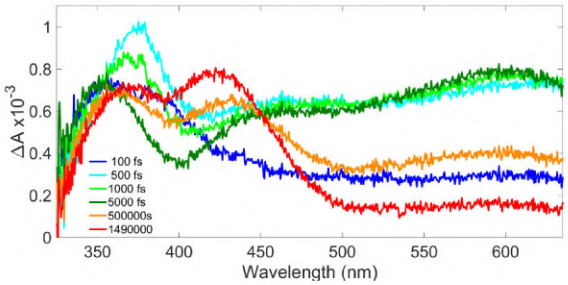


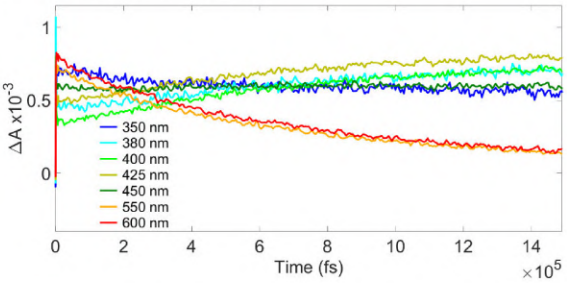
Figure 33 – Linear absorption spectrum for tryptophan in acid and neutral medium and their Gaussian fits respectively.



(a) 2D pump-probe map of transient absorption



(b) Time-resolved absorption spectra extracted from the 2D map for 100 fs to 1.5 ns.



(c) Wavelength-resolved absorption signal extracted from the 2D map for the 350 – 600 nm probe range.

Figure 34 – Transient absorption of Trp in hydrochloric acid aqueous solution, pH 1.0, after excitation at 266 nm.

When we compare the spectra for the neutral solution with the acid solutions (see Fig.35), and analyze the possible photoinduced absorptions signals for the protonation C4 species, we conclude that we have limited informations. Based on the measurements, we believe that even in the acid medium we still have contributions for the zwitterion species in the transient absorption mixed with protonated species signals.

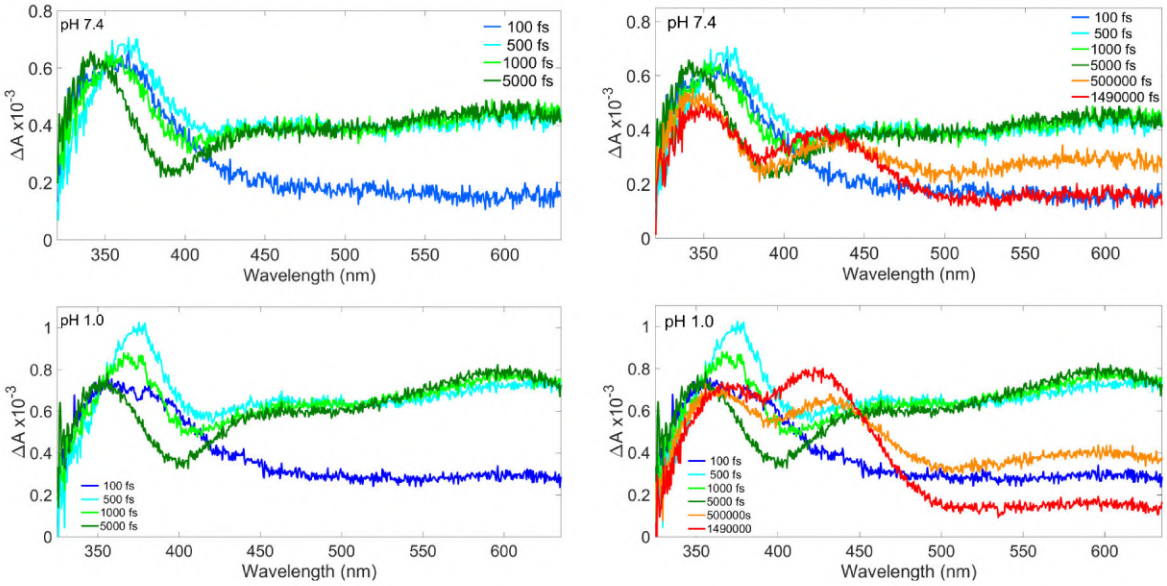
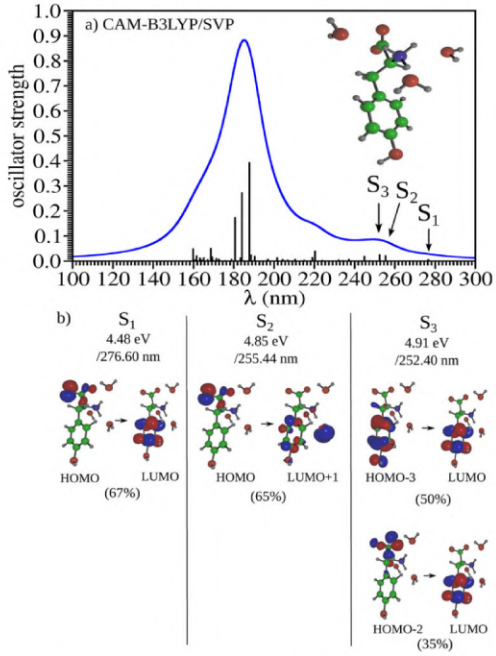


Figure 35 – Tryptophan transient absorption spectrum at pH 7.4 in comparison to tryptophan at pH 1.0. We clearly see contributions from the zwitterion species in the acid medium and vice versa.

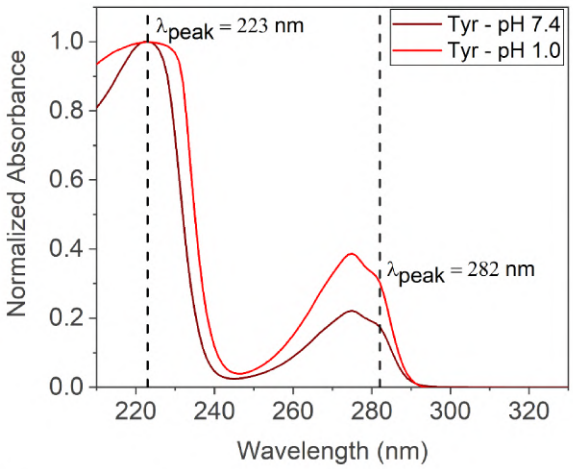
4.4 Tyrosine

4.4.1 State of Art

Time-depend density functional theory (TDDFT) combined with quantum mechanical/molecula mechanical approach was applied to study the photodynamics of tyrosine in the gas phase and in water. [69] Gaia Tomasello *et al.* performed calculations of the eletronic absorption spectra of tyrosine with three explicit water molecules embedded in a classical water sphere via TDDFT, showing the character of the first three excited states in terms of the orbital excitations. We extracted their results to compare them with our linear absorption spectra, and as shown in Fig.36 they are in great agreement. The spectra show the first transition



(a) Eletronic absorption spectrum of tyrosine calculated with TDDFT. This figure was extracted from Gaia Tomasello *et al.*, ref. [69].



(b) Linear absorption spectra of tyrosine measured at pH 7.4 and at pH 1.0.

Figure 36 – Absorption spectrum of tyrosine obtained via TDDFT in comparison with our linear absorption spectrum measured at different pHs.

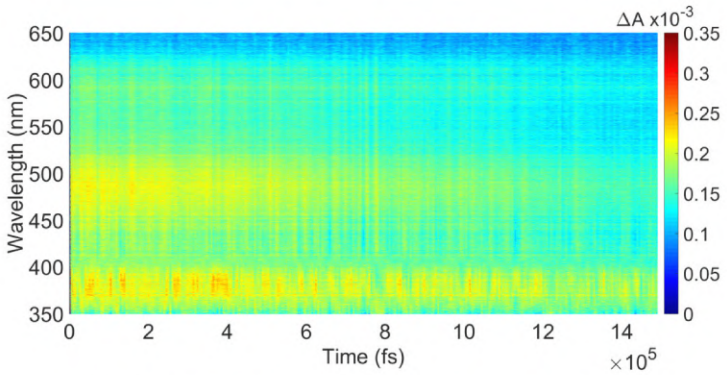
with a $\pi\pi^*$ character at 252 nm which corresponds to the S_3 state. The other states, S_1 and S_2, presented less intense transitions and have $\pi\pi^*$ mixed with $n\pi^*$ character. They also calculated the relaxation snapshots for a selected trajectory of tyrosine in water. Starting in the S_3 state the molecule comes back to the ground in 170 fs with an ultrafast decay from S_3 to S_1 and then reaching the ground state through a conical intersection.

Transient absorption measurements were reported for tyrosine at pH 9.0, for its chromophore phenol in water, and for phenolate (phenol deprotonated form) at pH 13. [70] [71] [72] [73]In all of them only positive signals were observed when they excited the samples at 266 nm and probed in the VIS range (in the tyrosine measurements the

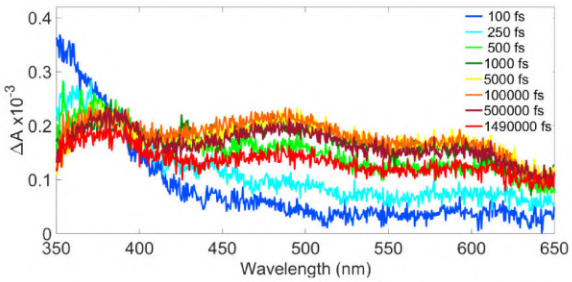
excitation was at 280 nm). In similarity with our measurements they detected the broad PA signal around 600 nm which we believe is associated with solvated electrons and another PA signal at 505 nm (for tyrosine, and 515 nm for phenolate) which could be associated to a photoinduced absorption from the singlet excited state S_1.

4.4.2 Transient Absorption Measurements

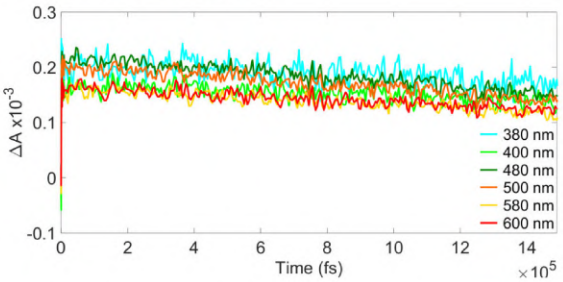
In this section we present the results for the excited state dynamics of tyrosine in solutions with different pHs by femtosecond transient absorption experiments. To the best of our knowledge, this is the first time that such results are presented for tyrosine. We excited the samples in the same experimental conditions as for tryptophan (details in Chapter 4.3.2). In Figs. 37 and 38, we show the results for tyrosine in neutral pH solution. For these measurements we do not have the theoretical calculations to assign



(a) 2D pump-probe map of transient absorption



(b) Time-resolved absorption spectra extracted from the 2D map for 100 fs to 1.5 ns.

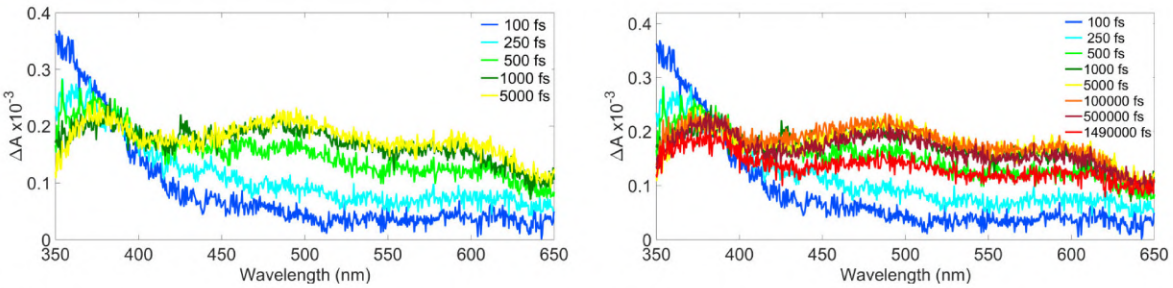


(c) Wavelength-resolved absorption signal extracted from the 2D map for the 350 – 600 nm probe range.

Figure 37 – Transient absorption of Tyr in phosphate buffer saline, pH 7.4, after excitation at 266 nm.

each excited state absorption peak to their respective state. The interpretation of these data are based on our measurements and the literature. We only observed positive signals in the spectra map, which means that the three PA signals are stronger than the possible SE signals. From the fluorescence measurements we could expect a SE signal from 290 to 340 nm, which is outside the spectral region we measured, and from the phosphorescence measurements from 380 to 425 nm which is outside of our time delays measured. [55] In

time resolved fluorescence measurements was shown that the time decay for the emission spectrum was in the nanosecond time scale, and we should not expect to detect the phosphorescence (time decay in the order of seconds [74]) in our measurements. Hence we assigned the initial dynamics to the singlet states of tyrosine and the radicals that can be formed due to excitation. Comparing with Gaia Tomasello *et al.* results [69], we assigned



(a) Time-resolved absorption spectra extracted from the 2D map for 100 fs to 5 ps.

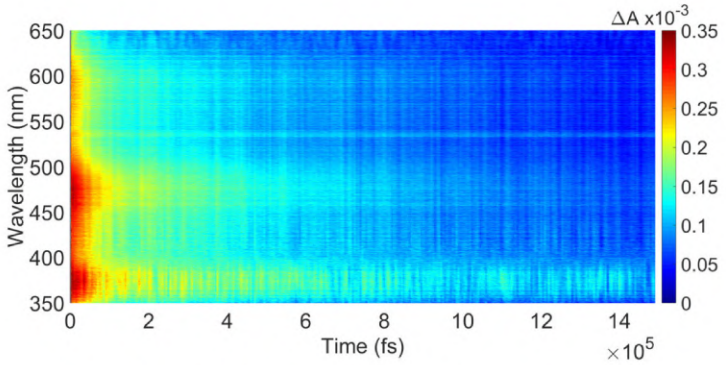
(b) Time-resolved absorption spectra extracted from the 2D map for 100 fs to 1.5 ns.

Figure 38 – Time-resolved absorption spectra extracted from the 2D map for 100 fs to 1.5 ns of Tyr in phosphate buffer saline, pH 7.4, after excitation at 266 nm.

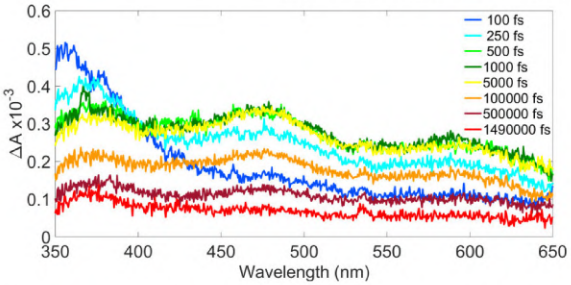
the first peak in the linear absorption spectrum to the first three excited states S_1, S_2, and S_3 states. They also calculated the character of the first excited states, showing that the spectrum exhibits a $\pi\pi^*$ character for the first transition which corresponds to a S_0 to S_3 (labeled as L_b according to the Platt notation) transition. Thus, we propose this scenario: initially, pumping the molecule at 266 nm we are populating the L_b state, since the linear absorption spectrum showed two peaks, one at 225 nm (5.51 eV) and another at 282 nm (4.39 eV), identified as L_a and L_b states respectively. Then an ultrafast deactivation of the initially excited bright $\pi\pi^*$ state by internal conversion to the S_1 must be happening within the first few hundred femtoseconds. From the minimum of S_1 is predicted a SE at 303 nm due to fluorescence, but also an intersystem crossing from S_1 to T_1, from where a phosphorescence at 395 nm is predicted, and a PA at 505 nm which was measured in transient absorption for tyrosine at pH 9 [70]. In our transient absorption spectrum we detected three ESA signals, the first one at 380 nm, the second at 480 nm, and the third one at 600 nm, all fully formed in the time scale between one to five picoseconds. We believe that the signal at 480 nm can be related to a PA from the tyrosine S_1 excited state. Because a PA at 505 nm has already been reported in transient absorption measurements for tyrosine at pH 9 after excitation at 280 nm in agreement with the previous assignment of a 515 nm band to the PA from S_1 excited state of phenolate (deprotonation form of phenol) [70] [71] [73]. The PA at 600 nm seems to be related to the solvated electrons, as previously mentioned they give rise to a broad absorptive band centered at 720 nm. The PA at 380 nm maybe is related to photoproduct signals since radicals are expected to exist in aqueous solutions of tyrosine after UV excitation. In tyrosine aqueous solutions at pH 9, tyrosyl radicals have been generated and were monitored by a narrow absorption band

at 410 nm. But most likely they are not the same species since their absorption shapes are quite different.

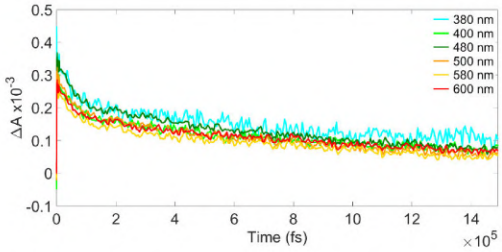
We have also perfomed transient absorption measurements for tyrosine in an acid medium. The results for the molecule dissolved in HCl aqueous solution at pH 1.0 are shown in Fig.39.



(a) 2D pump-probe map of transient absorption



(b) Time-resolved absorption spectra extracted from the 2D map for 100 fs to 1.5 ns.



(c) Wavelength-resolved absorption signal extracted from the 2D map for the 350 – 600 nm probe range.

Figure 39 – Transient absorption of Tyr in HCl aqueous solution, pH 1.0, after excitation at 266 nm.

The main difference between the neutral and acid media is the change in the relaxation time dynamics. In the neutral, the three PA signals had started to decrease only on the nanosecond time scale; on the other hand in acid, the PA signals had presented time decays around 100 ps, and on the nanosecond time scale all signals have already vanished. But the peak positions and the shapes for the three signals are very similar to the ones in the neutral solution. There is only a signal that is hard to describe, because it is in the edge of the spectrum, presented at the initial time, 100 fs. This absorption peak showed a red shift in the acid medium with respect to the neutral: its position seems to be below 350 nm in neutral and around 350 nm in the acid. If this difference really exists, it could be related to the distinct radical species forming in the different pH solutions.

4.5 Phenylalanine

4.5.1 State of Art

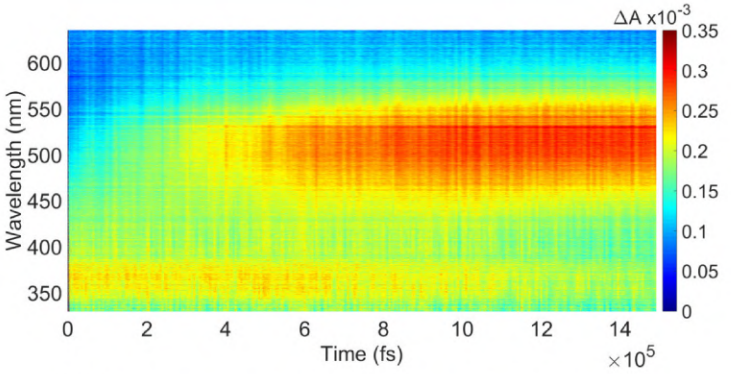
Theoretical calculations on the deactivation mechanisms of neutral (Phe) and protonated phenylalanine ($Phe+$) in gas phase were reported in the literature. The potential energy profiles for both species, at different eletronic states was investigated using RI-MP2 and RI-CC2 methods with the Turbomole program suit. [75] The *ab initio* calculations showed that the first vertical transition ($S_0 - S_1$) energy in protonated and neutral phenylalanine is quite similar, but there is a large discrepancy between the second transition ($S_0 - S_2$) in the species. In addition, the optical transitions to the lowest excited singlet states (S_1, S_2) of both species had presented weak oscillator strengths in the UV range. The $S_0 - S_1$ and $S_0 - S_3$ transitions have a $\pi\pi^*$ character for Phe and $Phe+$ while the $S_0 - S_2$ has a $n\sigma^*/n\pi^*$ and a $\pi\pi^*$ character respectively. Although it is not possible to quantitatively compare the excited transition energies of Phe and $Phe+$ computed with this method with our linear absorption spectra, we should expect a similar behavior for the both species in solution. [75]

The UV absorption of phenylalanine in gas phase [76], [77] and fluorescence [78], [79] spectra of phenylalanine in solution have been studied, but to our knowledge, there is only one work [80] that shows ultrafast pump-probe spectroscopy of phenylalanine in solution. It is only a conference abstract that provides little information. The time resolved absorbance revealed two decay components of 146 fs and 1.4 ps in which the first one was assigned to the relaxation via a conical intersection from the main excitation band. The time-resolved absorbance spectrum was not showed, only the time traces extracted from the 2D pump-probe map.

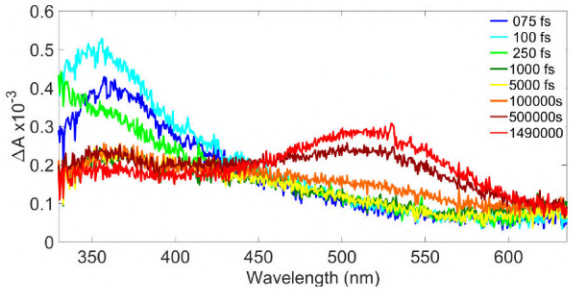
4.5.2 Transient Absorption Measurements

We measured the excited state dynamics of phenylalanine in solutions with different pHs by femtosecond transient absorption experiments. We excited the samples pumping with the third harmonic setup and probe in the VIS with the WLC in CaF_2 crystal, in the same way that was done for tryptophan and tyrosine. To the best of our knowledge, this is the first time that the complete time-resolved spectrum and time traces of phenylalanine in solution is presented. In Fig.40 we show the transient absorption results for the neutral pH.

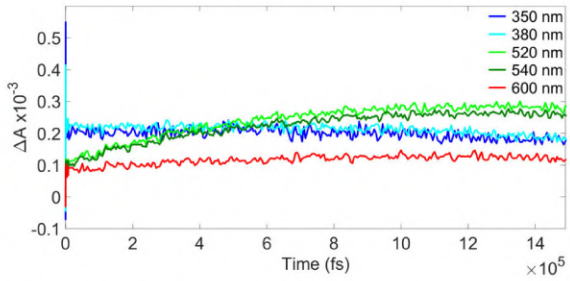
From the linear absoption spectra (absorption peak detected at 263 nm), shown in section 4.1, we can assume that excitating the phenylalanine in phosphate buffer saline at 266 nm, we are excitating close to the lower band ($S_0 - S_1$ transition) and shoud not expect vibrational relaxation. Stimulated emission signals are expected at 282 nm (from 265 to 324 nm) which is related to PL spectra signal, and at 380 nm (from 350 to 440 nm)



(a) 2D pump-probe map of transient absorption



(b) Time-resolved absorption spectra extracted from the 2D map for 75 fs to 1.5 ns.



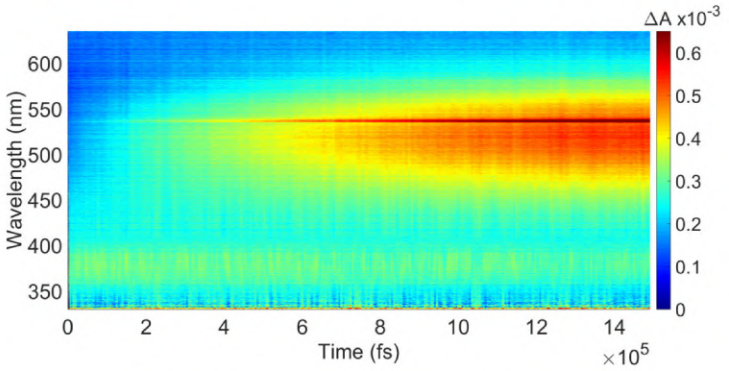
(c) Wavelength-resolved absorption signal extracted from the 2D map for the 350 – 600 nm probe range.

Figure 40 – Transient absorption of Phe in phosphate buffer saline, pH 7.4, after excitation at 266 nm.

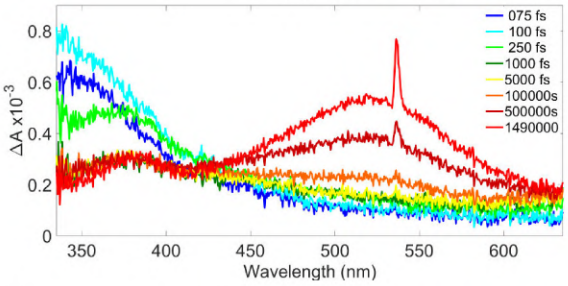
that was reported in phosphorescence measurements in the literature [74]. However, in our transient absorption measurements these signals may not be observed: the first one is not in our spectral windown range and from time-resolved fluorescence in phenylalanine that showed fluorescence spectrum with 7 ns time decay, the phosphorescence signal should not appear because we had measured time traces up to 1.5 ns time scale. We observed two PA, one at 360 nm and another at 530 nm that have different time dynamics (see Fig.40). The first PA is completed formed up to 100 fs time scale and starts to decay with 250 fs. However the signal does not vanish, we could detected a remained signal up to 1.5 ns time scale. Pump-probe delayed ionization measurements of Phe in gas phase showed that the lifetime for the first excitated stated, S_1, was estimated to be in the nanosecond range. [81] We believe that the photoinduced dynamics of the molecule in gas phase and in solution should be completed different, even though that measurement can be the indicator to assign the second PA coming from de S_1 state and the first one to be assigned to photoinduced processes coming from the new species ($Phe+$). The second PA appeared in the time-resolved spectrum from the first 100 ps and until the end of the mesurement it does not give indication of decay.

The pump-probe measurements of phenylalanine in acid medium gives support for our interpretation for the PA signals discussed above. In Fig.41 we show the 2D pump-probe

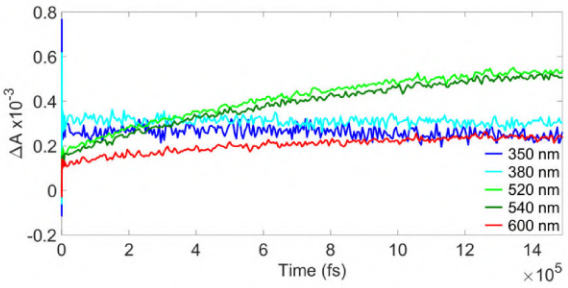
map, the time-resolved absorption spectra at some delay times and the wavelength-resolved absorption signal at some selected wavelengths for phenylalanine in hydrochloric acid aqueous solution (pH 1.0). The differences between the time-resolved absorption spectra



(a) 2D pump-probe map of transient absorption



(b) Time-resolved absorption spectra extracted from the 2D map for 75 fs to 1.5 ns.



(c) Wavelength-resolved absorption signal extracted from the 2D map for the 330 – 635 nm probe range.

Figure 41 – Transient absorption of Phe in hydrochloric acid aqueous solution, pH 1.0, after excitation at 266 nm.

obtained in neutral and acid pH are even smaller for phenylalanine compared to the other molecules. We could not detect differences in the time traces, but only a subtle difference in the 330 – 400 nm spectral region. This can be due to different species signatures or it may be due to the fact that this region is at the edge of the measured spectral windown. If it is the first option, thus this will support our interpretation that the PA at 360 nm is a photoproduct signal and the PA at 530 nm is an absorption from the S_1 state of phenylalanine. These similarities in the spectra are in line with what has been reported in the literature, since the first vertical transition ($S_0 - S_1$) energy in protonated and neutral phenylalanine molecules is quite similar.

We also measured trasient absorption of tryptophan, tyrosine, and phenylalanine in a buffer solution at pH 5.35. These measurements show very similar results as to the neutral pH, but for completeness we included them in the AppendixA.2. All the measurements shown above were done with pump and probe polarization at the magic angle, 54.7°, to be sure that there will not be any rotational contribution in the measurements. However, we have also measured the transient absorption of the three molecules in hydrochloric acid aqueous solution with parallel and perpendicular polarization to try to extract additional

information of the photoinduced processes. Unfortunately, the change in light polarization also complicates the interpretation of the maps, thus we are not sure if the differences that were detected are due to rotational diffusion of the molecules. We included these measurements in the AppendixA.2.

5 Results - Hyperspectral Imaging

5.1 Hyperspectral Camera

5.1.1 Spectral and Reflectance Calibration

The hyperspectral camera was designed to obtain spectral and spatial information in the macro scale. However, as we showed in section 3.1.3.1, the contrast depends on the optical configuration for collecting light - a large field of view implies in a large dispersion of angles for the incoming light. So, before showing how the system works with the artwork application, we will show some measurements we did to characterize it.

To evaluate the spectral resolution and sensitivity of the hyperspectral camera, we imaged four Spectralon color materials (green (G), blue (B), red (R), and yellow (Y)) which are calibrated diffusive reflectance standards (Labsphere Inc., North Sutton, USA), with $98.3 \pm 1.3\%$ of reflectance from 300 nm to 2.5μm range. In addition, the beams of a green ($\lambda = 532$) nm and a red ($\lambda = 635$) nm diode laser were directed on points L_1 and L_2 (see Fig.42(d)) respectively, and were used to measure the spectral resolution of our system. The total scan length of the translation stage was adjusted to achieve the desired spectral resolution in each measurement. In the first measurement, that was performed to obtain the refractance of the Spectralon color materials, we acquired 400 images, scanning the position of the wedges from -1 mm to 1 mm around the zero path delay (ZPD). The samples were illuminated by a 150 W Xenon lamp, and the objective of the camera lens was set at the largest aperture, resulting in a exposure time of 25 ms for each image. In Fig.42, we show the spectral information retrieved from the hyperspectral imaging from each pixel in the Spectralon color materials. The dashed lines are the certified reflectivity values, while the solid lines are the spectra obtained in our setup, and averaged over the surface of each standard. Absolute reflectance was calculated after spectral calibration with the white Spectralon (W) and correction for spatial and spectral non-uniformities of the illumination by imaging a white Lambertian surface at the object plane (data not shown). The spectral accuracy for each colorimetric sample, estimated as the standard deviation of the difference between measured and certified spectra, was smaller than 2.18%. This shows that our hyperspectral camera is able to measure absolute reflectance with very high accuracy in the visible and near-infrared spectral range ($400 - 1000$ nm).

The other measurement were performed to obtain the spectral resolution of the system which only depend on the scan range of the transition stage and the designe of the wedges where the last one does not change for one measurement to other. For this high-resolution measurement, we acquired 1000 images, scanning the wedges position from

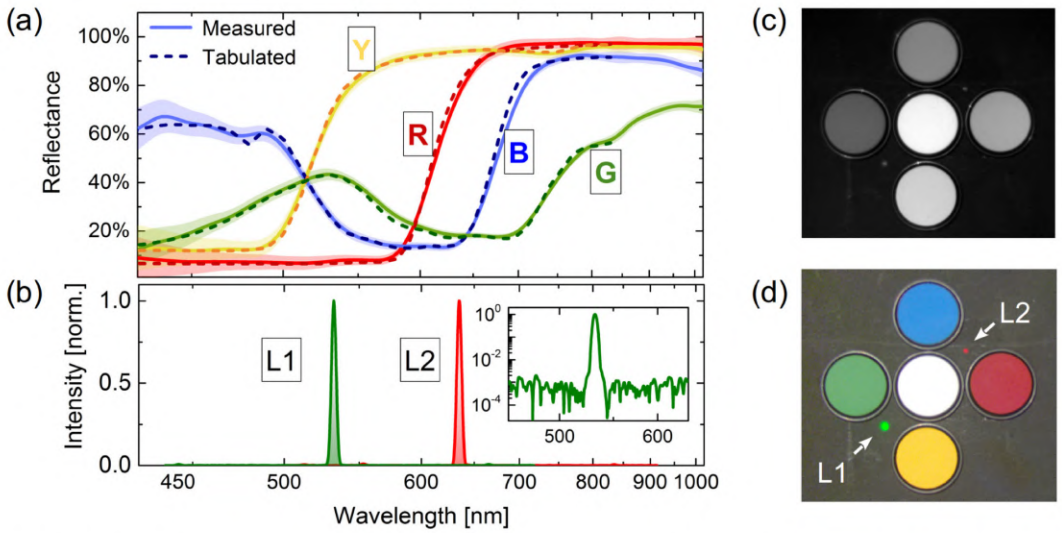


Figure 42 – Optical Characterization of the Hyperspectral Camera: a)Tabulated(dashed lines) and measured (solid lines) reflectance spectra of the color standards; the shaded areas are wavelength-dependent standard deviations of the spectra measured over all points of each color standard surface. b)Measured spectra of the lasers L1 and L2; the inset spectrum shows L1 spectrum in log scale. (c) Intensity single-exposure image of the test object. (d) RGB image generated from the hyperspectral data-cube. This figure was extracted from the reference [82].

for ±5 mm. For this scanning range we obtained a spectral resolution of 3 THz ($\approx$ 4 nm at $\lambda = 635$ nm), which corresponds to 1/150 of the spectral range of the camera. We also measured the fringe visibility of two interferogram coming from a pixel on the region of the Y colored standard and on the L_1 area, and obtained 86.5% and 84% respectively. The high contrast proves that, when placed before the camera lens, the TWINS interferometer provides high degree of coherence at the single-pixel level, as required by FT HSI. The RGB image showed in Fig.42d) was generated using the measured spectrum of each pixel.

5.1.2 Artworks imaging

We tested the potentiality of our hyperspectral camera to image artworks and, more specifically, an Egyptian cartonnage, dated between Ptolemaic and Roman Periods [83], and currently at the Museo Civico di Crema e del Cremasco (Italy). Fig.43a) shows the RGB image generated with the hyperspectral data, after illumination with the 150W Xenon lamp. For this measurements we acquired 400 images (±1 mm scan) with 10 ms of exposure time. To obtain the absolute reflectance in each pixel of the image we placed the white standard Spectralon in the field of view and used the same procedure described in the section 5.1.1. In Fig.43c) we can see the reflectivity spectra of three selected pixels from the image. To identify the Egyptian Blue ($CaCuSi_4O_{10}$) pigment in the cartonnage, we also performed fluorescence measurements in the sample, using for this a broadband LED ($\lambda = 617$ nm) for excitation and with exposure time of 700 ms per image. Fig.43b)

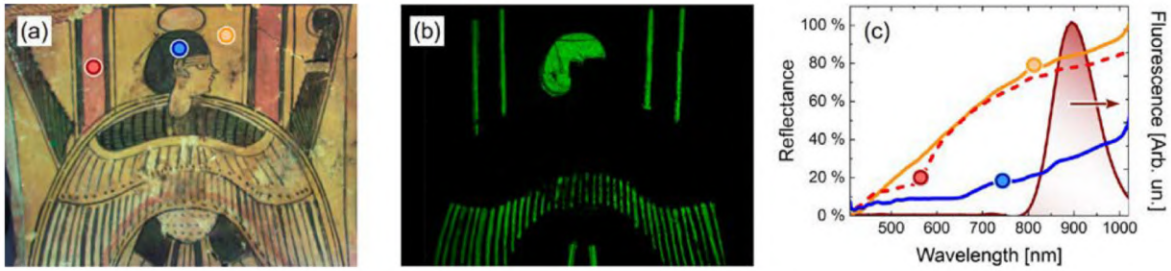


Figure 43 – Hyperspectral imaging of the Egyptian cartonnage (size $\sim$ 18 cm$\times$16 cm): a) RGB image synthesized from the hyperspectral data. b) False-color fluorescence image a $\lambda = 900$ nm after excitation at $\lambda = 617$ nm. c) Solid/dashed lines: reflectance spectra of three points of panel a); shaded area: fluorescence spectrum. This figure was extracted from the reference [84].

shows the resulting fluorescence hyperspectral image of the sample, which reveals a massive presence of Egyptian Blue in some of the decorations. The measured emission spectrum is the shaded area in Fig.43c) and is in excellent agreement with literature. [83]

5.2 Hyperspectral Microscope

5.2.1 Spectral Calibration

Initialy we performed some tests to verify the hyperspectral microscope capability and to obtain the wavelength calibration. For that we imaged a smartphone screen, as shown in Fig.44. We acquired 500 images, scanning the position of the wedges from -0.4 to 1.6 mm around the zero phase delay (ZPD). The exposure time was set to 300 ms for each single frame, giving an acquisition time for the hyperspectral cube of around seven minutes. After the FT of the interferogram for each image pixel, we obtained the spectra from the red (R), green (G), and blue (B) emitters. Panel d) compares the spectra measured by the hyperspectral microscope with the average one detected by a traditional grating-based spectrometer. The very good agreement between the two techniques reveals the hyperspectral capability of the FT microscope. The Fig.44c) shows the RGB color map reconstructed from the spectral hypercube after FT. We used the spectra from these three emitters completed by the spectra peaks from the light of a mercury and a Ne-Ar lamps to calibrate the frequency axes of the spectral imaging system.

For the first fluorescence measurements we prepared a sample with two dyes deposited in a paper to test the capability of the system to separate their spectrum. Fluorescence images were carried out with a 20$\times$ objective. We collected 500 images with 90 ms exposure time each, scanning the position of the wedges from -2.0 to 1.0 mm around the ZPD. Fig.45 shows a hyperspectral microscope image displaying the fluorescence coming from the green beads and the rhodamine 6G deposited in an paper. The RGB color maps showed in the top of the Fig.45 were reconstructed from the spectral

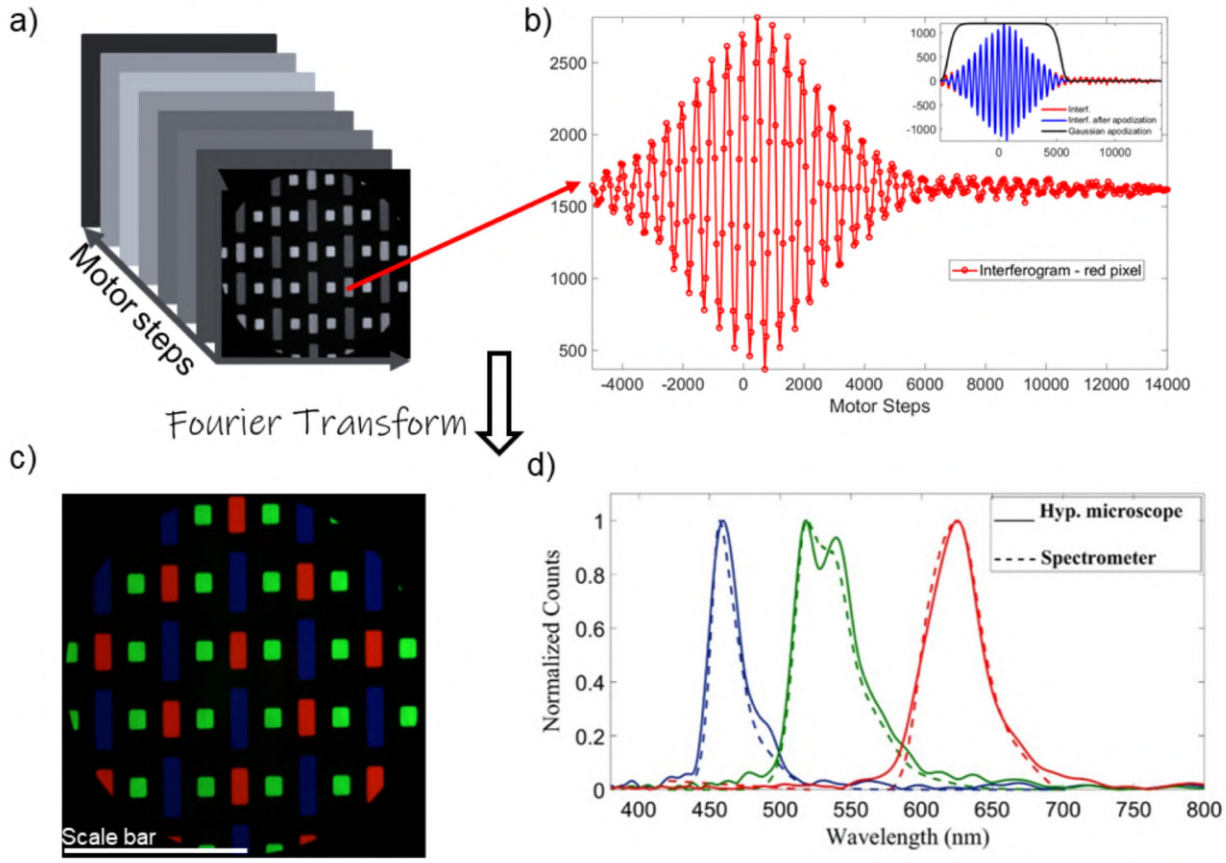


Figure 44 – Hyperspectral microscope image of a smartphone digital display: a)hyperspectra hypercube obtain after aquired the 500 images, scanning the positions of the wedge. b)Interferogram of the red emitter pixel, and the inset graph shows the same interferogram after the gaussian apodization process. c)The colored image (587×587 pixels) is generated from the measured spectra of the R, G, B emitters. The scale bar is 225μm. d)Spectra of the R, G, B emitters, measured by the hyperspectral microscope (solid line) and a commercial dispersive spectrometer (dashed line).

hypercube, selecting diferent spectral regions of interested. At the left we selected from 500 to 750 nm to show the fluorescence contributions of the rhodamine and the green beads, in the center we only selected the green beads fluorescence contribution by spectral filtering between 510 and 520 nm, and in the right we showed the rhodamine contribution for the fluorescence image by filtering from 570 to 590 nm. The graph in the bottom of the figure shows the spectra from two points selected in the sample, where in 1 is a region that has a strong contribution from the green beads and 5 from the other dye. For comparison we measured in a commercial spectrometer the fluorescence spectra, with the same filters used in the hyperspectral microscope, from a sample prepared with the green beads solution deposited in a paper, and another sample prepared with the rhodamine solution deposited in a paper, also showed in the graph. The setup could separate very well the contribution from the different dyes, as can be seen in the graph.

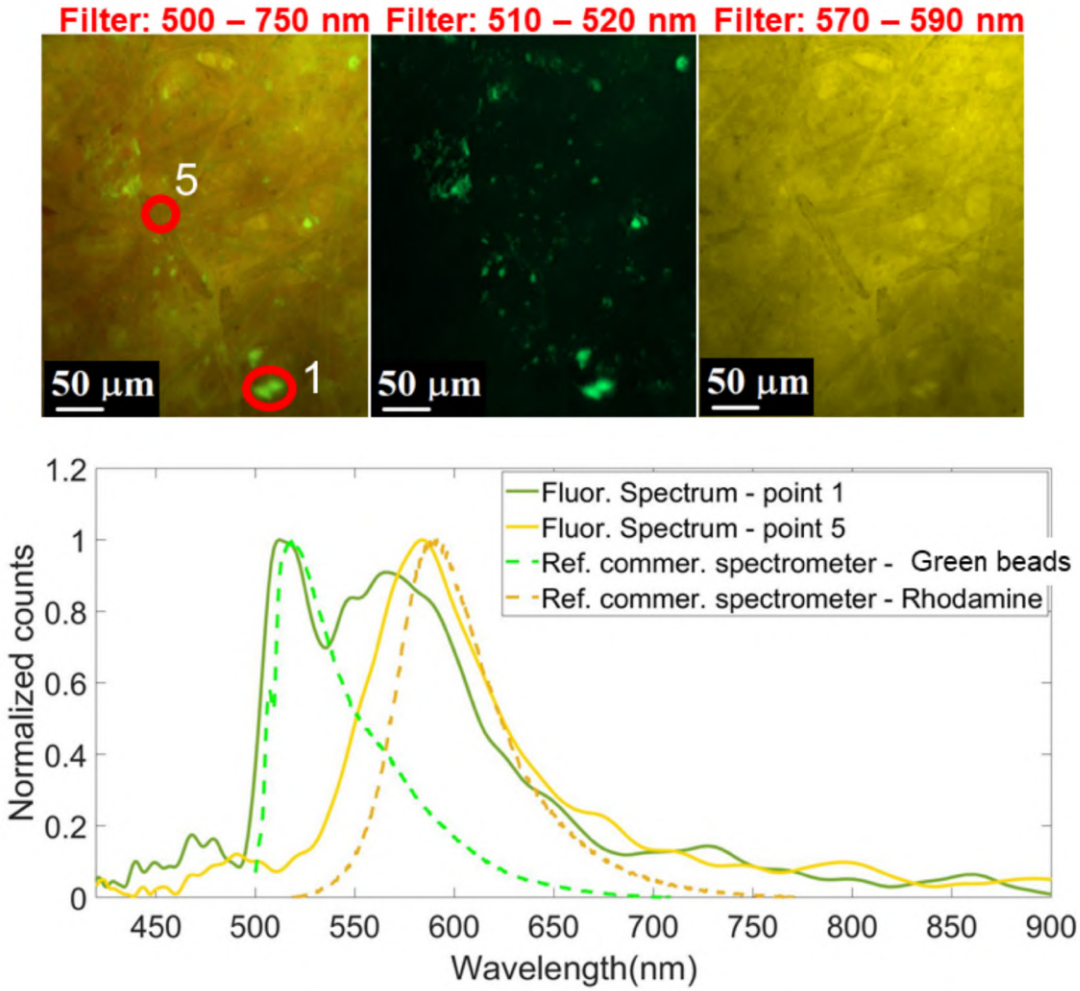


Figure 45 – Hyperspectral fluorescence image of rhodamine 6G mixed with green beads solutions deposited in a paper. At the top we can see false-color images synthesized from the spectral hypercube for the same region of the sample showing different spectral regions of interest. At the bottom we have the spectra from two points, 1 and 5, where the point 1 represents the spectrum from the greeen beads and 5 the spectrum from the rhodamine. The graph includes the fluorescence spectrum from the same dyes measured by a standard grating spectrometer.

5.2.2 Nanomaterials Imaging

In this section we show the application of the hyperspectral microscope to image the photoluminescence emission of single layer nanomaterials. We show results for exfoliated atomically thin sheets of WS_2 (tungsten disulfide) which is a semiconducting transition metal dichalcogenide. The band structure of this material undergoes from an indirect to a direct transition when thinned to a single monolayer which seems to be a similar behavior for different transition metal dichalcogenides. The optical properties of this material have been widely studied, from the bulk configuration to the one, two, and few layers configuration. [85] [86] The idea to measured photoluminescence (PL) spectra of exfoliaded WS_2 layers deposited on SiO_2/Si substrate was to find out if it would be possible to detect differences in the PL spectra due to different stacked layers of the material. These samples were prepared in colaboration with the doctoral student Rafael Nunes Gontijo, supervised by Prof. Cristiano Fantini Leite, who also participated in the discussions of the results.

We performed the measurements using a 100× objective, decreasing the power of the laser to the lowest possible value in a way that the fluorescence signal could still be detected. The power of the excitation was set to 6 mW, which was measured close to the sample focus position. The first picture showed in Fig.46 is a bright field optical image,

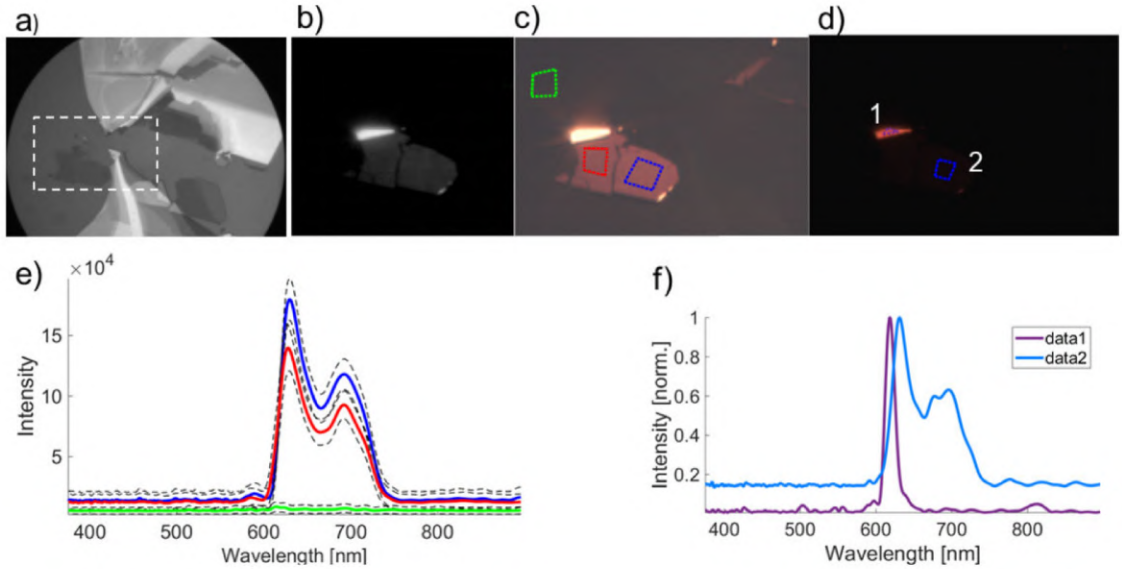


Figure 46 – Hyperspectral microscope fluorescence images of mechanically exfoliated WS_2 flakes: a)bright field optical image in the region of the sample we performed the measurements, b) black and white fluorescence picture obtained in the hyperspectral microscope, c) and d)RGB colormap obtained from the hyperspectral microscope fluorescence images for exposure time of 1600 and 400 ms respectively, e)spectra for the selected regions showed in c) f)spectra for the selected regions showed in d).

that shows a region of the sample with monolayers, bilayers, and few layers of WS_2 and

the second is one fluorescence image (black and white) obtained through the hyperspectral microscope excitating at 488 nm. The other two pictures are hyperspectral microscope fluorescence images (RGB color maps reconstructed from the spectral hypercube) of the same region, that display how the emisson intensity decrease from a monolayer to a bilayer, and to a few layers system. It was extimated that it drops more than 100 folds when the thickness is increased from monolayer to bilayer and gradually dimishes with further increase thickness [86]. To detect the PL from the monolayer and also from the bilayer, we measured with two exposure time: with 1600 ms we acquired 655 images (6 μm step, from -1.97 mm to 1.97 mm) in order to measured the bilayer emission, and with 400 ms we acquired 600 images (6 μm step, from -1.8 mm to 1.8 mm) for the monolayer. In the bottom of the Fig.46 we show the spectra obtained in the selected regions from the both measurements that when compared to the spectra obtained by Weijie Zhaoa and *et al.* (shown in the Fig.47), leads us to conclude that they are really monolayer and bilayer of WS_2.

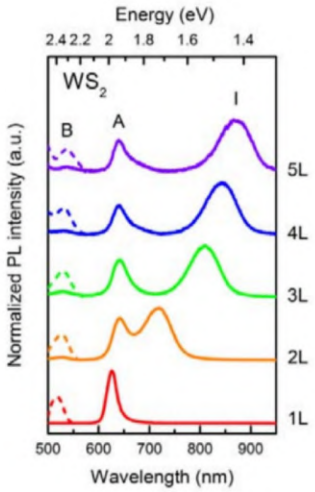


Figure 47 – Normalized photoluminescence spectra of mechanically exfoliated WS_2 flakes consisting of 1 to 5 layers. The figure was extrated from the ref. [86].

5.2.3 Biological Tissue Imaging

In this section we present results for the hyperspectral imaging of biological materials, part of a project that we started in collaboration with the Universidade Federal de Pernambuco. The aim of the project is the analysis of liver tissues infected with *Schistosoma mansoni*. Schistosomiasis is a tropical disease caused by parasitic worms of the genus *Schistosoma*. Mice hepatic tissues infected with *Schistosoma mansoni* is an experimental model that has been widely used to resemble the human disease, which we also used here since it is easily reproducible. [52] We followed the evolution of the disease through three different stages: 30, 60, and 120 days of infection. In Fig.48 we show the autofluorescence hyperspectral imaging of the control sample. We performed

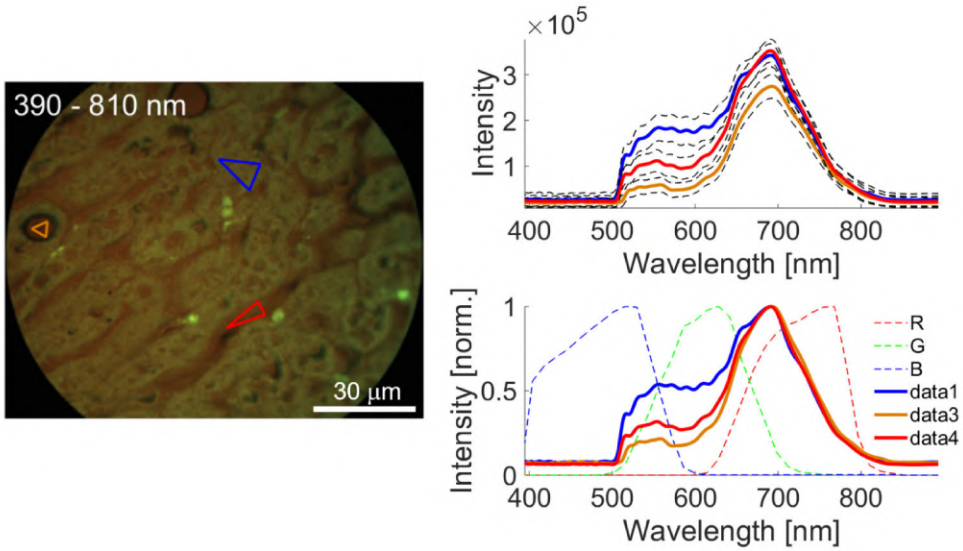
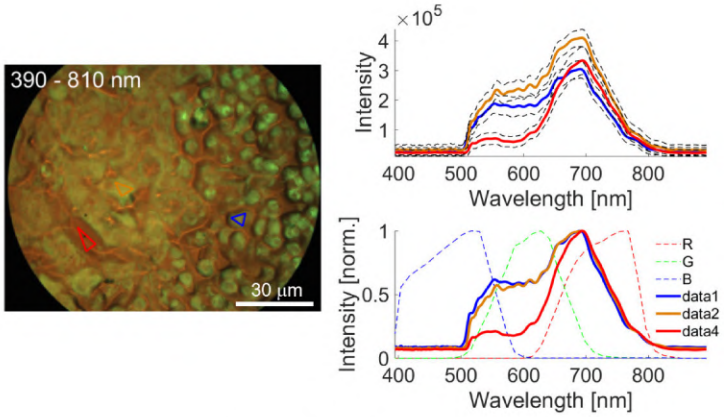


Figure 48 – Autofluorescence hyperspectral imaging of a mouse liver from an uninfected sample with the spectra from selected regions.

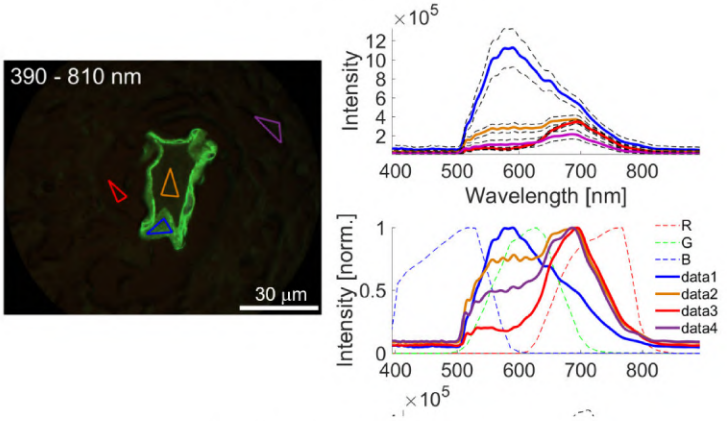
the measurements using a 100× objective, excitating at 488 nm, and collecting the autofluorescence signal above 505 nm. All the four hypercube (shown in Figs.48 and 49) was obtained acquiring 500 images (8 μm step, from -2 mm to 2 mm) with 5000 ms of exposure time. From the hyperspectral autofluorescence false-color image showed in Fig.48, we can indentify the hepatocytes, and from the spectra we can extract two contributions, one around 550 nm and the other at 689 nm. Exciting at 488 nm, the autofluorescence contribution at 550 nm may correspond to the emission of flavins fluorophores, and at 689 nm may correspond to the emission of porphyrins fluorophores. [47]

Fig.49 shows the hyperspectral images of the liver tissues infected with the disease after 60 and 120 days, and the spectra of selected regions. In the sample that has been infected for 60 days, the second hyperspectral imaging showed in Fig.49, we detected a region with the egg of the parasite. It has a very characteristic and intense autofluorescence spectrum, with a peak around 580 nm. In comparison to the control sample, the main difference in all infected samples, seems to be around the peak at 550 nm which we believe is the contribution from the emission of flavins fluorophores. The other autofluorescence contribution, at 689 nm, seems very similiar in all samples. We did not display the autofluorescence spectrum for the sample that had been infected for 30 days because we could not observe any differences when compared to the control sample. However, all samples that were infected show great morphological differences when compared to the control sample, as we can see in Fig.50.

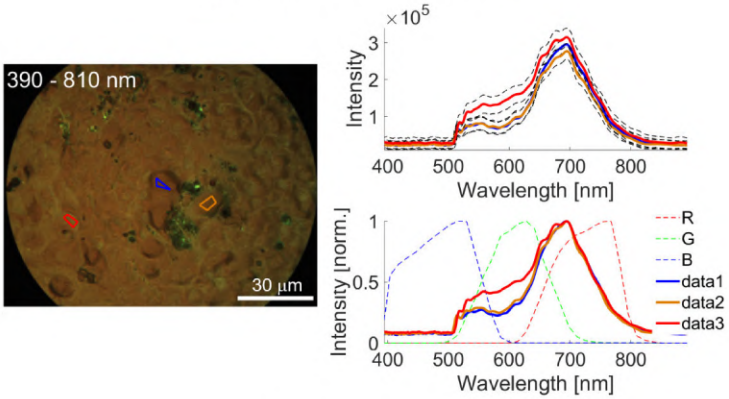
To obtain a quantitative analysis of the liver samples, we will need a larger number of samples. We also tried to image the same samples for excitation wavelength at 405 nm in order to obtain information of the collagen autofluorescence. However, we did not detect any signal from the collagen.



(a) 60 days of infection.



(b) 60 days of infection.



(c) 120 days of infection.

Figure 49 – Representative autofluorescence hyperspectral imaging of the mouse livers infected with *S. mansoni*: typical granulomas at different developmental stages of the disease with the spectra from the selected regions.

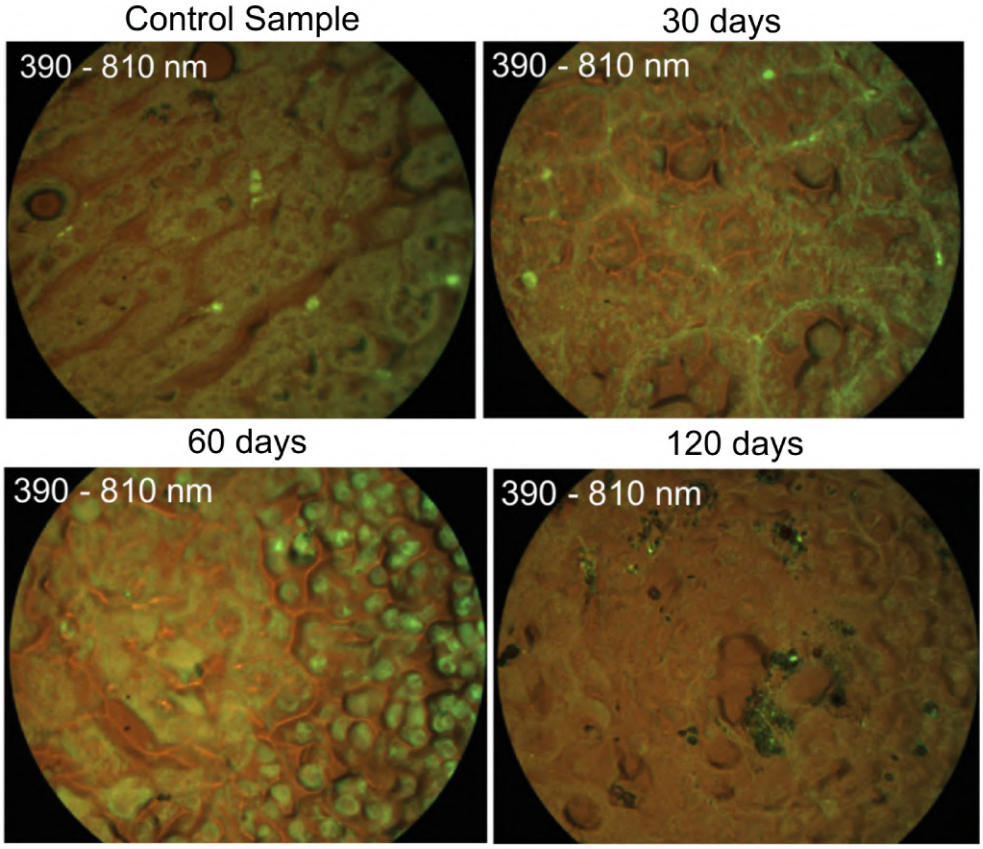


Figure 50 – Representative autofluorescence hyperspectral imaging of the mouse livers showing the evolution of the disease.

6 Conclusion and Perspectives

In this work we developed two projects in parallel where we studied photoinduced processes in aromatic amino acids and developed a hyperspectral camera and microscope setups providing a new way to obtain hyperspectral images.

In the first project, we investigated the UV photoinduced processes in tryptophan, tirosine and phenylalanine solutions by pump-probe spectroscopy, linear absorption, and photoluminescence measurements. In adittion, we also performed *ab initio* calculations to better understand the tryptophan trasient absorption results. We showed for the first time the main excited states of tryptophan in neutral solutions. When pumping at 266 nm, the molecule is excited to the singlet state L_a, after that it evolves through photoinduced deactivation processes which involves singlet and triplet states, and also the possibility of a photoproduct formation. In the transient absorption measurements we only detected positive signals which were fitted very well with the photoinduced absorptions signals from the singlet states L_a and L_b, the triplet state T_1, and also singlet and triplet states of the protonated C4 photoproduct predicted by the calculations. Although, we observed positive signals (which means photoinduced absorption signals in pump-pump maps), we showed that stimulated emission signals from the singlet states were expected and we did not see the negative signals in the map only because they are less intense than the photoinduced absorption signals. For the other two amino acids we do not have the simulations confirming our interpretation of the transient absorption results. The main electronic structure difference from tryptophan to tyrosine and phenylalanine is the energetic distance from the first two singlet states L_a and L_b. In tyrosine and phenylalanine L_a is in higher energy in a way that exciting the molecules solutions at 266 nm we did not access this state. We think that pumping at 266 nm we are exciting the tyrosine and phenylalanine solutions to the singlet state L_b which them follows by a deactivation process that involves photoinduced absorption from these singlet states and problably the photoproduct formation. To confirm this scenario we will also need the *ab initio* calculations.

In the second project we implemented two devices to obtain hyperspectral images for different applications. The novelty of both devices is the way that the hyperspectral images were acquired which are based on a birefringent interferometer. Instead of using filters or dispersive elements, which sometimes require complex and expensive devices, our system consist of the TWINS interferometer. We showed how using the TWINS in our systems add several advantages such as low cost, simplicity, exceptional delay precision and insensitivity to vibrations. We demonstrated the capability of both systems and for the hyperspectral camera we acquired spectral absolute reflectance and fluorescence images

for applications in conservation science and analysis of artworks. For the hyperspectral microscope we acquired fluorescence and autofluorescence images for applications in nanomaterials imaging and in biological tissues studies. For the WS_2 studied we still need to analyze more samples which will give more information about the monolayers, bilayers, and few layers configurations. For the liver tissues infected with *Schistosoma mansoni* we also need more samples to have a better quantitative analysis of the disease evolution.

Bibliography

[1] Soorkia, S.; Jouvet, C.; Grégoire G.: *UV photoinduced dynamics of conformer-resolved aromatic peptides*. Chemical Reviews, 2019. Cited 2 times on pages 15 and 53.

[2] Lakowicz, J. R.: *Protein fluorescence*. Em *Principles of fluorescence spectroscopy*, páginas 341–381. Springer, 1983. Cited on page 15.

[3] Meer, F. D.; Van der Werff, H. M. A.; Van Ruitenbeek F. J. A.; Hecker C. A.; Bakker W. H.; Noomen M. F.; Van Der Meijde M.; Carranza E. J. M.; De Smeth J. B.; Woldai T. Van der: *Multi-and hyperspectral geologic remote sensing: A review*. International Journal of Applied Earth Observation and Geoinformation, 14(1):112–128, 2012. Cited on page 15.

[4] Ossa, M. Á. F.; Amigo, J. M.; García Ruiz C. de la: *Detection of residues from explosive manipulation by near infrared hyperspectral imaging: A promising forensic tool*. Forensic Science International, 242:228–235, 2014. Cited on page 16.

[5] Gowen, A. A.; O'Donnell, C. P.; Cullen P. J.; Downey G.; Frias J. M.: *Hyperspectral imaging–an emerging process analytical tool for food quality and safety control*. Trends in Food Science & Technology, 18(12):590–598, 2007. Cited on page 16.

[6] Cucci, C.; Delaney, J. K.; Picollo M.: *Reflectance hyperspectral imaging for investigation of works of art: old master paintings and illuminated manuscripts*. Accounts of Chemical Research, 49(10):2070–2079, 2016. Cited on page 16.

[7] Gosnell, M. E.; Anwer, A. G.; Cassano J. C.; Sue C. M.; Goldys E. M.: *Functional hyperspectral imaging captures subtle details of cell metabolism in olfactory neurosphere cells, disease-specific models of neurodegenerative disorders*. Biochimica et Biophysica Acta (BBA)-Molecular Cell Research, 1863(1):56–63, 2016. Cited on page 16.

[8] Griffiths, D. J.: *Introduction to Electrodynamics*. Prentice Hall New Jersey, 1962. Cited on page 17.

[9] Born, M.; Wolf, E.: *Principles of Optics: Electromagnetic Theory of Propagation, Interference and Diffraction of Light*. Cambridge University Press, 1956. Cited on page 18.

[10] Diels, J. C.; Rudolph, W.: *Ultrashort Laser Pulse Phenomena*. Elsevier, 2006. Cited on page 18.

[11] Zilio, S. C.: *Óptica Moderna*. São Carlos-SP: Instituto de Física de São Carlos, 93:217–233, 2009. Cited 4 times on pages 19, 21, 24, and 32.

[12] Fowles, G. R.: *Introduction to Modern Optics*. Courier Corporation, 1989. Cited 4 times on pages 19, 21, 23, and 33.

[13] *Refractive Index Database*. `https://refractiveindex.info/?shelf=main&book=BaB2O4&page=Tamosauskas-o`. Accessed: 2020-04-06. Cited on page 21.

[14] Boyd, R. W.: *Nonlinear Optics*. Elsevier, 2003. Cited 4 times on pages 23, 24, 25, and 26.

[15] Tkachenko, N. V.: *Optical Spectroscopy: Methods and Instrumentations*. Elsevier, 2006. Cited 4 times on pages 23, 24, 53, and 95.

[16] Bertoli, F.: *Development of a Two-Dimensional Electronic Spectroscopy Setup in the Ultraviolet*. Tese de Doutoramento, Politecnico di Milano, Italy, 2016. `http://hdl.handle.net/10589/127342`. Cited on page 25.

[17] Alfano, R. R.: *The Supercontinuum Laser Source: The Ultimate White Light*. Springer, 2016. Cited on page 26.

[18] Manzoni, C.; Cerullo, G.: *Design criteria for ultrafast optical parametric amplifiers*. Journal of Optics, 18(10):103501, 2016. Cited on page 27.

[19] Bradler, M.; Baum, P.; Riedle E.: *Femtosecond continuum generation in bulk laser host materials with sub-μJ pump pulses*. Applied Physics B, 97(3):561, 2009. Cited on page 27.

[20] Varillas, R. B.: *Role of wavefront aberrations of amplified femtosecond pulses in nonlinear optics*. Tese de Doutoramento, Universidad de Salamanca, Spain, 2013. Cited on page 27.

[21] Abramowitz, M.; Davidson, M. W.: *Optical Birefringence*. `https://www.olympus-lifescience.com/en/microscope-resource/primer/lightandcolor/birefringence/`. Accessed: 2020-04-01. Cited on page 28.

[22] Goldstein, A.; Krell, A.; Burshtein Z.: *Transparent Ceramics: Materials, Engineering, and Applications*. Wiley, 2020. Cited 2 times on pages 28 and 29.

[23] *Birefringent Crystals*. `http://www.castech.com/productsinfo.aspx?id=85&selectIndex=0`. Accessed: 2020-04-02. Cited on page 29.

[24] Brida, D.; Manzoni, C.; Cerullo G.: *Phase-locked pulses for two-dimensional spectroscopy by a birefringent delay line*. Optics Letters, 37(15):3027–3029, 2012. Cited on page 29.

[25] Réhault, J.; Maiuri, M.; Oriana A.; Cerullo G.: *Two-dimensional electronic spectroscopy with birefringent wedges*. Review of Scientific Instruments, 85(12):123107, 2014. Cited 2 times on pages 29 and 31.

[26] Borrego-Varillas, R.; Oriana, A.; Ganzer L.; Trifonov A.; Buchvarov I.; Manzoni C.; Cerullo G.: *Two-dimensional electronic spectroscopy in the ultraviolet by a birefringent delay line*. Optics Express, 24(25):28491–28499, 2016. Cited on page 29.

[27] Oriana, A.; Réhault, J.; Preda F.; Polli D.; Cerullo G.: *Scanning Fourier transform spectrometer in the visible range based on birefringent wedges*. Journal of the Optical Society of America A, 33(7):1415–1420, 2016. Cited 3 times on pages 29, 31, and 32.

[28] Réhault, J.; Borrego-Varillas, R.; Oriana A.; Manzoni C.; Hauri C. P.; Helbing J.; Cerullo G.: *Fourier transform spectroscopy in the vibrational fingerprint region with a birefringent interferometer*. Optics Express, 25(4):4403–4413, 2017. Cited 2 times on pages 29 and 31.

[29] Preda, F.; Oriana, A.; Réhault J.; Lombardi L.; Ferrari A. C.; Cerullo G.; Polli D.: *Linear and nonlinear spectroscopy by a common-path birefringent interferometer*. IEEE Journal of Selected Topics in Quantum Electronics, 23(3):88–96, 2016. Cited 2 times on pages 31 and 32.

[30] Davis, S. P.; Abrams, M. C.; Brault J. W.: *Fourier transform spectrometry*. Elsevier, 2001. Cited on page 31.

[31] Coudrain, C.; Bernhardt, S.; Caes M.; Domel R.; Ferrec Y.; Gouyon R.; Henry D.; Jacquart M.; Kattnig A.; Perrault P.; et al.: *SIELETERS, an airborne infrared dual-band spectro-imaging system for measurement of scene spectral signatures*. Optics Express, 23(12):16164–16176, 2015. Cited on page 31.

[32] Naylor, D. A.; Gom, B. G.; Schofield I.; Tompkins G.; Davis G. R.: *Mach-Zehnder Fourier transform spectrometer for astronomical spectroscopy at submillimeter wavelengths*. Em *Millimeter and Submillimeter Detectors for Astronomy*, volume 4855, páginas 540–551. International Society for Optics and Photonics, 2003. Cited on page 31.

[33] Pisani, M.; Zucco, M.: *Compact imaging spectrometer combining Fourier transform spectroscopy with a Fabry-Perot interferometer*. Optics Express, 17(10):8319–8331, 2009. Cited on page 31.

[34] Harvey, A. R.; Fletcher-Holmes, D. W.: *Birefringent Fourier-transform imaging spectrometer*. Optics Express, 12(22):5368–5374, 2004. Cited on page 31.

[35] Cerullo, G.; Manzoni, C.; Lüer L.; Polli D.: *Time-resolved methods in biophysics. 4. Broadband pump–probe spectroscopy system with sub-20 fs temporal resolution for the study of energy transfer processes in photosynthesis.* Photochemical & Photobiological Sciences, 6(2):135–144, 2007. Cited 2 times on pages 34 and 35.

[36] Lorenc, M.; Ziolek, M.; Naskrecki R.; Karolczak J.; Kubicki J.; Maciejewski A.: *Artifacts in femtosecond transient absorption spectroscopy.* Applied Physics B, 74(1):19–27, 2002. Cited on page 35.

[37] Borrego-Varillas, R.; Ganzer, L.; Cerullo G.; Manzoni C.: *Ultraviolet transient absorption spectrometer with sub-20-fs time resolution.* Applied Sciences, 8(6):989, 2018. Cited 2 times on pages 37 and 55.

[38] Weingart, O.; Nenov, A.; Altoè P.; Rivalta I.; Segarra Martí J.; Dokukina I.; Garavelli M.: *COBRAMM 2.0 - A software interface for tailoring molecular electronic structure calculations and running nanoscale (QM/MM) simulations.* Journal of Molecular Modeling, 24(9):271, 2018. Cited on page 37.

[39] Gao, L.; Smith, R. T.: *Optical hyperspectral imaging in microscopy and spectroscopy–a review of data acquisition.* Journal of Biophotonics, 8(6):441–456, 2015. Cited on page 38.

[40] Perri, A.; Faria, B. E. N.; Ferreira D. C. T.; Comelli D.; Valentini G.; Preda F.; Polli D.; de Paula A. M.; Cerullo G.; Manzoni C.: *Hyperspectral imaging with a TWINS birefringent interferometer.* Optics Express, 27(11):15956–15967, 2019. Cited 3 times on pages 39, 40, and 43.

[41] Candeo, A.; Faria, B. E. N.; Erreni M.; Valentini G.; Bassi A.; de Paula A. M.; Cerullo G.; Manzoni C.: *A hyperspectral microscope based on an ultrastable common-path interferometer.* APL Photonics, 4(12):120802, 2019. Cited 3 times on pages 39, 44, and 45.

[42] Peatross, J.; Ware, M.: *Physics of light and optics.* Brigham Young University, Department of Physics, 2011. Cited on page 41.

[43] Hecht, E.: *Optics.* Pearson Education India, 2012. Cited on page 44.

[44] Nelson, D. L.; Cox, M. M.: *Princípios de Bioquímica de Lehninger.* Artmed Editora, 2018. Cited 2 times on pages 46 and 47.

[45] Vollhardt, P.; Schore, N. E.: *Química Orgânica-: Estrutura e Função.* Bookman Editora, 2013. Cited on page 46.

[46] Croce, A. C.; Bottiroli, G.: *Autofluorescence spectroscopy and imaging: a tool for biomedical research and diagnosis.* European Journal of Histochemistry, 58(4), 2014. Cited on page 48.

[47] Croce, A. C.; Ferrigno, A.; Vairetti M.; Bertone R.; Freitas I.; Bottiroli G.: *Autofluorescence properties of isolated rat hepatocytes under different metabolic conditions.* Photochemical & Photobiological Sciences, 3(10):920–926, 2004. Cited 2 times on pages 48 and 77.

[48] NASCIMENTO, G. A. F.: *Identificação quimiluminescente do perfil de carboidratos e antígenos teciduais em modelo experimental de esquistossomose mansônica.* Tese de Doutoramento, Program in Biological Sciences of the Universidade Federal de Pernambuco, Brazil, 2018. `https://repositorio.ufpe.br/handle/123456789/31073`. Cited on page 48.

[49] Nascimento, G. A. F.; de Lima, L. R. A.; Pereira A. S. A.; Cavalcanti C. L. B.; de Melo Junior M. R.; Chaves M. E. C.; de Carvalho Junior L. B.: *Chemiluminescent detection of glycocode alterations in hepatic granulomatous lesions of experimental schistosomiasis.* International Journal of Clinical and Experimental Pathology, 10(8):8599, 2017. Cited on page 49.

[50] Amaral, K. B.; Silva, T. P.; Malta K. K.; Carmo L. A. S.; Dias F. F.; Almeida M. R.; Andrade G. F. S.; Martins J. S.; Pinho R. R.; Costa Neto S. F.; *et al.*: *Natural Schistosoma mansoni infection in the wild reservoir Nectomys squamipes leads to excessive lipid droplet accumulation in hepatocytes in the absence of liver functional impairment.* PloS One, 11(11), 2016. Cited on page 49.

[51] Lenzi, H. L.; Kimmel, E.; Schechtman H.; Pelajo Machado M.; Vale B. S.; Panasco M. S.; Lenzi J. A.: *Collagen arrangement in hepatic granuloma in mice infected with Schistosoma mansoni: dependence on fiber radiation centers.* Brazilian Journal of Medical and Biological Research, 32(5):639–643, 1999. Cited on page 49.

[52] Junqueira, L. C. U.; Montes, G. S.; Toledo O. M. S.; Joazeiro P. P.: *Morphological, histochemical and biochemical observations on the connective tissue matrix of in situ and isolated hepatic granulomas in experimental murine schistosomiasis.* Annals of Tropical Medicine & Parasitology, 80(1):27–41, 1986. Cited 2 times on pages 49 and 76.

[53] Farani, P. S. G.: *Laboratório de Estudo de Estrutura e Função de Proteínas.* `http://www.ufjf.br/labproteinas/material-de-apoio/esquistossomose/ovo-e-a-formacao-do-granuloma-de-s-mansoni/`. Accessed: 2020-04-09. Cited on page 49.

[54] Guzow, K.; Ganzynkowicz, R.; Rzeska A.; Mrozek J.; Szabelski M.; Karolczak J.; Liwo A.; Wiczk W.: *Photophysical properties of tyrosine and its simple derivatives studied by time-resolved fluorescence spectroscopy, global analysis, and theoretical calculations.* The Journal of Physical Chemistry B, 108(12):3879–3889, 2004. Cited 2 times on pages 51 and 52.

[55] Ross, J. B. A.; Laws, W. R.; Rousslang K. W.; Wyssbrod H. R.: *Tyrosine fluorescence and phosphorescence from proteins and polypeptides.* Em *Topics in Fluorescence Spectroscopy*, páginas 1–64. Springer, 2002. Cited 2 times on pages 51 and 63.

[56] Sobolewski, A. L.; Shemesh, D.; Domcke W.: *Computational studies of the photophysics of neutral and zwitterionic amino acids in an aqueous environment: tyrosine-$(H_2O)_2$ and tryptophan$(H_2O)_2$ clusters.* The Journal of Physical Chemistry A, 113(3):542–550, 2009. Cited on page 52.

[57] Grégoire, G.; Jouvet, C.; Dedonder C.; Sobolewski A. L.: *Ab initio study of the excited-state deactivation pathways of protonated tryptophan and tyrosine.* Journal of the American Chemical Society, 129(19):6223–6231, 2007. Cited 2 times on pages 52 and 53.

[58] Nolting, D.; Marian, C.; Weinkauf R.: *Protonation effect on the electronic spectrum of tryptophan in the gas phase.* Physical Chemistry Chemical Physics, 6(10):2633–2640, 2004. Cited 2 times on pages 52 and 53.

[59] Sharma, D.; Léonard, J.; Haacke S.: *Ultrafast excited-state dynamics of tryptophan in water observed by transient absorption spectroscopy.* Chemical Physics Letters, 489(1-3):99–102, 2010. Cited on page 53.

[60] Léonard, J.; Sharma, D.; Szafarowicz B.; Torgasin K.; Haacke S.: *Formation dynamics and nature of tryptophan's primary photoproduct in aqueous solution.* Physical Chemistry Chemical Physics, 12(48):15744–15750, 2010. Cited on page 53.

[61] Lessing, H. E.; Von Jena, A.: *Separation of rotational diffusion and level kinetics in transient absorption spectroscopy.* Chemical Physics Letters, 42(2):213–217, 1976. Cited on page 53.

[62] Schott, S.; Steinbacher, A.; Buback J.; Nuernberger P.; Brixner T.: *Generalized magic angle for time-resolved spectroscopy with laser pulses of arbitrary ellipticity.* Journal of Physics B: Atomic, Molecular and Optical Physics, 47(12):124014, 2014. Cited on page 53.

[63] Lin, S. W.; Sakmar, T. P.: *Specific tryptophan UV-absorbance changes are probes of the transition of rhodopsin to its active state.* Biochemistry, 35(34):11149–11159, 1996. Cited on page 54.

[64] Bram, O.; Oskouei, A. A.; Tortschanoff A.; van Mourik F.; Madrid M.; Echave J.; Cannizzo A.; Chergui M.: *Relaxation dynamics of tryptophan in water: a UV fluorescence up-conversion and molecular dynamics study.* The Journal of Physical Chemistry A, 114(34):9034–9042, 2010. Cited on page 56.

[65] Liu, H.; Zhang, H.; Jin B.: *Fluorescence of tryptophan in aqueous solution.* Spectrochimica Acta Part A: Molecular and Biomolecular Spectroscopy, 106:54–59, 2013. Cited on page 56.

[66] Saito, I.; Sugiyama, H.; Yamamoto A.; Muramatsu S.; Matsuura T.: *Photochemical hydrogen-deuterium exchange reaction of tryptophan. The role in nonradioative decay of singlet tryptophan.* Journal of the American Chemical Society, 106:4286–4287, 1984. Cited on page 57.

[67] Jou, F. Y.; Freeman, G. R.: *Temperature and isotope effects on the shape of the optical absorption spectrum of solvated electrons in water.* Journal of Physical Chemistry, 83(18):2383–2387, 1979. Cited on page 58.

[68] Schwartz, B. J.; Rossky, P. J.: *Aqueous solvation dynamics with a quantum mechanical solute: computer simulation studies of the photoexcited hydrated electron.* The Journal of Chemical Physics, 101(8):6902–6916, 1994. Cited on page 58.

[69] Tomasello, G.; Wohlgemuth, M.; Petersen J.; Mitrić R.: *Photodynamics of Free and Solvated Tyrosine.* The Journal of Physical Chemistry B, 116(30):8762–8770, 2012. Cited 2 times on pages 62 and 64.

[70] Pagba, C. V.; Chi, S. H.; Perry J.; Barry B. A.: *Proton-coupled electron transfer in tyrosine and a β-hairpin maquette: Reaction dynamics on the picosecond time scale.* The Journal of Physical Chemistry B, 119(6):2726–2736, 2015. Cited 2 times on pages 62 and 64.

[71] Pagba, C. V.; McCaslin, T. G.; Chi S. H.; Perry J. W.; Barry B. A.: *Proton-Coupled Electron Transfer and a Tyrosine–Histidine Pair in a Photosystem II-Inspired β-Hairpin Maquette: Kinetics on the Picosecond Time Scale.* The Journal of Physical Chemistry B, 120(7):1259–1272, 2016. Cited 2 times on pages 62 and 64.

[72] Oliver, T. A. A.; Zhang, Y.; Roy A.; Ashfold M. N. R.; Bradforth S. E.: *Exploring autoionization and photoinduced proton-coupled electron transfer pathways of phenol in aqueous solution.* The Journal of Physical Chemistry Letters, 6(20):4159–4164, 2015. Cited on page 62.

[73] Chen, X.; Larsen, D. S.; Bradforth S. E.; van Stokkum I. H. M.: *Broadband spectral probing revealing ultrafast photochemical branching after ultraviolet excitation of the*

aqueous phenolate anion. The Journal of Physical Chemistry A, 115(16):3807–3819, 2011. Cited 2 times on pages 62 and 64.

[74] Konev, S. V.: *Fluorescence and phosphorescence of proteins and nucleic acids*. Springer Science & Business Media, 2012. Cited 2 times on pages 64 and 67.

[75] Omidyan, R.; Ataelahi, M.; Azimi G.: *Excited-state deactivation mechanisms of protonated and neutral phenylalanine: a theoretical study*. RSC Advances, 5(37):29032–29039, 2015. Cited on page 66.

[76] Belshaw, L.; Calegari, F.; Duffy M. J.; Trabattoni A.; Poletto L.; Nisoli M.; Greenwood J. B.: *Observation of ultrafast charge migration in an amino acid*. The Journal of Physical Chemistry Letters, 3(24):3751–3754, 2012. Cited on page 66.

[77] Féraud, G.; Broquier, M.; Dedonder C.; Jouvet C.; Grégoire G.; Soorkia S.: *Excited state dynamics of protonated phenylalanine and tyrosine: Photo-induced reactions following electronic excitation*. The Journal of Physical Chemistry A, 119(23):5914–5924, 2015. Cited on page 66.

[78] McGuinness, C. D.; Macmillan, A. M.; Sagoo K.; McLoskey D.; Birch D. J. S.: *Excitation of fluorescence decay using a 265 nm pulsed light-emitting diode: evidence for aqueous phenylalanine rotamers*. Applied Physics Letters, 89(6):063901, 2006. Cited on page 66.

[79] Rzeska, A.; Stachowiak, K.; Malicka J.; Łankiewicz L.; Wiczk W.: *Photophysics of phenylalanine analogues: Part 1. Constrained analogues of phenylalanine modified at phenyl ring*. Journal of Photochemistry and Photobiology A: Chemistry, 133(1-2):33–38, 2000. Cited on page 66.

[80] Shiokawa, N.; Xue, B.; Nakata K.; Tokunaga E.; Kobayashi T.: *DUV ultrafast electronic relaxation and real-time vibration dynamics in l-phenylalanine*. Em *International Conference on Ultrafast Phenomena*, páginas UTu4A–8. Optical Society of America, 2016. Cited on page 66.

[81] Lee, Y.; Jung, J.; Kim B.; Butz P.; Snoek L. C.; Kroemer R. T.; Simons J. P.: *Alanyl side chain folding in phenylalanine: conformational assignments through ultraviolet rotational band contour analysis*. The Journal of Physical Chemistry A, 108(1):69–73, 2004. Cited on page 67.

[82] Perri, A.; de Faria, B. E. N.; Ferreira D. C. T.; Comelli D.; Valentini G.; Polli D.; Cerullo G. N.; Manzoni C.: *A hyperspectral camera for conservation science, based on a birefringent ultrastable common path interferometer*. Em *Optics for Arts, Architecture, and Archaeology VII*, volume 11058, página 110580B. International Society for Optics and Photonics, 2019. Cited on page 71.

[83] Comelli, D.; Capogrosso, V.; Orsenigo C.; Nevin A.: *Dual wavelength excitation for the time-resolved photoluminescence imaging of painted ancient Egyptian objects*. Heritage Science, 4(1):21, 2016. Cited 2 times on pages 71 and 72.

[84] Perri, A.; de Faria, B. E. N.; Ferreira D. C. T.; Polli D.; Comelli D.; Valentini G.; Cerullo G.; Manzoni C.: *A Hyperspectral Camera for Remote Sensing based on a Birefringent Ultrastable Common-Path Interferometer*. Em *Hyperspectral Imaging and Sounding of the Environment*, páginas HM3C–4. Optical Society of America, 2018. Cited on page 72.

[85] Tongay, S.; Zhou, J.; Ataca C.; Lo K.; Matthews T. S.; Li J.; Grossman J. C.; Wu J.: *Thermally driven crossover from indirect toward direct bandgap in 2D semiconductors: $MoSe_2$ versus MoS_2*. Nano Letters, 12(11):5576–5580, 2012. Cited on page 75.

[86] Zhao, W.; Ghorannevis, Z.; Chu L.; Toh M.; Kloc C.; Tan P. H.; Eda G.: *Evolution of electronic structure in atomically thin sheets of WS_2 and WSe_2*. ACS Nano, 7(1):791–797, 2013. Cited 2 times on pages 75 and 76.

Appendix

APPENDIX A – Aromatic Amino Acids

Here we present the optical characterizations that were performed in the aromatic amino acids at pH 5.35. We separate them from the others because they were very similar to pH 7.4.

A.1 Stead-State Absorption

We measured steady-state absorption spectrum of tryptophan, tyrosine, and phenylalanine in the same conditions as described in the Chapter4.1. In Fig.51 we can see the measurements for the solutions prepared in a buffer solution at pH 5.35.

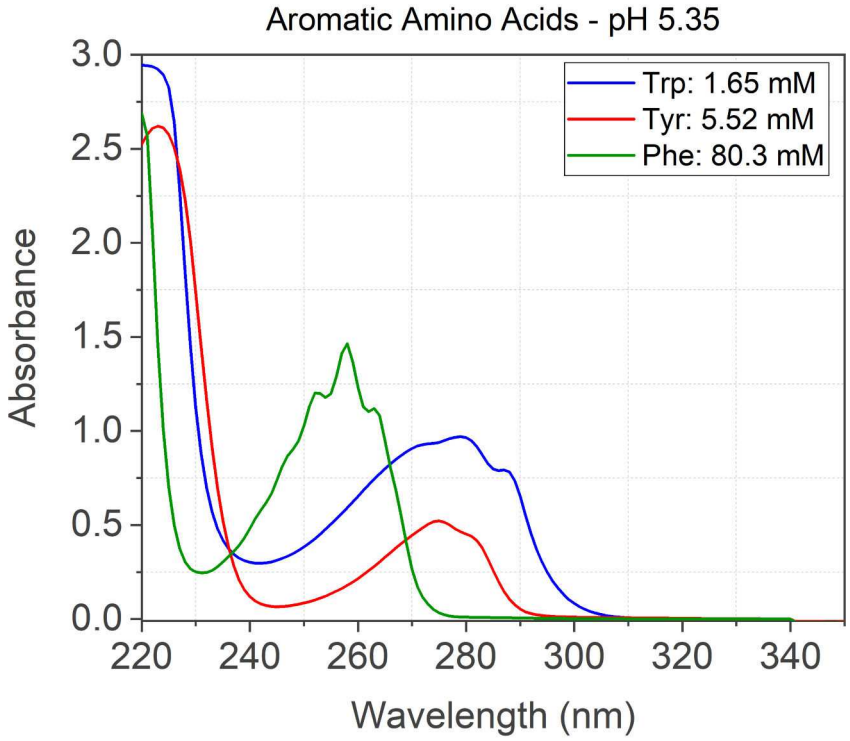
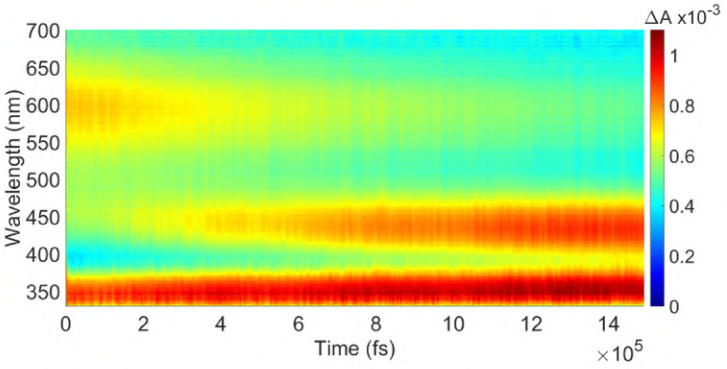


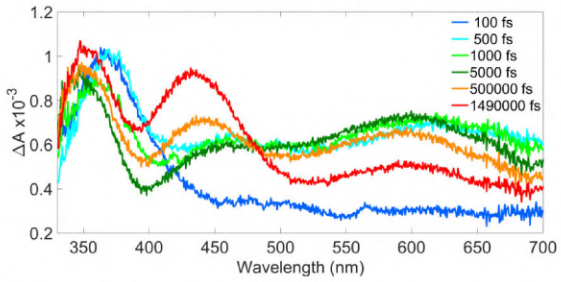
Figure 51 – Linear absorption spectra of tryptophan, tyrosine, and phenylalanine dissolved in a buffer solution at pH 5.35.

A.2 Transient Absorption Measurements

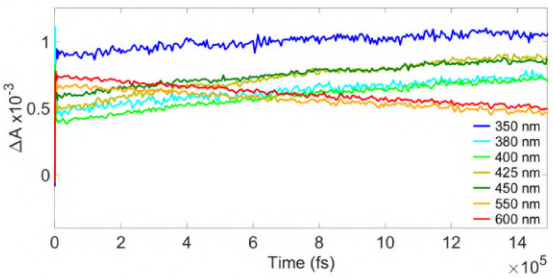
We measured transient absorption of the aromatic amino acids at pH 5.35 in the same conditions as described in section 4.3.2. In Figs. 52, 53, and 54 we present the data for tryptophan, tyrosine, and phenylalanine, respectively:



(a) 2D pump-probe map of transient absorption.

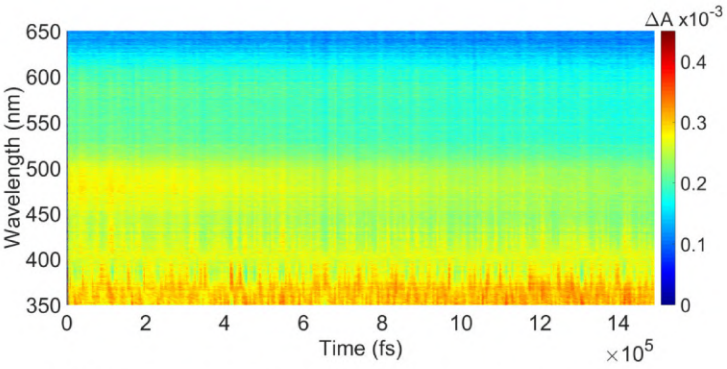


(b) $\Delta T/T$ spectra extracted from the 2D map at selected pump-probe delays.

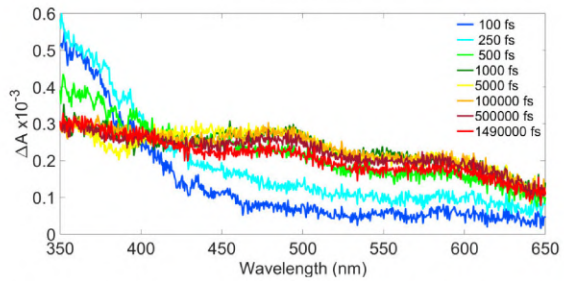


(c) $\Delta T/T$ dynamics extracted from the 2D map at selected probe wavelength.

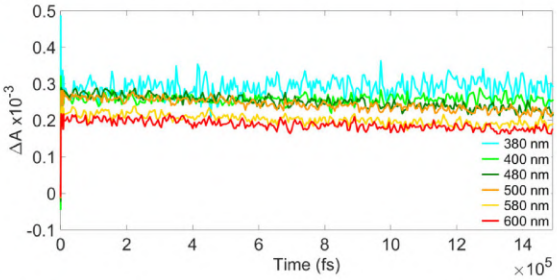
Figure 52 – Transient absorption of Trp in a buffer solution, pH 5.35, after excitation at 266 nm.



(a) 2D pump-probe map of transient absorption.

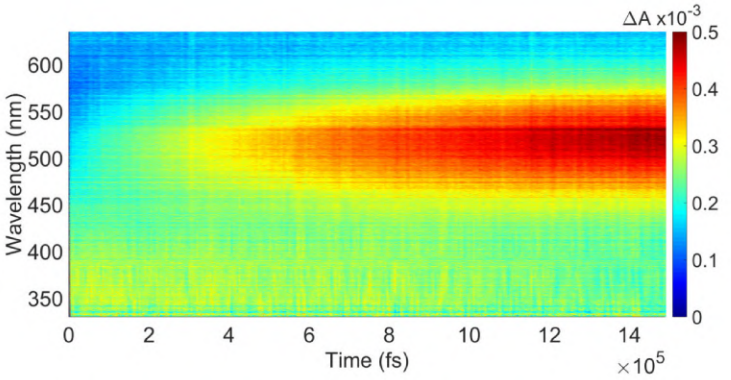


(b) $\Delta T/T$ spectra extracted from the 2D map at selected pump-probe delays.

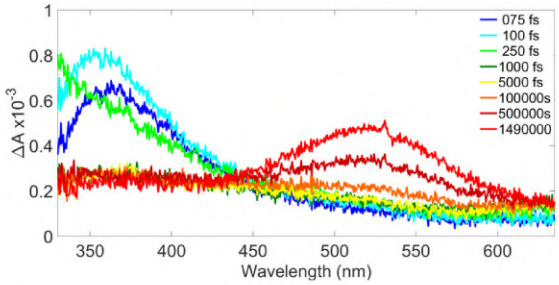


(c) $\Delta T/T$ dynamics extracted from the 2D map at selected probe wavelength.

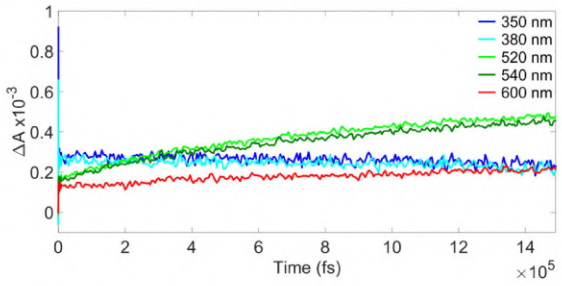
Figure 53 – Transient absorption of Tyr in a buffer solution, pH 5.35, after excitation at 266 nm.



(a) 2D pump-probe map of transient absorption.



(b) $\Delta T/T$ spectra extracted from the 2D map at selected pump-probe delays.



(c) $\Delta T/T$ dynamics extracted from the 2D map at selected probe wavelength.

Figure 54 – Transient absorption of Phe in a buffer solution, pH 5.35, after excitation at 266 nm.

In sumary, the transient absorption measurements at pH 5.35 are quite similar to the ones at pH 7.4. In fact, after studying the literatura and the amino acids physical-chemical properties, we found out that from pH 4 until pH 8 we should expect the same behaviour for each amino acid in solution. In addition, below pH 4 and above pH 8, all of them can present different species in solution. The tyrosine measurements in the the pH 5.35 buffer solution are too noisy, thus it is very difficult to compare with the ones in phosphate buffer saline. However, for tryptophan and phenylalanine we can conclude that the transient absorption pump-probe maps por solutions at pH 7.4 and pH 5.35 are very similar.

A.2.1 Transient Absorption Measurements with Parallel and Perpendicular Polarization

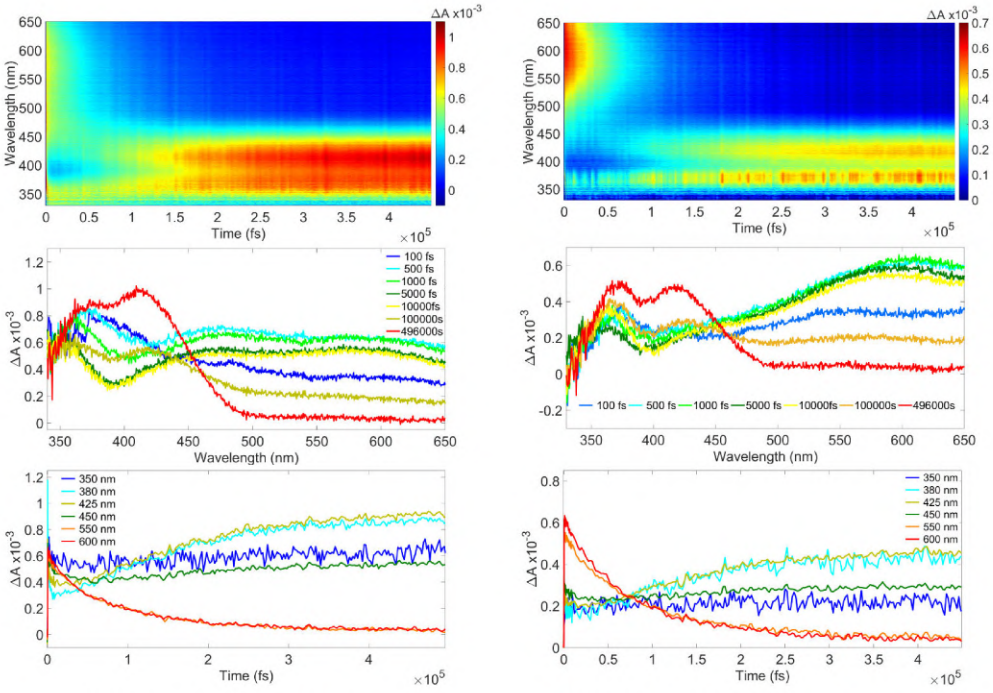
Emission and absorption are transitions between the same electronic states, and both are sensitive to the polarization of the excitation light. In addition, the polarization of the photon emitted by a molecule is determined by the molecule orientation with the most probable photon polarization being at the direction of the transition dipole moment of the molecule. Hence, molecules can absorb photons that have the same orientation polarization of their transition dipole moments but will not interact with photons that have perpendicular polarization with respect to their dipole moment orientation. [15] This means that changing the polarization of the excitation light in pump-probe measurements can exhibit distinct excitation scenarios from the same system.

In order to obtain a complete eletronic structure information on the aromatic amino acids we measured the transient absorption of tryptophan, tyrosine, and phenylalanine in hydrochloric acid aqueous solution, at pH 1.0, changing the pump polarization. We excited the samples with the third-harmonic setup and probe using the WLC generation in the VIS range, with pump and probe polarization set parallel and then perpendicular. These mesurements were performed in lower fluency (0.309 mJ/cm^2) compared to ones at the magic angle polarization and without flowing the samples.

In Fig.55 we show the transient absorption pump-probe maps for tryptophan in both polarization. During the first 5 ps the main differences between the two polarizations are in $400-500$ nm and in $550-650$ nm range, but in the UV spectral range we observed similar behaviour. In the last dynamics we observed that the PA at 370 nm is more intense compared to the PA at 425 nm in the perpendicular polarization.

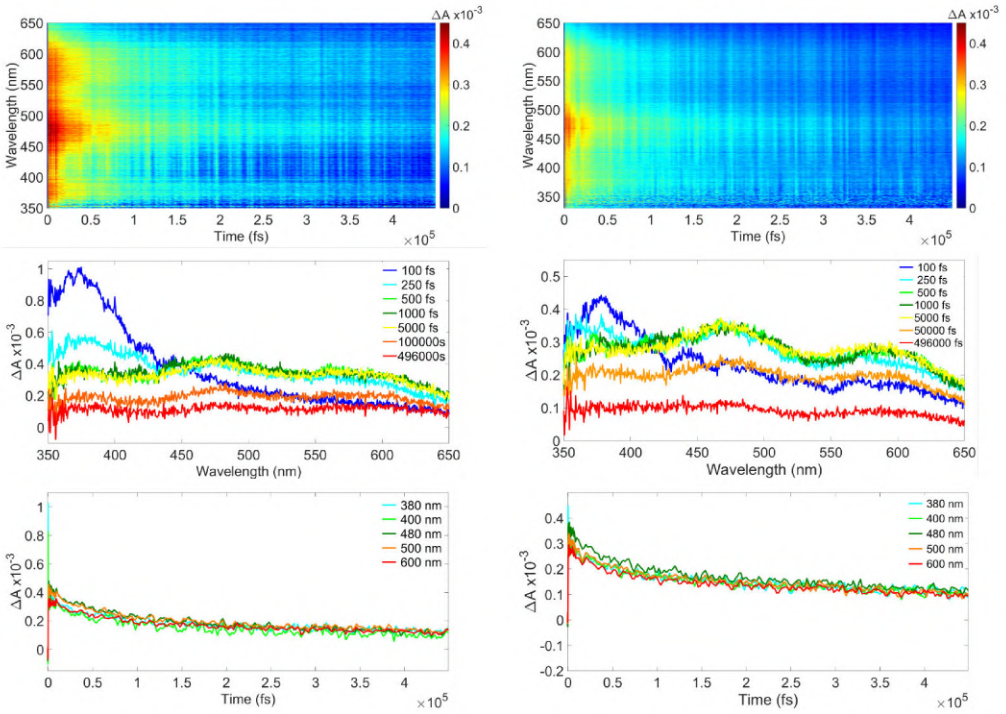
A comparison between the perpendicular and parallel polarizations is a complicate measurement procedure, and when we do it without the complete analysis, without measuring A_{vv}, A_{vh}, A_{hv}, and A_{hh}, where the first index denotes polarization of the excitation and the second shows polarization of the emission, this can leads us to a misinterpretation of the data. Because, if the changes in the polarization measurements, e. g. is due to rotational diffusion, the intensities of the signals will change too, and will not be related the polazation differences of the excited states. Due to lack of time, we were not able to repeat these measurements with all the necessary polarization variations for a complete analysis. In this way, with only these measurements we cannot separate what differences are related to the contribution of the rotation of the molecule and what can be related to the polarization of the excited states.

The results for tyrosine are shown in Fig.56. Here, we could only detect differences in the intensity of the signals which could just mean that the detector has different sensitivity for different polarizations.



(a) Parallel polarization. (b) Perpendicular polarization.

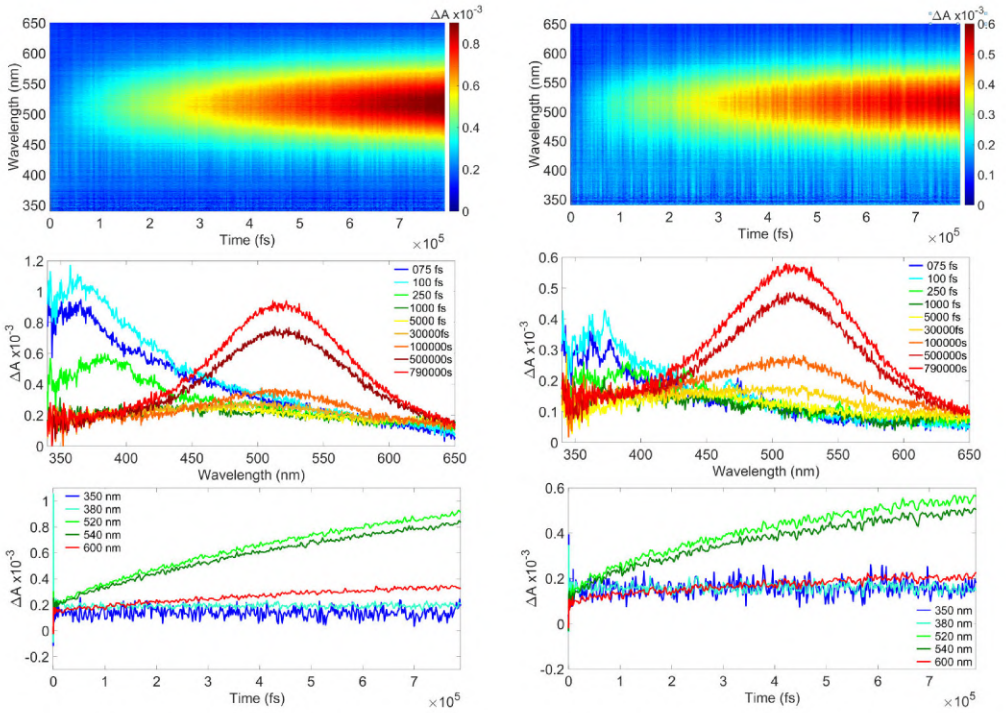
Figure 55 – Comparison between parallel and perpendicular polarization in pump-probe measurements of tryptophan aqueous solution at pH 1.0, after excitation at 266 nm and probe in VIS range.



(a) Parallel polarization. (b) Perpendicular polarization.

Figure 56 – Comparison between parallel and perpendicular polarization in pump-probe measurements of tyrosine aqueous solution at pH 1.0, after excitation at 266 nm and probe in VIS range.

We did the same experiment with phenylalanine and the results can be seen in Fig.57 The situation for phenylalanine is the same as for tyrosine, we only observed



(a) Parallel polarization. (b) Perpendicular polarization.

Figure 57 – Comparison between parallel and perpendicular polarization in pump-probe measurements of phenylalanine aqueous solution at pH 1.0, after excitation at 266 nm and probe in VIS range.

differences in the signal strength.

With only these preliminary results, we believe that the tryptophan polarization measurements should be repeated for a complete analysis. For the other amino acids, the polarization measurements do not seem relevant.

Annex

ANNEX A – Thesis-related Publications

- *Hyperspectral imaging with a TWINS birefringent interferometer*,
  Perri*, A.; de Faria*, B. E. N.; Ferreira, D. C. T.; Comelli, D.; Valentini, G.; Preda, F.; Polli, D.; de Paula, A. M.; Cerullo, G.; Manzoni, C.
  Optics Express, **27**(11), 15956 (2019), https://doi.org/10.1364/OE.27.015956
  * The authors contributed equally to the work

- *A hyperspectral microscope based on an ultrastable common-path interferometer*,
  Candeo, A.; de Faria, B. E. N.; Erreni, M.; Valentini, G.; Bassi, A.; de Paula, A. M.; Cerullo, G.; Manzoni, C.
  APL Photonics **4**, 120802 (2019), https://doi.org/10.1063/1.5129860

- *Hyperspectral Microscope Based on a Birefringent Interferometer for Biomedical Imaging.*
  de Faria, B. E. N., Fonseca, G. R.; Valentini, G.; Bassi, A.; Cerullo, G. N.; Manzoni, C.; de Paula, A. M.
  In: OSA Biophotonics Congress: Optics in the Life Sciences, 2019, Tucson. Biophotonics Congress: Optics in the Life Sciences Technical Digest. Washington, D.C.: OSA Publishing, NS1B.5. (2019).

- *A hyperspectral camera for conservation science, based on a birefringent ultrastable common path interferometer*,
  Perri, A.; de Faria, B. E. N.; Ferreira, D. C. T.; Comelli, D.; Valentini, G.; Polli, D.; Cerullo, G. N.; Manzoni, C.
  Proc. SPIE 11058, Optics for Arts, Architecture, and Archaeology VII, 110580B (2019), https://doi.org/10.1117/12.2525580

- *A Hyperspectral Camera for Remote Sensing based on a Birefringent Ultrastable Common-Path Interferometer.*
  Perri, A.; de Faria, B. E. N., Ferreira, D. C. T.; Comelli, D.; Valentini, G.; Polli, D.; Cerullo, G. N.; Manzoni, C.
  In: Hyperspectral Imaging and Sounding of the Environment 2018, Singapore (2018), https://doi.org/10.1364/HISE.2018.HM3C.4